

ABSTRACT

WALL, JOHN. Analysis and Characterization of Closed Topographic Depressions. (Under the direction of Dr. DelWayne R. Bohnenstiehl).

A closed topographic depression is a landform having no lateral surface flow or external drainage. Such features result from a variety of natural processes including the compaction and pipping of sediments, dissolution of rock, fluvial incision, land sliding, volcanic explosions, and movement of ice. These topographic features may also be formed by human activities within a landscape. Closed depressions are therefore ubiquitous features and, in some areas, they are the primary source of topographic relief.

A semi-automated workflow and toolbox called *HydroCutter* is outlined to hydrologically condition digital elevation models (DEMs) containing manmade dams and culverts. The approach finds intersections between transportation routes and streams, and then lowers the elevation surface across routes to stream level allowing modeled flow to pass. The result of running *HydroCutter* is a reconditioned elevation dataset, which retains naturally formed closed topographic depressions, as well as a catalog of suspected culverts. Problematic areas include extensive road ditches, particularly along divided highways, and where surface flow crosses beneath road intersections. Limitations do exist for this method and results partially depend on the quality of data being input.

The efficacy of inventorying closed topographic depressions within karst topography using an automated fill-difference method on a lidar-derived DEM is evaluated against existing inventories at Mammoth Cave National Park (MACA) and Apalachicola National Forest (ANF). The automated method can identify 95% and 87% of manually identified karst depressions at MACA and ANF, respectively. Additionally, the method increases catalog size by 183% ($n = 797$) at MACA and 505% ($n = 3377$) at ANF, providing a more complete representation of these

landscapes. For features larger than $\sim 10^3$ m² in area and 3-5 m in depth, the resulting distribution of depression sizes is statistically similar to those within the manual catalogs. The disaggregation or aggregation of karst features, relative to these existing inventories, is dependent on the local relief and the density of lidar returns used to generate the DEM.

Where grave markers (e.g., headstones, fieldstones) are absent, closed depressions formed above a grave might be the only indicator of burial. An automated method is outlined to ascertain the number of sunken graves at Oberlin Cemetery—a 13,000 m² parcel of land in Raleigh, North Carolina that served the largest Freedmen's community in Wake County. Using a modified fill-difference approach operating on a terrestrial laser scanning derived DEM, contours are created where each is described by 13 morphometrics. A binary classification tree was then used to determine the likelihood of a contour being associated with a sunken grave. From the calculated metrics, orientation and contour perimeter as well as elongation, compaction, and difference shape factors were identified as the most meaningful. Of an initial 318 sunken graves identified in the field and DEM, 238 (75%) were automatically identified by this method along with a further 210 for a total of 448 confirmed or probable sunken graves at Oberlin Cemetery.

© Copyright 2018 by John Wall

All Rights Reserved

Analysis and Characterization of Closed Topographic Depressions

by
John Wall

A dissertation submitted to the Graduate Faculty of
North Carolina State University
in partial fulfillment of the
requirements for the degree of
Doctor of Philosophy

Marine, Earth, and Atmospheric Sciences

Raleigh, North Carolina
2018

APPROVED BY:

DelWayne R. Bohnenstiehl
Committee Chair

Karl W. Wegmann

Daniel H. Doctor

Norman S. Levine

DEDICATION

This dissertation is dedicated to my parents, Teresa and John Wall.

BIOGRAPHY

I was born in Anderson, South Carolina to Teresa and John Wall. My father ran a small business focused on city planning and residential market studies, and through this I was exposed to Geographic Information Systems (GIS) and GPS at an early age; however, it would take me many years to appreciate this exposure. Following high school, I attended Tri-County Technical College for the first two years of my undergraduate career and then transferred to the College of Charleston. In December 2009, I graduated from the College with a Bachelor of Science (*cum laude*) in Anthropology and minors in Archaeology and Classics. Although I majored in anthropology, I continued to express an interest in spatial interactions, databases, and analysis much to the chagrin of some of my instructors. These interests lead to me working as a research assistant for Dr. Margaret J. Cormack and Dr. Norman S. Levine at the College of Charleston. During this time, I was formally introduced to GIS. Following this assistantship, I spent a year living abroad in Leicester and Oxford, England during which time I attend a short course at the University of Oxford on processing light detection and ranging (lidar) data for archaeological applications. Upon returning to the United States in 2011, I enrolled in the Masters of Geospatial Information Science and Technology program at NC State University. While in this program, I explored applications for lidar data at Mammoth Cave National Park and show cased this work to Dr. DelWayne R. Bohnenstiehl and Dr. Karl W. Wegmann. Following my master's in 2013, I enrolled in the Ph.D. in Marine, Earth, and Atmospheric Sciences program.

ACKNOWLEDGMENTS

Numerous people and organizations have provided support, encouragement, and advice to me throughout my time at NC State University while pursuing this degree. Beyond my parents, the utmost laudable of these individuals would be my committee members Del, Karl, Dan, and Norm. A few simple words on a page cannot express my thanks and gratitude.

I would like to thank Silvia Terzoitti for her assistance during the development of *HydroCutter*, support through further development of the tool, and providing mentorship while I worked at the U.S. Geological Survey. The Friends of Oberlin Village, especially Sabrina Goode and Cheryl Williams, for opening Oberlin Cemetery to me as a research site. Dru McGill, John Millhauser, Ruth Little, and Vincent Melomo for their assistance with devising a field investigation strategy at Oberlin Cemetery as well as discussion and insights. Field investigation at Oberlin Cemetery was principally aided by Natalia Womack, Lisa Picariello, and Morgan Whited. Their assistance through three hot and humid summer months in 2016 recording every item of material culture and topographic feature in Oberlin Cemetery was invaluable. Additional assistance at Oberlin was provided by Erik A. Bolch and Sam Levy. I would also like to thank Justin Baron and Chris Branas for their guidance on processing the terrestrial lidar at Oberlin along with providing academic licenses for Leica Cyclone.

Discussions and encouragement by other students was important to my time in the Ph.D. program; notably, Christiana Ade, Emily Barnett, Gantulga Bayasgalan, Erik Bolch, Julian Chesnutt, Gabrielle Corradino, Sam Levy, Nathan Lyons, Stephen Smith, and Parker Sprinkle.

Financial support for this work was provided by the Beck Scholarship Committee, National Speleological Society, Cave Research Foundation, Environmental and Engineering Geology Division of the Geological Society of America, Southeastern Section of the Geological

Society of America, and National Science Foundation. Without these funds, field investigation and presentation at conferences would not have been possible.

TABLE OF CONTENTS

LIST OF TABLES	viii
LIST OF FIGURES	ix

CHAPTER 1: A semi-automated tool for reducing the creation of false closed depressions from a filled lidar-derived digital elevation model	1
Abstract	2
Introduction	2
Study area and previous work	3
Methods	4
Results	5
Conclusions	7
Acknowledgements and Disclaimer	8
References	8

CHAPTER 2: Morphometric comparisons between automated and manual karst depression inventories in Apalachicola National Forest, Florida, and Mammoth Cave National Park, Kentucky, USA.....	10
Abstract	11
Introduction	12
Background	14
<i>Formation of karst depressions</i>	14
<i>Inventorying karst depressions</i>	14
<i>High-resolution topographic data from lidar</i>	15
Study areas	15
Data	17
Methods	18
<i>Automated inventorying using a fill-difference routine</i>	18
<i>Testing the impact of data resolution</i>	18
<i>Comparisons with existing state inventories</i>	20
<i>Catalog validation</i>	20
Results and discussion	22
<i>Catalog comparisons</i>	22
<i>Distribution of depressions</i>	23
<i>Impact of data resolution</i>	25
<i>Newly identified depressions</i>	27
Conclusions	28
Acknowledgements	28
References	28

CHAPTER 3: A novel workflow for identifying sunken graves utilizing ultra-high-resolution topographic data and machine learning.....	32
Abstract	33
Introduction	35
<i>Methodological background and motivation</i>	35

<i>Geomorphology, geology, and pedology</i>	37
Data and Methods	37
<i>Topographic survey</i>	37
<i>Field observations</i>	38
<i>Grave detection from ultra-high-resolution topographic data</i>	39
<i>Classifying detections with machine learning</i>	40
Results.....	41
Discussion.....	42
Conclusions.....	44
Acknowledgements.....	45
References.....	45
Appendix.....	65
APPENDIX A: A geospatial and geoarchaeological investigation of an African-	
American Cemetery in Raleigh, North Carolina, U.S.A.	66
Abstract.....	67
Introduction.....	69
Historical and cartographic analysis	71
Previous surveys of Oberlin Cemetery	73
Field Methods	74
<i>Terrestrial laser scanning survey</i>	74
<i>Pedestrian survey</i>	75
<i>Ground penetrating radar survey</i>	76
Results.....	77
<i>Cultural materials and burials</i>	77
<i>Enclosures and family plots</i>	79
<i>Demography</i>	80
Discussion	81
<i>Database comparison</i>	81
<i>Unmarked grave identification</i>	82
Summary and conclusions	83
Acknowledgements.....	85
References.....	85
Appendices.....	107
<i>Appendix A.1: Other material culture records</i>	107
<i>Appendix A.2: Field identified Oberlin Cemetery death registry</i>	109
<i>Appendix A.3: Family plot and marker records</i>	115

LIST OF TABLES

Chapter 2

Table 1	Area and maximum depth quartiles for manually and automatically generated karst depression catalogs at Mammoth Cave National Park (MACA) and Apalachicola National Forest (ANF).	23
Table 2	Success rates from re-gridding the MACA lidar derived DEM and creating depression catalogs.....	26

Chapter 3

Table 1	Field recorded metrics for sunken graves at Oberlin Cemetery	53
Table 2	Tested annulus inner and outer radii to determine optimal values. Capture ratio is calculated by: 1) converting contours to polygons; 2) thresholding polygons to two standard deviations of the observed area ($1.00 \text{ m}^2 < A_{field} < 2.72 \text{ m}^2$); and 3) and using a Select by Location on field observations ($n = 318$). This identified 0.70 m inner and 0.90 m outer radii (italicized) as optimal with a capture ratio of 90%	56
Table 3	Calculated shape factors from derived contour-polygon metrics.....	57

Appendix A

Table 1	Counts of records identified as monuments, monuments & sunken graves, and graves with material culture in disrepair identified as well.....	97
Table 2	Records identifying unique burials.....	98
Table 3	Field recorded metrics of sunken graves at Oberlin Cemetery described by inclusive percentile measurements. Depth and width measurements were not always determinable in the field. Depth was indeterminate for two records, OC0192 and OC0760, due to dense vegetation and subtle topographic expression. Width was also indeterminate for OC0192 because of this vegetation	99

LIST OF FIGURES

Chapter 1

- Figure 1 (A) Digital Elevation Model of the Boyce 7.5-minute quadrangle with a draped hillshade. Intersections between NHD Streams, railways and roads. (B) An initial fill difference raster map illustrates ponding behind artificial dams created by railways and roads. The fill difference raster is created by subtracting the initial DEM from the filled DEM. (C) The second and third iterations of intersections identified by the Cutter tool are shown. Note the increase in intersections found between both of these iterations, which directly corresponds to the different flow accumulation thresholds (400,000 m² and 10,000 m²) used 3
- Figure 2 Data quality is important to consider when running Hydrocutter toolbox. Note the issues with the railway presented here. The initial railway data (dashed red line) is offset from the edited railway (dark brown solid line)..... 4
- Figure 3 Work flow of the Cutter tool within the Hydrocutter toolbox 5
- Figure 4 (A) Red points indicate the initial intersections found between NHD stream data with roads and railway data. These are compared to (B) green and yellow points which are the intersections found between the 400,000 m² and 10,000 m² stream lines respectively and transportation routes. As indicated by panels A and B, the stream lines with the lower flow accumulation extend further upstream and therefore intersect a greater number of roads. (C) A detail of these differences is illustrated between initial intersections and subsequent iterations of the Hydrocutter tool resulting in differences of stream dataset quality highlighted particularly in the left half of the panel 6
- Figure 5 Depressions identified by Hydrocutter are compared to manually identified depressions. Note that some of the manually identified closed depressions are grouped into one closed depression using the results of Hydrocutter suggesting a coalescence of closed depressions which are not easily identified by manual interpretation 7
- Figure 6 Future development for this toolbox is illustrated by (A) The original elevation surface shown with the NHD flow line and road intersection, (B) grid cells matching the NHD were recalculated with the minimum elevation value within the buffer zone to create hydrologic connectivity. The red areas indicate false depressions that remain, (C) The least cost path through the buffer zone is used to identify the cells to calculate as the flow path through the topographic high..... 8

Chapter 2

Figure 1	Karst-susceptible regions of the contiguous United States. The Mammoth Cave National Park, Kentucky and Apalachicola National Forest, Florida field sites are indicated by stars (Weary and Doctor, 2014).....	13
Figure 2	Hillshaded digital elevation models of (A) Mammoth Cave National Park and (B) Apalachicola National Forest created from light detection and ranging (lidar) data. Statewide inventoried karst depressions, major roads, and urban areas are indicated.	16
Figure 3	Percent canopy cover for the contiguous United State (Homer et al., 2015). Note the change in scale between 90 and 100%, used to highlight the most dense canopy cover. Field sites are indicated by <i>stars</i>	17
Figure 4	The workflow used in this study for karst depression inventorying and parameterization within a Geographic Information System.....	19
Figure 5	Cumulative Distribution Functions (CDFs) for the Statewide (blue) and Lidar Inventories for area and depth parameters at Mammoth Cave National Park (A & B) and Apalachicola National Forest (C & D). At Mammoth Cave National Park, the empirical distribution of features with areas > 1,456 m ² and depths > 5.3 m are statistically identical between the two catalogs. At Apalachicola National Forest, the empirical distribution of features with areas > 5,620 m ² and depths > 2.64 are statistically identical between the two catalogs.....	21
Figure 6	Boxplots depicting quartiles for the distribution of areas and maximum depths of manually and automatically generated karst depression catalogs at Mammoth Cave National Park (A & B) and Apalachicola National Forest (C & D). Maximum depths for manually generated karst depressions were derived from the processed lidar derived digital elevation models.....	22
Figure 7	An example of a false-positive karst depression included in the Statewide Inventory of Kentucky. (A) Map-view of the lidar data with the misidentified karst depression in association with other manually and automatically identified karst depressions. (B) This lidar data is compared to the USGS 1:24,000-scale (20 ft. contour interval) Cub Run topographic quadrangle showing how the hill was represented as a closed depression on the quadrangle. (C & D) Topographic profiles illustrating that the false-positive karst feature is indeed a topographic high, as indicated by the grey shading. This false positive was not detected by the automated method and should not be included in an inventory of karst depressions	24

Figure 8 The two most extreme one-to-many relationships at each location are shown. (A) At Mammoth Cave National Park, several smaller karst depressions are aggregated by the automated method. This feature is bounded in the northwestern corner by a raised road which restricts its estimated extent. While this is evident here, similarly bounded features are minimal-to absent from the rest of the dataset. (B) Conversely, at Apalachicola National Forest, the most extreme one-to-many relationships are likely due to triangulation artifacts resulting from the data being gridded at too fine of a resolution given the ground point density 25

Figure 9 Application of the Logarithmic Size Ratio to aid in identifying biases in recording metrics by the manual and automated karst depression cataloging methods for area and maximum depth at Mammoth Cave National Park (A & B) and Apalachicola National Forest (C & D) 26

Figure 10 A digital elevation model with a hillshade showing newly identified karst depressions at the Leon Sinks Geological Area within Apalachicola National Forest 27

Chapter 3

Figure 1 (A) Raleigh is located in central North Carolina. (B) Just north-west of downtown Raleigh, Oberlin Cemetery (pink square) occupies a 3.2-acre (1.3-hectare) plot of land. (C) To the north of the cemetery (pink hachured square) are the Oberlin Court Apartments while to the south are the Cameron Village Condominiums. Flanking the cemetery to the east and west are the Occidental Life Insurance and InterAct office buildings, respectively 49

Figure 2 (A) Locations for 26 scans (blue dots) that were carried out with a Leica HDS3000 Terrestrial Laser Scanner (TLS) within Oberlin Cemetery. Planned scans at four locations (pink crosses) could not be conducted due to dense vegetation. These scans were combined into a unified point cloud within Leica Cyclone. Ground returns were identified and classified with LAStools. (B) Vertical accuracy of elevation values within a 0.10 m grid was assessed using the standard deviation of elevation values within each cell ($\mu = 0.01$ m). (C) Using this grid resolution of 0.10 m, 13.38% of cells had ≤ 1 point per cell (dark grey) while 86.62% have two or more points per cell. Optimally constrained cells had 2 to 19 points per cell. Most of the sub-optimally constrained cells were in areas of dense vegetation. (D) A digital elevation model (DEM) was gridded from ground classified points where cells with ≤ 1 point per cell were interpolated from TLS points located within two meters. Color-shading shows the derived DEM with a draped slope-shade 50

Figure 3 Distribution of field observed sunken graves which could also be identified in the terrestrial laser scanning derived digital elevation model ($n = 318$). The majority ($n = 265$) of these sunken graves were identified without associated

	material culture (grey dots) while 53 were associated with headstones, fieldstones, flower holders and other material culture (blue dots)	52
Figure 4	A schematic for automatically identifying sunken graves within an ultra-high-resolution digital elevation model (DEM). An initial DEM is locally detrended using a Topographic Position Index (TPI) with an annulus window. The TPI is then hydrologically conditioned using the <i>Fill</i> tool within the ArcGIS <i>Hydrology Toolbox</i> . This fills depressions within the TPI such that synthetic streamflow would be routed over depressions and to the edge of the raster. The initial TPI is then subtracted from the filled TPI to create a depth raster which is contoured with an interval equal to the vertical accuracy of the DEM (0.01 m). These contours are then converted to polygons and thresholded during processing to two standard deviations from the observed mean grave area ($1.00 \text{ m}^2 < A_{\text{field}} < 2.72 \text{ m}^2$). Conversion must happen in a for-loop within Python, ArcGIS Model Builder, or equivalent. A simple conversion to polygons (i.e. <i>Feature to Polygon</i> in ArcGIS) results in the intra-contour spacing being converted to polygons opposed to the entire area that the contour covers.....	54
Figure 5	Examples of closed-contours, with a 0.01 m interval, manually classified as ‘likely’ sunken graves (green lines) for training a binary classification tree. A slope-shaded digital elevation model is shown in the background. (A) When concentric closed-contours were associated with field identified sunken graves (green dots), only the two outer-most contours were classified. Remaining contours were left ‘unclassified’ (purple lines) and were not used for training and validation. (B) Closed-contours associated with field observation and classified as ‘likely’ despite having less idealized shapes. (C) Closed-contours not associated with field identified sunken graves and classified as ‘unlikely’ (red lines).....	58
Figure 6	Pruned binary classification tree created from 734 training contours. Predictor selection was determined using the interaction-curvature method. Splitting was determined using Gini’s diversity index while pruning used the $1 - SE$ rule. Using a ten-fold cross-validation method, the classification error is 18.05%. Note that not all metrics from <i>Table 3</i> are used in this classification tree	59
Figure 7	Predictor importance for the pruned classification tree. Of the 13 predictors, only orientation, contour perimeter (P_c), elongation factor (F_{elong}), and difference factor (F_{diff}) were identified as meaningful. The estimated value is calculated by summing the changes in risk due to splits on every predictor and dividing the sum by the number of branch nodes	60
Figure 8	Confusion matrix created from test contours	61

Figure 9 A total of 1,039 contours were classified as ‘likely’ to be associated with sunken graves. Of these, 844 contours spatially collocated with 238 of the graves identified during the pedestrian survey (blue polygons). An additional 305 contours (green polygons), describing 210 features, were identify as ‘likely’ associated with sunken graves based on their morphometric properties. For visualizaton, overlapping polygons were dissolved into one another 62

Figure 10 Pink crosses denote the locations of 32 sunken graves whose defining contours had areas outside two standard deviations of field observed sunken graves ($A_{field} < 1.00 \text{ m}^2$; $A_{field} > 2.72 \text{ m}^2$). Red crosses denote the location of 48 field-identified sunken graves with contours that were misclassified by the decision tree 63

Figure 11 (A) Example of a closed-contour (pink lines, $A_C = 5.42 \text{ m}^2$) that exceeded the area threshold due to graves (pink crosses) coalescing into one another. (B) Examples of graves not identified as ‘likely’ sunken graves (red) by the binary classification tree due to having deferring morphologies from training polygons... 64

Appendix A

Figure 1 (A) Raleigh is located in central North Carolina. (B) Just north-west of downtown Raleigh, Oberlin Cemetery (pink square) occupies a 3.2-acre (1.3-hectare) plot of land. (C) To the north of the cemetery (pink hachured square) are the Oberlin Court Apartments while to the south are the Cameron Village Condominiums. Flanking the cemetery to the east and west are the Occidental Life Insurance and InterAct office buildings, respectively. 88

Figure 2 Modern extent of Oberlin Cemetery (pink hatched polygon) compared to two historic maps. (A) The modern extent occupies land identified as Pettiford’s in an 1865 map of Confederate lines around Raleigh, North Carolina. (B) A map created in 1920 by C.L. Mann from compiled survey, deed survey notes, and historic surveys indicating that the land was sold by George W. Mordecai to Jesse Pettiford in 1858. The boundary for Pettiford’s land is noted on Mann’s map as being re-surveyed in 1910..... 89

Figure 3 A survey plat map created by Harry Tucker of Pine View Cemetery which was created by John Jerome Turner in 1922. Pine View abutted Oberlin Cemetery to the south and is now collectively identified as part of Oberlin Cemetery, although sometimes identified as an annex. The plat indicates the annex contains 136 lots, or family plots, measuring 18.58 m^2 (200 ft^2), each. 90

Figure 4	Modern extent of Oberlin Cemetery (light blue hatched polygon) compared to United States Geological Survey (USGS) (A) topographic data and (B) aerial photography. The 15'-topographic map from 1943 does not show Oberlin Cemetery nor Oberlin Graded School but does show the historically white Broughton High School a short distance away. Aerial photography from 1968 shows Oberlin Graded School (below blue arrow) immediately to the west of the Cemetery. The Cemetery is wooded with a contiguous wooded appendage extending west from the northwestern corner. Although the land-cover between the appendage and cemetery are the same, the land-use is indeterminate.....	91
Figure 5	Locations for 26 scans (blue dots) carried out with a Leica HDS3000 Terrestrial Laser Scanner within Oberlin Cemetery. These scans were combined into a unified point cloud within Leica Cyclone. Color-shading shows the derived digital elevation model created from these data. Planned scans at four locations (pink crosses) could not be conducted due to dense vegetation.....	92
Figure 6	A customized data entry form was created for the work at Oberlin Cemetery using Trimble's TearraFlex application. Point and polygon data could be recorded with each point having an associated estimated accuracy with it. A unique identification number was given to each marker along with date and time stamp and field photos. Subsequent fields were dynamically exposed depending on prior values entered by the user. Shown here are fields exposed based on answering "Monument (only)" for the question "What are you recording?" Beyond recording metrics and inscriptions, if present, spatial relationships were also recorded, such as existing in an enclosure or other associated markers. Finally, the person recording the marker had to sign their initials to close the form.	93
Figure 7	Items of material culture identified within the cemetery were grouped into (A) Carved Stones, (B) Cement Markers, (C) Fieldstones, (D) Metal Plaques, (E) Wooden headboards, and (F) Other. Other was a catch-all term for any material culture that did not fit neatly into the other five categories. Features shown with a graduated scale in 1, 2, 5, and 10-centimeter intervals.....	94
Figure 8	Geophysical survey using Ground Penetrating Radar was carried out on 12% of the Cemetery in six grids (pink hatched polygons). Both 250 and 500 MHz antennae were used at each grid with a line spacing of 0.5 m in a north-south (grave-normal) orientation	95
Figure 9	Locations of sunken graves with point color indicating which quartile the grave's depth fit into from Table 3. Sunken graves within the fourth quartile appear to cluster along the middle portion of the southern edge; however, similarly deep values are found dispersed throughout the cemetery.....	99

Figure 10	Family plots (pink hatched polygons) and family plot markers without enclosures (pink dots). Last names on markers and counts of records within enclosure are described in text as well as Appendix A.3	100
Figure 11	Distribution of (A) birth (n = 128) and (B) death (n = 142) dates found within Oberlin Cemetery. Count of individuals by decade are shown in comparison to the cumulative distribution of records for each graph. Thus, from grave markers with inscribed birth and/or death dates, 50% of individuals buried at Oberlin were born before 1885 while 50% died by 1935.....	101
Figure 12	Age at death by decade of birth for individuals found within Oberlin Cemetery. N.B. there is a graph break between 1939 and 1960.....	102
Figure 13	Spatial distribution of burials with inscribed death dates symbolized by decade. There is no clear indication of clustering prior to 2000. Following 2000, burials cluster in the southwestern corner of the Cemetery	103
Figure 14	Examples of social organizations on grave markers at Oberlin Cemetery. (A) The Prince Hall branch of the Freemasons, (B) Ancient Order of Oddfellows, and (C) Eastern Star Lodge of the Freemasons. Iconography and inscriptions shown with a graduated scale in 1, 2, 5, and 10-centimeter intervals.	104
Figure 15	(A) Ground Penetrating Radar radargram created from 250 MHz antennae from A to A'. Data are visualized after applying a de-WOW filter, SEC2 gain, and background subtraction. Blue arrows indicate decoupling of the antennae due to depressions associated with sunken graves. These depressions are evident in (B) topographic data recorded with a terrestrial laser scanner and were inventoried during the pedestrian survey. (C) A topographic profile created from the digital elevation model additionally show the sunken graves.	105

CHAPTER 1

A semi-automated tool for reducing the creation of false close depressions from a filled lidar-derived digital elevation model

Chapter 1 was published in the *Proceedings of the Fourteenth Multidisciplinary Conference, October 5-9, Rochester Minnesota* in 2015 with the following co-authors:

Doctor, D. H.¹; Terziotti, S.²

¹U.S. Geological Survey, Reston, Virginia, USA

²U.S. Geological Survey, Raleigh, North Carolina, USA

A SEMI-AUTOMATED TOOL FOR REDUCING THE CREATION OF FALSE CLOSED DEPRESSIONS FROM A FILLED LIDAR-DERIVED DIGITAL ELEVATION MODEL

John Wall

Department of Marine, Earth & Atmospheric Sciences, 2800 Faucette Drive, Room 1125 Jordan Hall Campus Box 8208, NC State University, Raleigh, NC, 27695-8208, jwall@ncsu.edu

Daniel H. Doctor

U. S. Geological Survey, 12201 Sunrise Valley Drive, Reston, VA, 20192, dhdoctor@usgs.gov

Silvia Terziotti

U. S. Geological Survey, 3916 Sunset Ridge Road, Raleigh, NC, 27607, seterzio@usgs.gov

Abstract

Closed depressions on the land surface can be identified by ‘filling’ a digital elevation model (DEM) and subtracting the filled model from the original DEM. However, automated methods suffer from artificial ‘dams’ where surface streams cross under bridges and through culverts. Removal of these false depressions from an elevation model is difficult due to the lack of bridge and culvert inventories; thus, another method is needed to breach these artificial dams. Here, we present a semi-automated workflow and toolbox to remove falsely detected closed depressions created by artificial dams in a DEM. The approach finds the intersections between transportation routes (e.g., roads) and streams, and then lowers the elevation surface across the roads to stream level allowing flow to be routed under the road. Once the surface is corrected to match the approximate location of the National Hydrologic Dataset stream lines, the procedure is repeated with sequentially smaller flow accumulation thresholds in order to generate stream lines with less contributing area within the watershed. Through multiple iterations, artificial depressions that may arise due to ephemeral flow paths can also be removed. Preliminary results reveal that this new technique provides significant improvements for flow routing across a DEM and minimizes artifacts within the elevation surface. Slight changes in the stream flow lines generally improve the quality of flow routes; however some artificial dams may persist. Problematic areas include extensive road ditches, particularly along divided highways, and where surface flow crosses beneath road intersections. Limitations do exist and the results partially depend on the quality of data being input. Of 166 manually identified culverts from a previous study by Doctor and Young in 2013, 125 are within 25 m of culverts identified by this tool. After three iterations, 1,735 culverts were identified and cataloged. The result is a reconditioned

elevation dataset, which retains the karst topography for further analysis, and a culvert catalog.

Introduction

The identification of closed depressions within a landscape is important for karst studies; however the automated creation of closed depression catalogs are hampered in urban locations. Automated depression delineation and cataloging methods have been discussed elsewhere (e.g., Lindsay and Creed, 2006; Zandbergen, 2010; Doctor and Young, 2013). Of these methods, the filling method (subtracting an initial digital elevation model (DEM) from the DEM with depressions filled to spill points) tends to be preferred due to the ease and speed by which a catalog can be generated. However, in populated areas simulated water flow tends to pond behind roads, railways, and other man-made surface features resulting in falsely detected closed depressions. These problems are especially acute when using high-resolution topographic datasets such as Light Detection and Ranging (lidar), but are not unique to these DEMs. There are a number of methods to deal with these false depressions, but care has to be taken when working within karst terrain as these depressions are likely to be real and of interest to further research (Zandbergen, 2010; Lindsay and Creed, 2006).

Current means to remove topographic barriers use either manual or digital methods. Manual methods require the digitization of lines (here collectively referred to as ‘culverts’) representing underpasses beneath roads, driveways, railways, or other obstructions to actual stream flow using either aerial or field observations. As to be expected, these methods are very time consuming. Following the digital creation of a culvert inventory, this dataset is then used as input into a variety of techniques to ‘cut’ or ‘burn’ the culverts into the elevation data. This

‘burning’ method normally uses the entire stream network to hydrologically condition the surface (e.g., Mitasova et al., 1999; Maidement, 2002; Tarbonton, 2012). However, these methods can be difficult to implement, or can create steep canyons in the hydrologically corrected elevation data potentially causing errors in further analysis, particularly when streams represented as vector lines do not accurately match the elevation surface. Current methods are too aggressive for karst terrain resulting in true depressions being scrubbed from the elevation dataset. For example, the optimized cut and fill tool (Jackson, 2013) would result in the removal of true depressions. Additionally, other tools such as those developed by Poppenga et al. (2010) require thresholds (i.e. area and depth) be set which could result in smaller, artificial depressions being missed.

The goal of this study was to develop an ArcGIS toolbox to identify potential culvert locations which could then be enforced into the elevation data, thereby removing false closed depressions within karst terrain. This is done by finding the intersection of transportation routes and stream lines which are then buffered and used to lower

the elevation across the man-made topography. This method minimizes the extent of DEM modification in order to retain the karst depressions. A semi-automated approach is taken with user-provided data and thresholds.

Study area and previous work

The study area is the Boyce 7.5-minute quadrangle predominantly covering Clarke County with smaller portions of Warren and Fredrick Counties in Virginia (Figure 1). The region spans roughly 150 km². Located within an extensive karst region of the Great Valley physiographic province of the Appalachian mountain range, the Boyce quadrangle covers part of the Shenandoah River drainage basin.

Details on the geology of the quadrangle can be found in Edmundson and Nunan (1973). Karstification in the study area has resulted in a mature dissected karst surface of moderate to low relief, with 90 m total elevation range and a mean elevation of 180 m above sea level. Sinkholes and other karstic depressions generally occur as a result of cover-collapse or suffosion processes within the residuum overlying the carbonate bedrock;

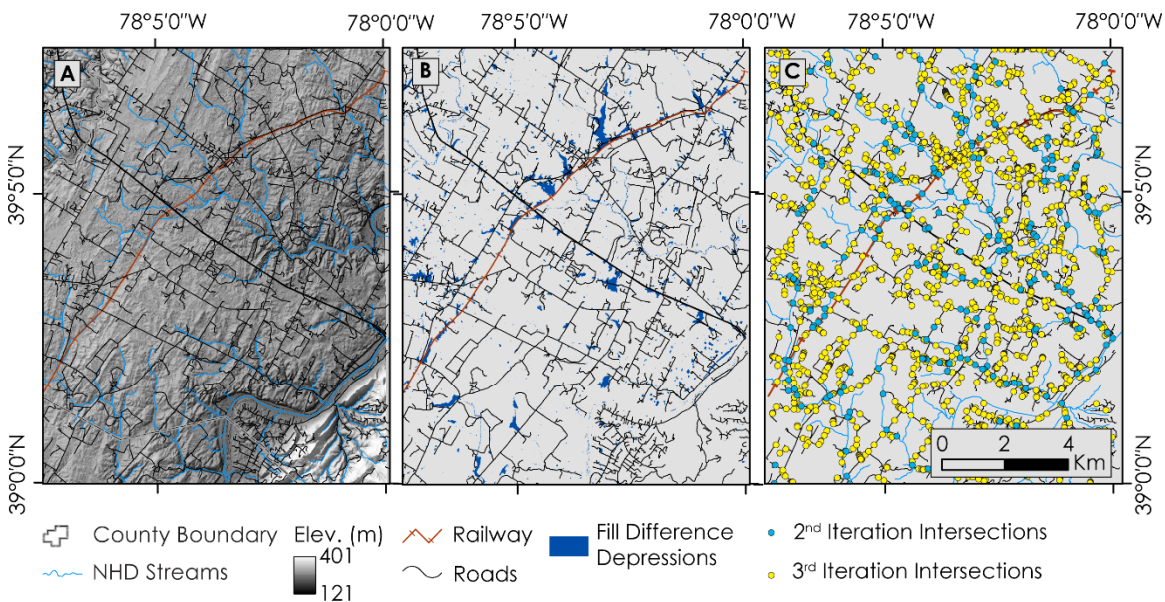


Figure 1. (A) Digital Elevation Model of the Boyce 7.5-minute quadrangle with a draped hillshade. Intersections between NHD Streams, railways and roads. (B) An initial fill difference raster map illustrates ponding behind artificial dams created by railways and roads. The fill difference raster is created by subtracting the initial DEM from the filled DEM. (C) The second and third iterations of intersections identified by the Cutter tool are shown. Note the increase in intersections found between both of these iterations, which directly corresponds to the different flow accumulation thresholds (400,000 m² and 10,000 m²) used.

the thickness of residuum varies between zero and ten meters.

Doctor and Young (2013) presented an evaluation of an automated workflow for identifying closed depressions in the Boyce quadrangle using a simple fill-difference method. This method uses the difference between a ‘filled’ DEM raster and the original raster, and was compared to manually-delineated closed depressions. They concluded that the primary hindrance to a fully-automated process for identifying closed depressions was the presence of artificial ‘dams’ in the elevation surface where streams pass beneath transportation routes. For that study, stream underpasses, usually in the form of culverts, were identified from aerial imagery and field work, and were manually added as an input layer used to recondition the original DEM allowing streams to flow through elevation obstructions such as those created by transportation routes. Although this approach was effective, it was tedious and was not successful in identifying all possible culverts within the quadrangle thereby impacting the closed depression catalog count and morphometrics. Thus, a new automated method to identify stream underpasses was deemed necessary.

Methods

The method presented here for reducing the creation of false closed depressions was developed using ArcGIS tools. For this work, ArcGIS 10.2.2 was used, but the models should work with any 10.X version of ArcGIS. Additionally, a license for the Spatial Analyst Tools is necessary.

Three vector datasets were acquired covering streams, railways and road networks along with a high-resolution lidar raster data set. Stream data were acquired from the United States Geological Survey’s (USGS) National Hydrologic Dataset (NHD). Railways and roads were acquired from the USGS National Map. All vector datasets were digitized at the 1:24,000 scale, which is much coarser resolution than the lidar data. This resulted in the need to manually correct the railway shapefile (Figure 2). The resulting corrected vector data was used as input into the tools. The lidar dataset was acquired between 1 March and 9 March 2011. Acquisition took place during leaf-off conditions and after snow cover melted. The vertical RMSE was 9.0 cm while the point spacing was 1.0 m.

The Hydrocutter toolbox contains two tools: Hydro and Cutter. Together, these tools can be run iteratively in a semi-automated way employing user thresholds. Hydro simply implements a stream definition method as determined using the Fill, Flow Direction, and Flow Accumu-

lation tools provided by ESRI within the Spatial Analyst à Hydrology toolbox. The result of the Hydro tool is a vector dataset which can be used as an input into Cutter. Cutter topographically enforces culverts where streams pass beneath topographic highs, generally along transportation routes, thereby providing a flow path across the artificial obstruction in the DEM and reducing false closed depressions.

The Processing Extent, Snap Raster, and Cell Size are all set to the DEM provided by the user within the tool environments automatically so that they do not need to be set by the end-user.

The workflow for the Cutter tool is outlined by Figure 3 and described in detail here. Transportation vector datasets are intersected with an initial NHD stream vector dataset. This results in two point datasets (one for railways and one for roads, respectively) which are then merged into a single point dataset representing all intersections with streams (i.e. culverts). These culverts are then buffered by a user-defined value which should span the widest railway or road. For this study, a 25 m buffer diameter around each point was used. The circular buffer polygons are then used to clip the stream vector line to provide stream segments where the streams cross the transportation routes. A Zonal Fill tool is then used to find the minimum elevation along the clipped vector segments (ESRI, 2012). This results in a raster layer which

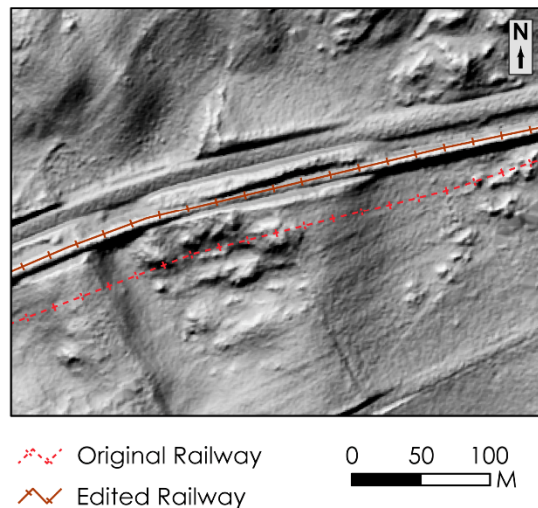


Figure 2. Data quality is important to consider when running Hydrocutter toolbox. Note the issues with the railway presented here. The initial railway data (dashed red line) is offset from the edited railway (dark brown solid line).

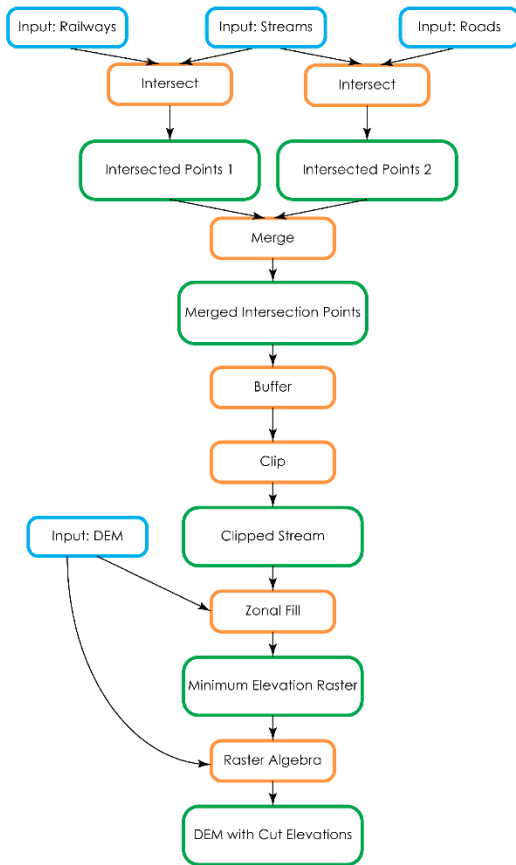


Figure 3. Work flow of the Cutter tool within the Hydrocutter toolbox.

is used to enforce this minimum elevation value into the DEM thereby hydrologically conditioning it.

This conditioned DEM is used as input into the Hydro tool. The only additional information that must be provided when running the Hydro tool is a threshold value for the flow accumulation. For this study area, a flow accumulation value of 400,000 m² was found to reasonably approximate the lengths of the NHD stream vector lines and was therefore used for the initial iteration of this tool.

The Hydrocutter toolbox was run on the lidar data covering the Boyce quadrangle. The initial iteration of the Cutter tool used the NHD streams and edited roads and railway data as input. The resulting DEM was then used as input into the Hydro tool and a flow accumulation threshold of 400,000 m² was used to approximate the surface flow accumulation of the NHD streams.

A second hydrologic conditioning iteration was carried out using newly defined 400,000 m² flow accumulation streams and transportation routes, and then the Hydro tool was repeated using a flow accumulation of 10,000 m². After the DEM had been reconditioned to account for intersections between the stream lines of 10,000 m² flow accumulation, stream lines at 2,000 m² flow accumulation were generated for visual comparison and validation.

Given the different approaches, the closed depressions catalogs identified after running the Hydrocutter toolbox described here and those of Doctor and Young (2013) are not directly comparable; however, here we heuristically compare these datasets.

Results

Using the Hydrocutter toolbox approximately 14 times as many culverts and stream intersections with transportation routes were found as those identified manually within the Boyce quadrangle. Of these, 75% were coincident with culvert lines from Doctor and Young (2013) within a 25 m buffer zone.

The 2,000 m² flow accumulation stream lines often represent flow routes across the DEM surface that do not have any obvious geomorphic expression of surface runoff, such as channels, swales, gullies, etc. Thus, stream lines having flow accumulation values less than 10,000 m² are not used here to define additional culverts. As a result, the 10,000 m² flow accumulation stream lines identified the majority of topographically evident stream channels as well as creating an inventory of potential culverts (Figure 4).

Doctor and Young (2013) manually identified 166 culverts of which 106 were verified by aerial imagery or field checking. Of the manually identified culverts 125 are within 25 m of the Hydrocutter culverts, 80 of these were verified. The first pass of the Hydrocutter toolbox found 260 intersections between the NHD stream vector lines and the transportation vector lines; these intersections were indicative of possible stream culverts. These culverts were burned into the original DEM, and used to generate a new stream vector line dataset that was more representative of the actual lidar-derived elevation model. The next iteration used lidar generated stream lines with a flow accumulation of 400,000 m² thus mimicking the original NHD vector stream lines and identified 272 culverts. The final iteration, using a flow accumulation of 10,000 m, identified 1,735 culverts.

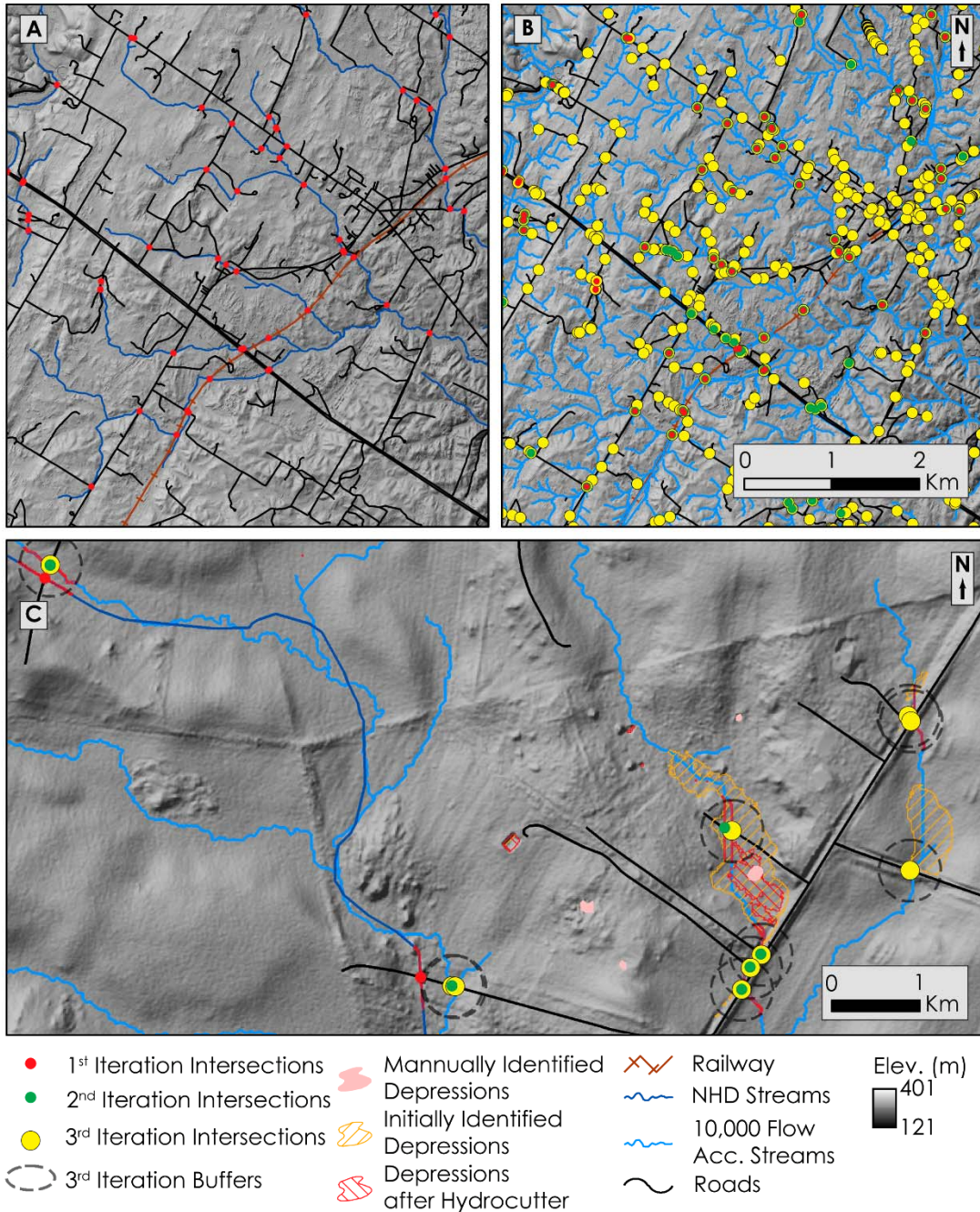


Figure 4. (A) Red points indicate the initial intersections found between NHD stream data with roads and railway data. These are compared to (B) green and yellow points which are the intersections found between the 400,000 m² and 10,000 m² stream lines respectively and transportation routes. As indicated by panels A and B, the stream lines with the lower flow accumulation extend further upstream and therefore intersect a greater number of roads. (C) A detail of these differences is illustrated between initial intersections and subsequent iterations of the Hydrocutter tool resulting in differences of stream dataset quality highlighted particularly in the left half of the panel.

Conclusions

The Hydrocutter toolbox provides two products useful in karst studies. The first is a hydrologically conditioned DEM by removing obstructions to flow routing that cause false closed depressions resulting from the impoundment of water behind man-made features such as roads. The second is an inventory of potential culverts which is not only useful to karst studies, but the broader geologic, hydrologic, and environmental management communities.

Nevertheless, there are several known issues and pieces of cautionary advice that come with using this tool. First, the user-defined buffer distance around intersections needs to be large enough to allow impoundments to be breached. This can be problematic when road widths are variable and span a greater width than the buffer distance used to define the ‘cutting’ of culverts. Second, in the Boyce quadrangle a flow accumulation of 10,000 m² was determined as reasonable to represent surface water flow routes when compared to the topographic expression of the surface hydrology; however, this is not a constant value, meaning that a user should determine a reasonable flow accumulation value empirically for their study area by examining the correspondence between the elevation model and the stream lines generated. Third, errors due to poor vector data quality compared to the lidar data can be propagated through the analysis. Therefore, high accuracy of the vector data used as the initial inputs to the process is important. If good vector datasets are unavailable, manual editing to 1:24,000 scale vector data to match the lidar elevation model might be necessary, as was done here. Fourth, some re-routing of stream lines can occur between iterations of the Hydrocutter tools. This is localized to areas within or near the buffer zones of intersections (Figure 4).

The process outlined here generally improves the overall representation of flow across the DEM. It is only problematic in areas where the initial road or NHD stream data is poor. Thus, as with many tools, the quality of the data being input into the tool is inherently representative of the data quality coming out of the tool.

Although further quantitative comparison is necessary, the Hydrocutter toolbox is better at breaching man-made impoundments while preserving the natural closed depression landscape within karst terrain (Figure 5). This is vital to creating closed depression catalogs generated from lidar datasets rather than statewide inventories which adequately represent the closed depression population while minimizing false detections (Wall & Bohentstiel, 2014).

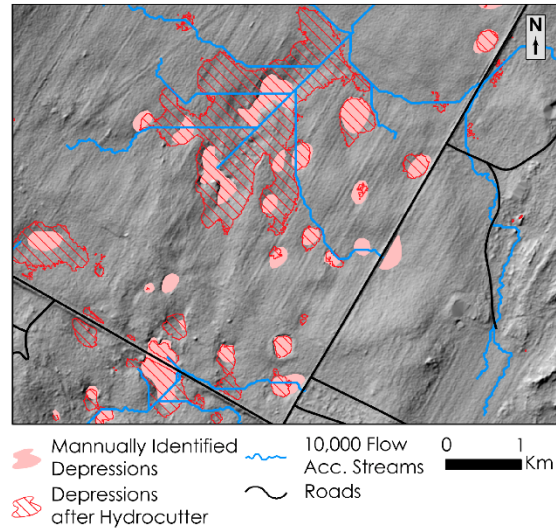


Figure 5. Depressions identified by Hydrocutter are compared to manually identified depressions. Note that some of the manually identified closed depressions are grouped into one closed depression using the results of Hydrocutter suggesting a coalescence of closed depressions which are not easily identified by manual interpretation.

A possible future refinement of the toolbox would be to improve the manner in which the location of a stream pathway is delineated across an impoundment. Using the current Cutter tool, the pathway follows the pre-existing stream line that crosses an obstruction. If the stream vector is not in the correct location (i.e. where a culvert or underpass is), then errors may result which could be propagated through the analysis. Clipped streams segments may not fully connect the actual stream channels in the lidar surface. Figure 6 illustrates a possible solution which would employ a least-cost path approach within the buffer zone of intersection to optimize the likelihood of connecting the lowest point on either side of the obstruction (Poppenga et al., 2010).

Future work will focus on implementing a hybrid method between the Cutter tool and least cost path technique. This will allow for more accurate connections between low points within the buffer zone. Ideally, this will be more representative of stream flow routes and culvert locations. It will have an added benefit of further reducing false closed depressions.

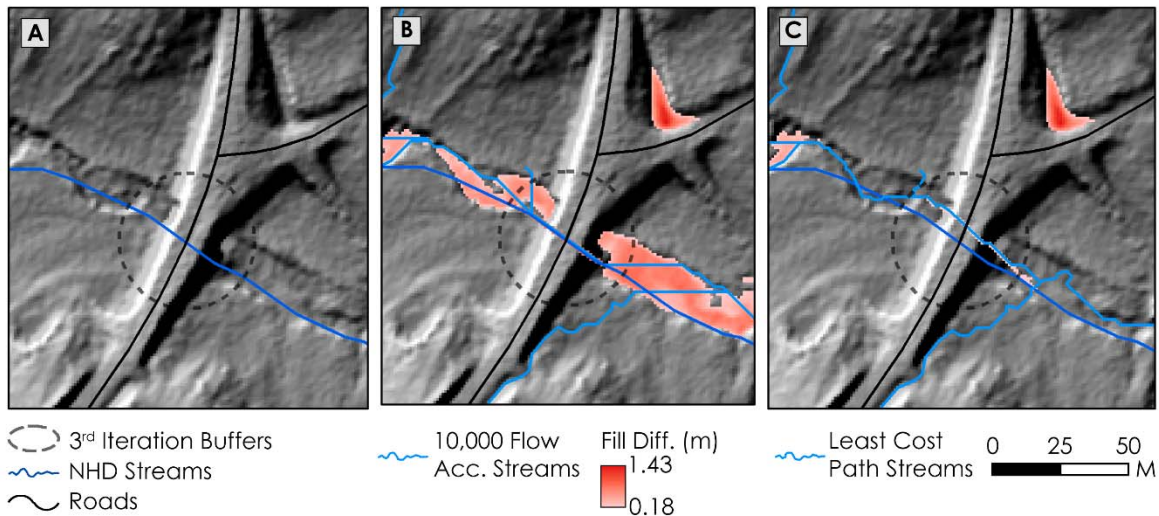


Figure 6. Future development for this toolbox is illustrated by (A) The original elevation surface shown with the NHD flow line and road intersection, (B) grid cells matching the NHD were recalculated with the minimum elevation value within the buffer zone to create hydrologic connectivity. The red areas indicate false depressions that remain, (C) The least cost path through the buffer zone is used to identify the cells to calculate as the flow path through the topographic high.

Acknowledgments and Disclaimer

We wish to thank John Young (USGS), Alan H. Rea (USGS), and Brian Bruckno (Virginia Dept. of Transportation) for helpful reviews. Although these data have been processed successfully on a computer system at the U.S. Geological Survey (USGS), no warranty expressed or implied is made regarding the display or utility of the data on any other system or for general or scientific purposes, nor shall the act of distribution constitute any such warranty. The USGS or the U.S. Government shall not be held liable for improper or incorrect use of the data described and/or contained herein. Any use of trade, firm, or product names is for descriptive purposes only and does not imply endorsement by the U.S. Government.

References

Doctor DH, Young JA. 2013. An evaluation of automated GIS tools for delineating karst sinkholes and closed depressions from 1-meter lidar-derived digital elevation data. In: Land L, Doctor DH, Stephenson JB, editors. Sinkholes and the Engineering and Environmental Impacts of Karst: Proceedings of the Thirteenth Multidisciplinary Conference, May 6-10, Carlsbad, New Mexico: NCKRI Symposium 2. Carlsbad (NM). National Cave and Karst Research Institute, p. 449-458

Edmundson RS, Nunan WE. 1973. Geology of the Berryville, Stephenson and Boyce Quadrangles, Virginia. Virginia Division of Mineral Resources Report of Investigations 34, Charlottesville, Virginia. 112 pp., 3 plates, 1:24,000 scale.

ESRI. 2012. ArcGIS Help 10.1 – Zonal Fill (Spatial Analyst). Available online at http://resources.arcgis.com/en/help/main/10.1/index.html#/Zonal_Fill/009z000000w3000000/

Jackson S. 2013. Optimized Pit Removal V1.5.1 Tutorial. Center for Research in Water Resources University of Texas at Austin. Available online at <http://tools.crrwr.utexas.edu/OptimizedPitRemoval/CRWR%20Tools%20Optimized%20Pit%20Removal.html> (accessed March 16, 2015).

Lindsay JB, Creed IF. 2006. Distinguishing actual and artefact depressions in digital elevation data. *Computers & Geosciences* 32: 1192–1204.

Maidment DR. 2002. Arc Hydro: GIS for water resources. Esri Press.

Mitasova H, Mitas L, Brown WM, & Johnston DM. 1999. Terrain modeling and soil erosion simulations for Fort Hood and Fort Polk test areas. Geographic Modeling and Systems Laboratory, University of Illinois at Urbana-Champaign.

Poppenga SK, Worstell BB, Stoker JM, Greenlee SK. 2010. Using selective drainage methods to extract

- continuous surface flow from 1-meter lidar-derived digital elevation data. U.S. Geological Survey Scientific Investigations Report 2010–5059, 12 p.
- Tarboton DG. 2012. Terrain analysis using digital elevation models (TauDEM). Logan, UT. Available online at <http://hydrology.uwrl.usu.edu/taudem/taudem5.0/index.html> (accessed March 16, 2015).
- Wall J, Bohnenstiehl DR. 2014. Power-law relationship of sinkholes and depressions within karst geology 63rd Annual Meeting Southeastern Section of the Geological Society of America, Blacksburg, Virginia, 10-11 April.
- Zandbergen PA. 2010. Accuracy considerations in the analysis of depressions in medium-resolution Lidar DEMs. *GIScience & Remote Sensing* 47 (2): 187–207.

CHAPTER 2

Morphometric comparisons between automated and manual karst depression inventories in Apalachicola National Forest, Florida, and Mammoth Cave National Park, Kentucky, USA

Chapter 2 was published in the October 2017 volume of *Natural Hazards* with the following co-authors:

Bohnenstiehl, D. R.¹; Wegmann, K.W.¹; Levine, N. S.²

¹ Department of Marine, Earth, and Atmospheric Sciences, NC State University, Raleigh, North Carolina, USA

² Department of Geology and Environmental Geosciences, College of Charleston, Charleston, South Carolina, USA

Morphometric comparisons between automated and manual karst depression inventories in Apalachicola National Forest, Florida, and Mammoth Cave National Park, Kentucky, USA

John Wall¹  · DelWayne R. Bohnenstiehl¹ · Karl W. Wegmann¹ · Norman S. Levine²

Received: 19 April 2016 / Accepted: 22 September 2016 / Published online: 3 October 2016
© Springer Science+Business Media Dordrecht 2016

Abstract Karst depression catalogs are critical to assessing the hydrology and geohazards of an area; yet, the delineation of these features within a landscape can be a difficult, time-consuming and subjective task. This study evaluates the efficacy of karst depression inventorying using an automated fill-difference method operating on high-resolution lidar-derived digital elevation models (DEMs). The resulting catalog is compared with existing karst depression inventories for two low-development areas of the USA, Mammoth Cave National Park (MACA) and Apalachicola National Forest (ANF), where karst depressions have been mapped previously using a manual closed-contour approach. The automated fill method captures 93 and 85 % of these previously mapped karst depressions at MACA and ANF, respectively. Field observations and topographic analysis suggest that the omitted features were likely misclassified within the existing catalogs. The automated routine returns 797 and 3377 additional topographic depressions, at MACA and ANF, respectively, which are not included in the existing catalogs. While the geology of ANF is mostly homogenous Quaternary deposits, the newly identified, typically smaller-scale depressions found within MACA tend to be disproportionately located in non-carbonate-dominated formations, where the development of karst may be restricted by geologic heterogeneity. Within both areas, the size distributions of the two inventories are statistically identical for features larger than $\sim 10^3$ m² in area or ~ 3 m in depth. For individual depressions captured by both methods at MACA, the automated fill-difference routine tends to return a slightly larger estimate of depression size and aggregate small depressions into larger ones. Conversely, at ANF, some low-relief depressions may be disaggregated by the fill-difference technique, with a trend toward smaller estimated depression areas when the automated method is employed. The automated fill-difference method, operating on high-

✉ John Wall
jwall@ncsu.edu

¹ Department of Marine, Earth and Atmospheric Sciences, North Carolina State University, 2800 Faucette Drive, Room 1125 Jordan Hall Campus, Box 8208, Raleigh, NC, USA

² Department of Geology and Environmental Geosciences, College of Charleston, 66 George Street, Charleston, SC, USA

resolution lidar-derived DEMs, can reproduce and expand the existing inventories of karst depressions, while minimizing false detections that may be inherent within pre-existing catalogs.

Keywords GIS · Lidar · Topography · Sinkhole

1 Introduction

Closed depressions are topographic features having no lateral surface flow or external drainage. In karst landscapes, closed depressions are associated primarily with sinkholes, sinking streams, and cave openings, which form by collapse or subsidence following the chemical dissolution of carbonate or evaporate rocks. Geologic units susceptible to karst development cover roughly 25 % of the continents (Veni et al. 2001), and these areas are home to a similar percentage of global population (Ford and Williams 2013). Within the contiguous United States, nearly 20 % of the landscape is underlain by karst-susceptible geologic units (Weary and Doctor 2014) (Fig. 1).

Inventorying karst depressions provides a cost-effective strategy for assessing and mitigating collapse hazards (e.g., Galve et al. 2009, 2011). As development encroaches into regions prone to sinkhole collapse, losses due to catastrophic collapse, as well as foundation and structural repairs, are on the rise. For example, it is estimated that the state of Kentucky loses roughly \$23 million per year to sinkhole and related karst hazards (Dinger et al. 2007), while a recent report to the Florida State Senate notes that citizens incurred over \$84 million in sinkhole-related damages in 2009 alone (Florida State Senate 2011).

Many karst depressions store rainwater and are often physically linked to aquifers capable of holding large volumes of groundwater. These depressions also provide pathways for chemical pollutants that migrate from the atmosphere and surface waters into the subsurface (e.g., Sanderson et al. 1995; Kerr-Upal et al. 1999; Stotler et al. 2011). Since groundwater serves as the primary municipal water source in many karst-prone areas (Green et al. 2006), the high degree of hydrologic connectivity poses a potential hazard to human health. Hazard analyses in karstic regions often require that sites of aquifer recharge (i.e., karst depressions) are considered in urban and industrial planning efforts and existing karst inventories be integrated as part of the risk assessment for any facility storing or producing hazardous materials.

Beyond their importance for geohazard and environmental risk assessment, inventories of karst depressions have wide applicability. Because of distinct hydrology and soils, karst depressions can represent important ecological and biogeochemical niches, hosting a number of regionally rare species (e.g., Hérault and Thoen 2008; Etienne et al. 2013) and providing a potential refuge for some species as wetland areas continue to be destroyed around the globe. Moreover, as predominantly depositional settings, karst depressions may preserve a rich history of paleoenvironmental and paleontological data (e.g., Shunk et al. 2006; Etienne et al. 2013). They can also be important sources of archaeological information, hosting cultural artifacts associated with prior human utilization of these features as water resources, repositories for rubbish, or even burial sites. The identification of karst features is increasingly recognized as a key input for archaeological predictive modeling and prospection studies (e.g., Mayer 2002; Bement 2010).

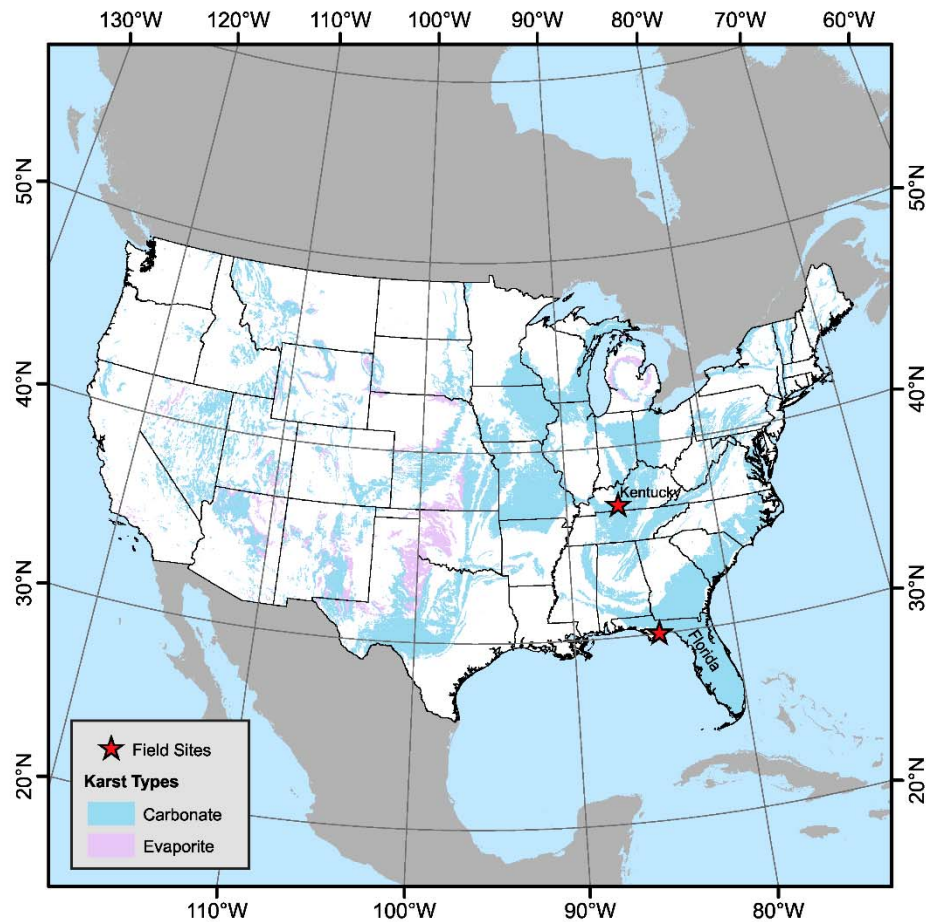


Fig. 1 Karst-susceptible regions of the contiguous United States. The Mammoth Cave National Park, Kentucky, and Apalachicola National Forest, Florida, field sites are indicated by stars (Weary and Doctor 2014)

The goal of this study is to compare karst depression inventories created using an automated fill-difference routine (e.g., Doctor and Young 2013) with existing inventories that have been derived primarily through the manual identification of closed-contour polygons on 7.5-min topographic maps (1:24,000 scale). The latter approach is widely used by federal, state and local agencies in the USA. For this investigation, Mammoth Cave National Park (MACA), Kentucky, and Apalachicola National Forest (ANF), Florida, were chosen due to their dense forest cover and low-degree of development. Low-development locations were chosen to limit the number of anthropogenic depression structures such as retention ponds, which would have to be excluded, either manually or through hydrologic reconditioning of the elevation model (e.g., Wall et al. 2015). The two inventories are compared based on the size ratio of spatial co-location of features and their respective area and depth distributions. Field investigations were carried out to understand some of the discrepancies observed between the two inventorying techniques.

2 Background

2.1 Formation of karst depressions

Karst topography forms as a result of physical and chemical weathering processes typically involving dissolution along fracture and bedding planes. Dissolution is most often driven by the presence of carbonic acid (HCO_3) that is created as rainwater reacts with and passes through CO_2 in the atmosphere and soil (Han and Liu 2004). Less frequently, however, sulfuric acid (H_2SO_4) can cause dissolution as oxygen-rich surface waters react with sulfide minerals (Engel et al. 2004). Overtime, dissolution creates void space in the rock mass by widening fractures, ultimately leading to the alteration of the groundwater hydrologic regime.

When the mantle of rock and soil above a void moves downward through collapse, sagging or suffusion processes, a depression is formed at the Earth's surface (Gupta 2011). Although catastrophic collapse events tend to be the most dramatic and pose the greatest direct threat of damage and injury, sagging and suffusion occurs with greater frequency and are often implicated in structural damage to buildings (Gutiérrez et al. 2008). Once formed, karst depressions may enlarge through time or link together to form compound sinks or uvalas. The development and growth of karst depressions may be accelerated by anthropogenic or natural activities that load the covering material, or by a lowering of the water table that reduces supportive buoyant forces (Tharp 1999).

2.2 Inventorying karst depressions

Government agencies are often tasked with generating inventories of karst depressions for hazard assessment and land-use planning. Although these catalogs may incorporate field and aerial photographic observations, at the state-wide level within the USA they have been generated primarily by the manual delineation of closed depression contours on topographic maps (e.g., Paylor et al. 2003; Arthur et al. 2005). Such efforts have traditionally used the photogrammetrically derived 7.5-min quadrangle maps (1:24,000-scale) that are produced by the United States Geological Survey (USGS) with typical contour intervals between 5 and 40 ft (1.5–12.2 m). The completeness and accuracy of these karst inventories are therefore directly dependent on the resolution and accuracy of the underlying topographic maps (Day 1976; Garbrecht and Starks 1995), which may suffer from photogrammetric artifacts at the time of creation that are associated with poor image contrast, scene boundary effects, and tree canopy cover (e.g., Gao 1995; Hodgson et al. 2003).

Recently, the application of light detection and ranging (lidar) topographic data to various geomorphic sub-disciplines has aided the identification of small-scale features including karst depressions. There are several methods for karst depression delineation using lidar data, including: outermost closed-contour identification (Rahimi and Alexander 2013); watershed-based karst depression delineation (Jenson and Domingue 1988); and the fill-difference technique (Doctor and Young 2013; Zhu et al. 2014; Kobal et al. 2015). The outermost closed-contour method is synonymous with the current method employed for manual inventories using 1:24,000-scale topographic maps, but updated to use higher-resolution topographic data. The watershed-based method determines contributing flow to a karst depression and tends to be used in hydrologic studies. The fill-difference method

was identified by Bauer (2015) as being the best at parameterizing the karst geomorphology of a region and is discussed in detail below.

2.3 High-resolution topographic data from lidar

Airborne lidar data can be employed to accurately portray topography beneath the cover of vegetation and at a high spatial resolution. Lidar instruments typically emit a pulse within the 900–1550 nm (infrared) range (Crutchley and Crow 2010). This being said, in areas of dense vegetation cover, particularly those areas with shrub and scrub layers, the number of laser pulses which reach the ground is likely to be restricted or result in false ground returns, thus confounding topographic analyses. A second method of lidar data collection, a full-waveform laser pulse, as opposed to discrete returns, can be recorded and post-processed using algorithms that are intended to remove false ground returns leading to greater hypsographic accuracy (Doneus et al. 2008).

Lidar data resolution is variable and is dependent on aircraft speed and altitude as well as the number of emitted laser pulses per second. Lidar data collection contracts usually specify a point density that is guided by a specific application; however, point spacing of one meter or less is not uncommon with sub-meter point spacing becoming increasingly common for engineering applications (Slatton et al. 2007; Carter et al. 2012). By comparison, elevation data derived from 1:24,000-scale topographic quadrangles typically have a point spacing of either 30 m (pre-1990s) or 10 m (post-1990s). Thus, lidar represents a 5- to 15-fold improvement over existing topographic data used to delineate karst depressions.

3 Study areas

Mammoth Cave National Park (MACA) spans roughly 295 km² and is located within the Pennyroyal–Mississippian Plateau physiographic province of central Kentucky (Fig. 2a). The west flowing Green River bisects the park. Topography in the north half is dominated by fluvial processes and landforms, whereas karst processes and landforms dominate the southern half. The surface morphology north and south of the Green River is a reflection of variations in bedrock geology. Mississippian sandstones underlie the northern half of MACA, while the southern portion is dominated by Mississippian carbonates in addition to sandstones and shales. The bedrock geology of the region is detailed elsewhere (White et al. 1970; Palmer 1981; Thornberry-Ehrlich 2011). Speleogenesis of Mammoth Cave was investigated by Granger et al. (2001) using ²⁶Al/¹⁰Be cosmogenic radionuclide burial dating methods on sediments transported into the Mammoth Cave system from external streams. Formation of the cave system is estimated at ca. 3.5 Ma when the Green River incised into the Girkin limestone formation. Between 3.5 Ma and the late Pleistocene, intervals of continental ice advance in the upper Ohio River basin resulted in alternating phases of stream incision and water table lowering interrupted by periods of increased regional water table elevations associated with episodes of sediment aggradation along the Green River. Both the incision and aggradation phases were important for the widening and deepening of the Mammoth Cave network. Net late Pliocene through Quaternary incision of the Green River resulted in lowering of the regional water table and speleogenesis of Mammoth Cave via the downward movement of slightly acidic surface waters through the host carbonate bedrock.

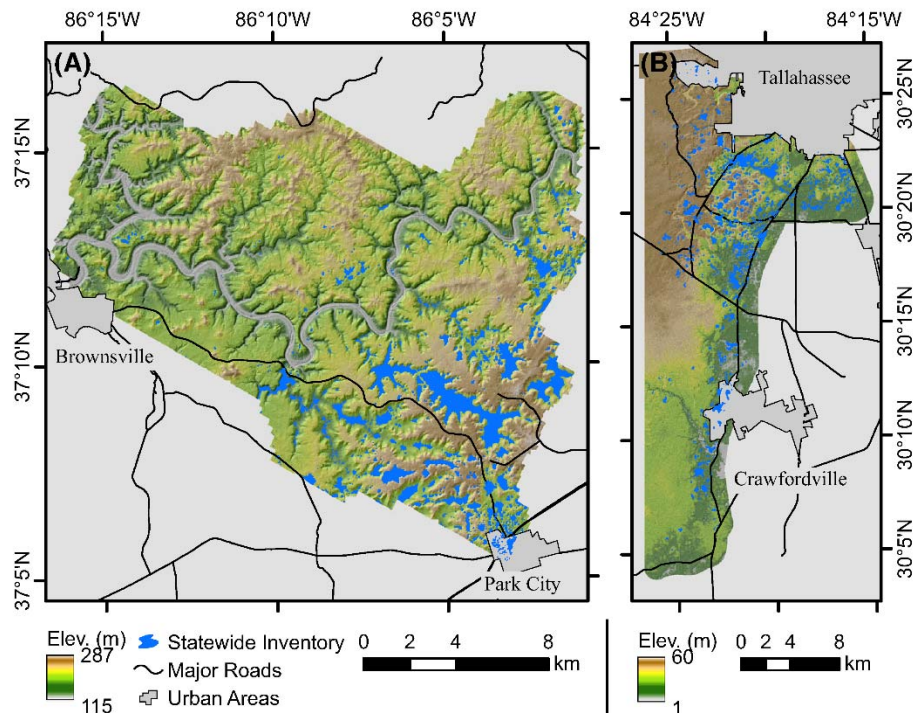


Fig. 2 Hillshaded digital elevation models of **a** Mammoth Cave National Park and **b** Apalachicola National Forest created from light detection and ranging (lidar) data. State-wide inventoried karst depressions, major roads, and urban areas are indicated

Apalachicola National Forest (ANF) spans several counties in northwestern Florida and covers an area of 2572 km². This study focuses upon a 300-km² area in the eastern edge of the National Forest, where karst depressions are prevalent (Fig. 2b). The study area crosses three physiographic province boundaries: the Tallahassee Hills in the north, the Gulf Coast Lowlands to the southwest, and the Woodville Karst Plain in the southeast. The southeast flowing Ochlockonee River bisects the Forest. Each half of the Forest contains smaller meandering rivers and creeks. Bays, ponds, and swamps dot the landscape with a greater presence in the eastern half. The Cody Escarpment is the only major topographic feature. Puri and Vernon (1964) attribute the development of the Escarpment to Pliocene and Pleistocene sea level highstands, while fluvial and karst processes altered the surface expression (Upchurch 2007). Karst topography within this area likely initiated during the lowstands of the Pleistocene (Olsen 1958). The geology of the area is dominated by Pleistocene to Holocene surficial deposits of undifferentiated sediments consisting of silicates, organics, and freshwater carbonates (Scott 2001). Subsurface geology consists mostly of the Miocene Torreya Formation, Hawthorne Group, and the St. Marks Formation, which were deposited during sea level transgressions.

Both study areas are covered by dense vegetation (Fig. 3). MACA and ANF have an average canopy cover of 79 and 67 %, respectively (Homer et al. 2015). Vegetation at both areas is managed differently by their respective overseeing agencies. At MACA, the National Park Service maintains natural woodlands where controlled burns are sparse in terms of space and time. Conversely, at ANF, the National Forest Service utilizes a

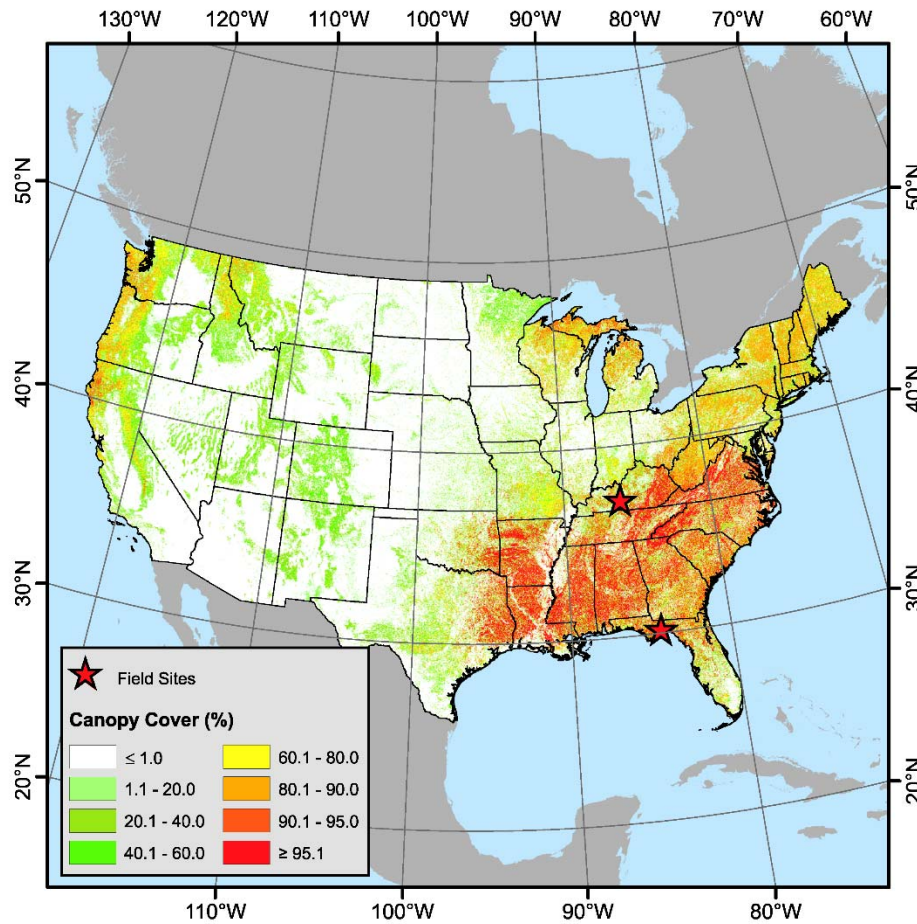


Fig. 3 Percent canopy cover for the contiguous United States (Homer et al. 2015). Note the change in scale between 90 and 100 %, used to highlight the most dense canopy cover. Field sites are indicated by stars

controlled burning regime to manage understory vegetation. Thus, the presence of an underlying shrub and scrub layer at MACA presents problems for topographic analysis. Surrounding land-use outside of the no-development Park and Forest is likely to impact inventorying efforts and should be taken into account when inventorying karst depressions (Seale et al. 2008). At MACA, the park is surrounded by some areas that are similarly forested to the Park, while other areas are cultivated. At ANF, dispersed single-family homes abut the Forest boundary.

4 Data

Geologists employed by the states of Kentucky and Florida have generated comprehensive state-wide karst depression inventories that are derived primarily through the manual digitizing of outer most closed-contours from 7.5-min topographic quadrangle maps (Florea et al. 2002; Paylor et al. 2003; Arthur et al. 2005). In both of these state inventories

individual karst depressions are represented as closed polygons, allowing size and shape metrics to be derived from individual features. Portions of these state databases spanning MACA and ANF are used for comparison with the results of an automated fill-difference routine applied using a high-resolution DEM produced from recent lidar surveys sponsored by the Joint Fire Science Program and the Northwest Florida Water Management District, respectively. Full-wave lidar data from MACA were initially collected in 2011 by the Joint Fire Science Program of the US Department of the Interior and National Forest Service of the US Department of Agriculture during leaf-on conditions. A contractor with the National Forest Service then processed the waveforms into discrete multiple returns using the *Toolbox for LiDAR Data Filtering & Forest Studies* (Chen 2007). Ground returns throughout the Park have an average density of 2.37 points per m² and were converted to a 1-m² raster grid format using the ArcGIS 10.1 *LAS Dataset to Raster tool*.

Airborne lidar data from ANF were collected in 2009 during leaf-off conditions. The processed data were originally released as a 1-m² spatial resolution DEM generated using a Triangulated Irregular Network. However, due to the low density of ground points (~0.75 points per m²), the DEM was later resampled to 2 m² raster grid using a cubic convolution routine.

5 Methods

5.1 Automated inventorying using a fill-difference routine

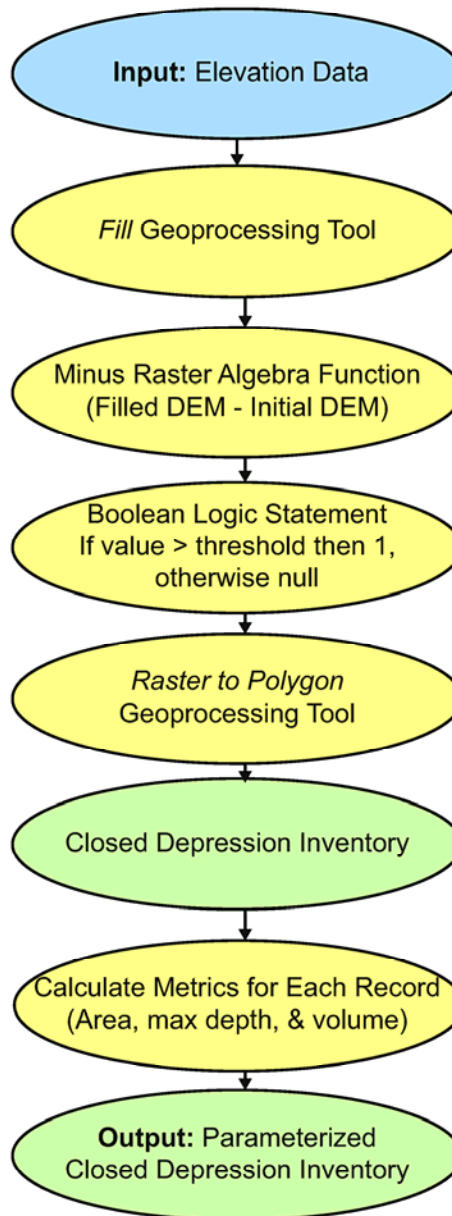
The delineation of closed depressions within a geographic information system is a relatively straightforward process (Fig. 4). ArcGIS *Hydrology Toolbox* and *Raster Algebra* were employed to delineate and parameterize karst depressions. An initial DEM was hydrologically corrected using the *Fill tool*. This tool is usually employed to ensure stream delineation flows over small errors in the elevation data. However, in karst topography, closed depressions are likely to be real features within the landscape (Lindsay and Creed 2006; Zandbergen 2010), allowing this tool to be used for identification (e.g., Doctor and Young 2013). The filled DEM was differenced from the original DEM to obtain a depth raster, from which any feature more than nine pixels in size was converted to a polygon using Boolean logic.

To account for the finite resolution of the lidar data, features having a maximum depth of less than 0.73 m were also excluded from the catalog. This depth threshold corresponds to two standard deviations of the vertical accuracy within the coarser ANF elevation model (NWFWMMD 2015). Finally, features with area less than the minimum reported in each state inventory were also excluded, unless they were spatially co-located with a depression cataloged by the State. For MACA, this area threshold was 119 m², while at ANF it was 40 m². After these restrictions were applied, the automated fill-difference method returned catalogs of 1504 and 4454 karst depressions at MACA and ANF, respectively.

5.2 Testing the impact of data resolution

As noted previously, DEM quality and resolution, topographic relief, vegetation, and land-use can impact the success rate of the automated fill-difference method. Quantifying the relative impact of these natural variables is complicated by the fact that they may co-vary at different scales within these landscapes. It is therefore difficult to determine which is

Fig. 4 Workflow used in this study for karst depression inventorying and parameterization within a geographic information system



most impactful in a statistically rigorous way. Of these variables, the influence of data resolution can be simulated by down-sampling (i.e., re-gridding) the higher-resolution (1 m^2) MACA data and repeating the cataloging method. Resampling was carried out in ArcMap using the *Resampling* tool with a cubic convolution method. As with the initial catalog, thresholds were enforced using the smallest area present within the state catalog (119 m^2).

5.3 Comparisons with existing state inventories

The spatial co-location of depressions, including one-to-one and one-to-many relationships, was obtained between the automated fill-difference and existing state inventories. These relationships can provide insight into size and aggregation versus disaggregation biases within the catalogs.

A logarithmic size ratio (ϕ) was used to identify potential bias in the size of depressions estimated using the automatic fill-difference method, relative to the state inventories. For each depression with a one-to-one relationship between catalogs, the parameter is defined as \log_{10} of the size (area or depth) ratio between the state and automatic fill catalogs.

For depressed features with one-to-many relationships, the size ratio is calculated as a summation:

$$\phi = \log_{10} \left(\frac{S_{\text{state}}}{\sum S_{\text{fill}} \subseteq S_{\text{state}}} \right) \quad (1a)$$

when many depressions in the automated fill catalog intersect (\subseteq) with one feature in the state catalog, or:

$$\phi = \log_{10} \left(\frac{\sum S_{\text{state}} \subseteq S_{\text{fill}}}{S_{\text{fill}}} \right) \quad (1b)$$

when many depressions in the state catalog intersect with one feature in the fill-difference catalog. A feature's size (S) is represented either by its area or maximum depth estimated from the lidar-derived DEM. Therefore, a negative size ratio will exist when the automated fill-difference method returns a larger size or depth than the state inventory for a given depression.

The size distribution of depressions is also characterized by comparing the empirical cumulative distribution functions (CDFs) for each inventory (Fig. 5). The null hypothesis states that, for features larger than some cutoff size, the automated fill catalog and state inventory exhibit the same distribution of depressed areas and depths. The cutoff size is defined to be the largest size depression for which the null hypothesis cannot be rejected with 95 % confidence. This is determined iteratively by applying a series of size thresholds to the two catalogs and assessing their relative goodness-of-fit using a nonparametric Kolmogorov–Smirnov (K–S) test.

5.4 Catalog validation

Karst depressions that were automatically identified using the fill routine, but not present in the existing state inventories, were highlighted for additional investigation. In order to prioritize sites to ground-truth, maps of each newly identified karst depression were created using aerial photographs obtained from ESRI base maps and a slope-shaded DEM derived from the lidar data. Based upon analysis of these maps, depressions were categorized as (1) 'likely,' (2) 'possible' or (3) 'unlikely' to be karst features. Depressions in the 'likely' category were identifiable in both the topographic data aerial imagery, with no indication of anthropogenic influence on the landscape. A newly identified depression was placed into the 'possible' category, if the natural or anthropogenic genesis of this feature was not clearly discernable using the remotely sensed data. Such an example would include a topographic low that has one side defined by a berm of possible anthropogenic origin. The

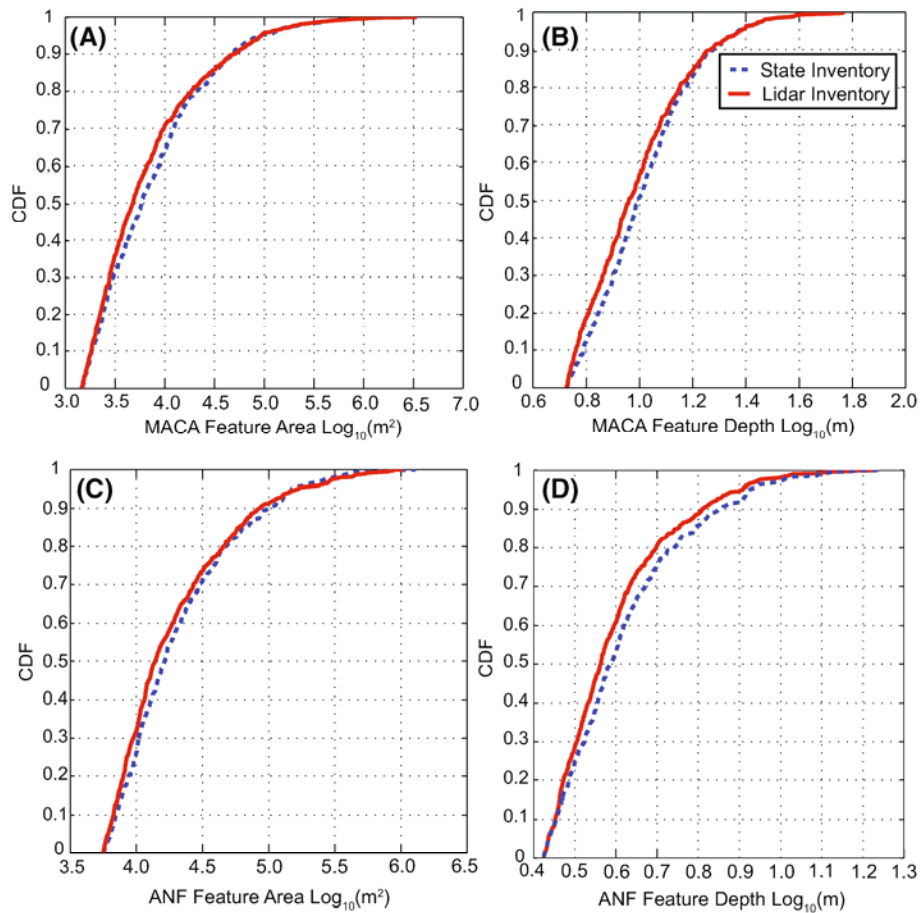


Fig. 5 Cumulative distribution functions (CDFs) for the state-wide (blue) and Lidar inventories for area and depth parameters at Mammoth Cave National Park (a, b) and Apalachicola National Forest (c, d). At Mammoth Cave National Park, the empirical distribution of features with areas $>1456 \text{ m}^2$ and depths $>5.3 \text{ m}$ are statistically identical between the two catalogs. At Apalachicola National Forest, the empirical distribution of features with areas $>5620 \text{ m}^2$ and depths >2.64 is statistically identical between the two catalogs

‘unlikely’ category included features that appeared to be man-made reservoirs, or the result of artifacts in the DEM.

Field investigations were carried out to validate the classification of the newly identified depressions and determine why some ‘likely’ features were missed within existing state catalogs. Features within each of the three categories were exported to KML files, which were loaded into the Backcountry Navigator Pro software on a 2013 Nexus 7 tablet. This allowed their polygonal outlines to be overlain on USGS topographic base maps, US Forest Service topographic maps, and aerial photographs. The tablet’s on-board GPS (3-6 m accuracy) was used to navigate to a subset of the features. Field notes and photographs were shared with collaborators in near-real time.

6 Results and discussion

6.1 Catalog comparisons

State inventories of karst depressions at MACA and ANF contained 820 and 822 records, respectively. Using the automated method, 1504 and 4454 karst depressions were found at MACA and ANF. The distribution of resulting inventories is depicted in Fig. 6 and quartiles reported in Table 1. The minimum depth within the state inventories at MACA and ANF is both zero indicating that some features inventoried by the state were either flat or represent topographic highs within the lidar-derived DEM.

At MACA, 93 % ($n = 764$) of the depressions cataloged in the state inventory spatially overlapped within the automatic fill catalog. The remaining 56 karst depressions identified by the state were not identified through the automated method. Of these, 51 (92 %) were represented in the lidar-derived DEM dataset by features too small to be retained as

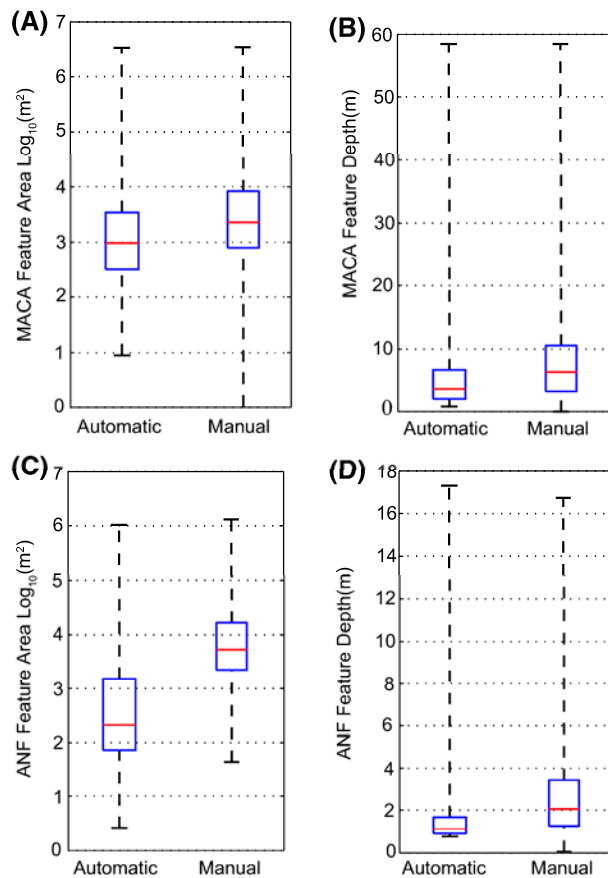


Fig. 6 Boxplots depicting quartiles for the distribution of areas and maximum depths of manually and automatically generated karst depression catalogs at Mammoth Cave National Park (a, b) and Apalachicola National Forest (c, d). Maximum depths for manually generated karst depressions were derived from the processed lidar-derived digital elevation models

Table 1 Area and maximum depth quartiles for manually and automatically generated karst depression catalogs at Mammoth Cave National Park (MACA) and Apalachicola National Forest (ANF)

	Mammoth Cave Nat'l Park		Apalachicola Nat'l Forest	
	Manual	Automatic	Manual	Automatic
Area (m ²)				
Q0	0.8	9.0	40.6	36
Q1	778.6	314.5	2109.8	72.0
Q2	2265.6	967.5	5081.8	208.0
Q3	8216.3	3489.5	15,803.3	1518.0
Q4	3,519,556.4	3,427,380.0	1,296,131.5	1,038,684.0
Maximum depth (m)				
Q0	0.0	0.8	0.0	0.8
Q1	3.2	2.0	1.2	0.9
Q2	6.3	3.6	2.1	1.1
Q3	10.6	6.6	3.5	1.7
Q4	58.5	58.5	17.3	17.3

significant. Five additional depressions (8 %) were omitted due to edge effects, which prevented the fill routine from functioning near the boundaries of the lidar-derived DEM.

At ANF, 85 % ($n = 753$) of the depressions cataloged in the state inventory spatially overlapped with those within the automatic fill catalog. Of the state-inventoried karst depressions not returned using the automated method, only one omitted feature can be attributed to edge effects. The remaining 128 are not associated with a resolvable topographic feature within the lidar-derived DEM for ANF.

Given that the USGS topographic quadrangles are contoured at 5-ft (1.5 m) intervals in ANF and 20-ft (6.0 m) intervals in MACA, and the vertical accuracy of the lidar data is ~ 0.37 m, the state inventory should not contain features at a finer scale than identifiable from the lidar-derived DEM. Depressed features within the existing state catalogs, but not returned by the automated fill-difference routine, are therefore suspected to reflect errors of commission in the existing database. These might arise due to (1) inaccuracies in the topographic quadrangles, reflecting the challenges associated with photogrammetric mapping in forested environments (e.g., Fig. 7), or (2) human error during the digitization of the closed-contours from topographic base maps.

Several depressions missed by the automated method, but classified by the manual inventory, were investigated in the field to validate this interpretation. In all instances, there was no evidence for the karst depression observed in the field; however, all of these features were in areas of dense or changing canopy cover, which may have led to their erroneous interpretation as topographic low during photogrammetric processing (e.g., Bolstad and Stowe 1994; Gong et al. 2000).

6.2 Distribution of depressions

At MACA, 633 unique relationships were identified between the catalogs, while 685 were identified at ANF. Of these unique relationships, one-to-one accounted for 531 (84 %) at MACA and 502 (73 %) at ANF. While the majority of the relationships are one-to-one, one-to-many relationships indicate aggregation or disaggregation at these locations. Thus, 102 (16 %) one-to-many relationships were identified at MACA and 183 (27 %) at ANF. The most extreme instances are illustrated by a 1-to-35 (automated to manual) relationship

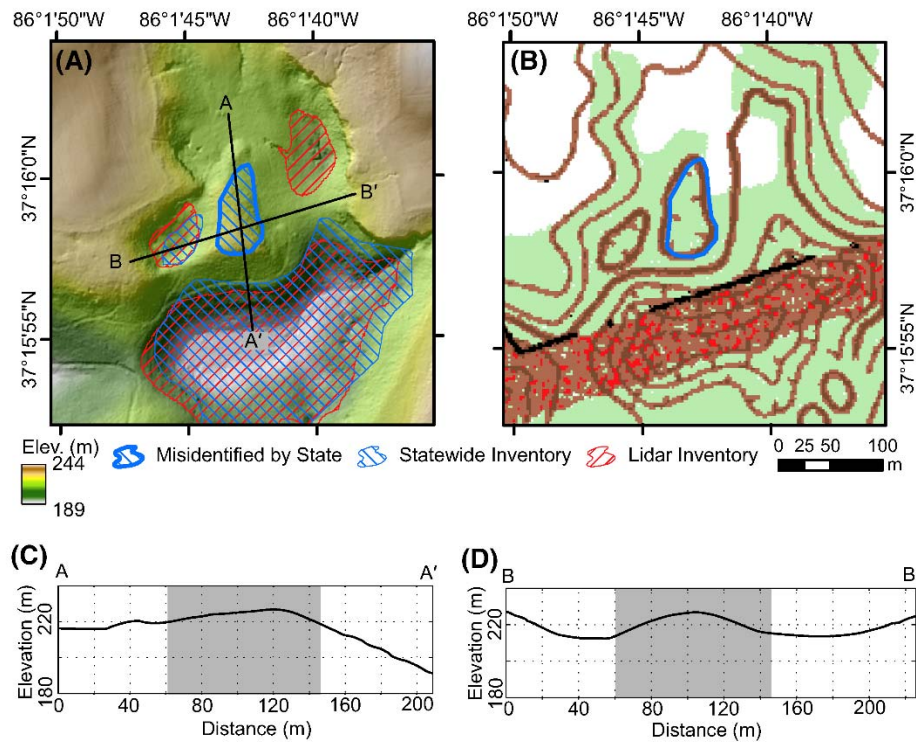


Fig. 7 Example of a false-positive karst depression included in the state-wide Inventory of Kentucky. **a** Map-view of the lidar data with the misidentified karst depression in association with other manually and automatically identified karst depressions. **b** These lidar data are compared to the USGS 1:24,000-scale (20 ft. contour interval) Cub Run topographic quadrangle showing how the hill was represented as a closed depression on the quadrangle. **(c, d)** Topographic profiles illustrating that the false-positive karst feature is indeed a topographic high, as indicated by the *gray shading*. This false positive was not detected by the automated method and should not be included in an inventory of karst depressions

at MACA and 75-to-1 relationship at ANF (Fig. 8). This suggests that at the MACA field site in Kentucky the automated method aggregates karst depressions, whereas the manual method used by the state-wide inventories disaggregates relative to the automated method. Conversely, at the ANF study site in northern Florida, the automated method disaggregates karst depressions, likely reflecting the presence of lower-relief depressions and somewhat lower-quality lidar data within ANF.

At MACA the automated fill-difference method tends to return a larger estimate of depression area and depth, compared to the existing state catalogs ($\phi < 0$); whereas at ANF, the areas returned by the automated method are smaller in terms of area ($\phi < 0$), with less bias in depth (Fig. 9). Recall that depth is extracted from the lidar-DEM for both catalogs.

The closed-contour delineation methods will underestimate the size (area and relief) of topographic features, with the magnitude of the bias being a function of the local gradient in topography and the contour interval chosen in the analysis (Bohnenstiehl et al. 2012). The coarser 20-ft contour interval available at MACA, compared to the 5-ft contours used at ANF, may therefore contribute to the differences in the size bias observed between MACA and ANF (Fig. 9).

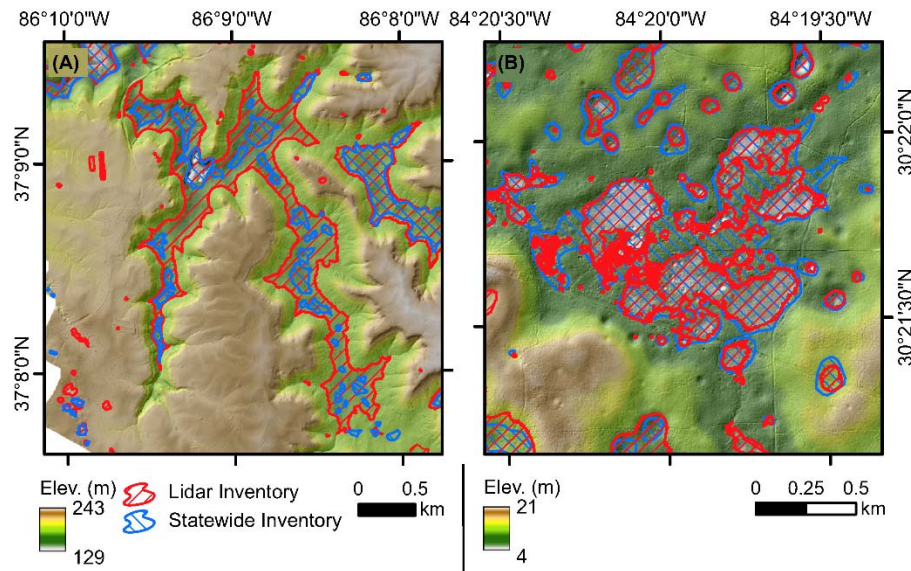


Fig. 8 Two most extreme one-to-many relationships at each location are shown. **a** At Mammoth Cave National Park, several smaller karst depressions are aggregated by the automated method. This feature is bounded in the northwestern corner by a raised road which restricts its estimated extent. While this is evident here, similarly bounded features are minimal-to-absent from the rest of the dataset. **b** Conversely, at Apalachicola National Forest, the most extreme one-to-many relationships are likely due to triangulation artifacts resulting from the data being gridded at too fine of a resolution given the ground point density

The size ratio (Eq. 1a, 1b), however, also incorporates the aggregation and disaggregation of features, which are influenced by the lidar data quality (point density) and local relief. For the higher-relief MACA area, where full-wave lidar data were processed to produce a more accurate bare earth model, there is a tendency for aggregation (Fig. 8). This is expected to result in both larger area and deeper depressions being reported. At ANF, where the overall relief is lower and the lidar data are slightly coarser resolution, there is a tendency toward disaggregation (Fig. 8). This produces smaller depressions in the automated inventory, relative to the state catalog.

The empirical size distributions returned by the manual and automated techniques are statistically identical for features larger than 1456 m² (38 × 38 m) and 5620 m² (75 × 75 m) at MACA and ANF, respectively. Given the factor of two differences in grid resolution between MACA and ANF, both thresholds represent a 38 × 38 pixel area. The empirical depth distribution is the same between state and automatic catalogs for features larger than 5.3 m at MACA and 2.6 at ANF. The differences are consistent with the greater relief within the MACA study area, compared to the ANF region.

6.3 Impact of data resolution

As data resolution is coarsened, the impact on the success rate of an automatically generated catalog varies little for the resolutions typically associated with airborne lidar and IFSAR datasets (Table 2). Consequently, the higher detection success rate observed at MACA, relative to ANF, is likely related to the improved data quality (hypsometric accuracy) of the DEM and larger topographic relief at MACA, as opposed to the slightly

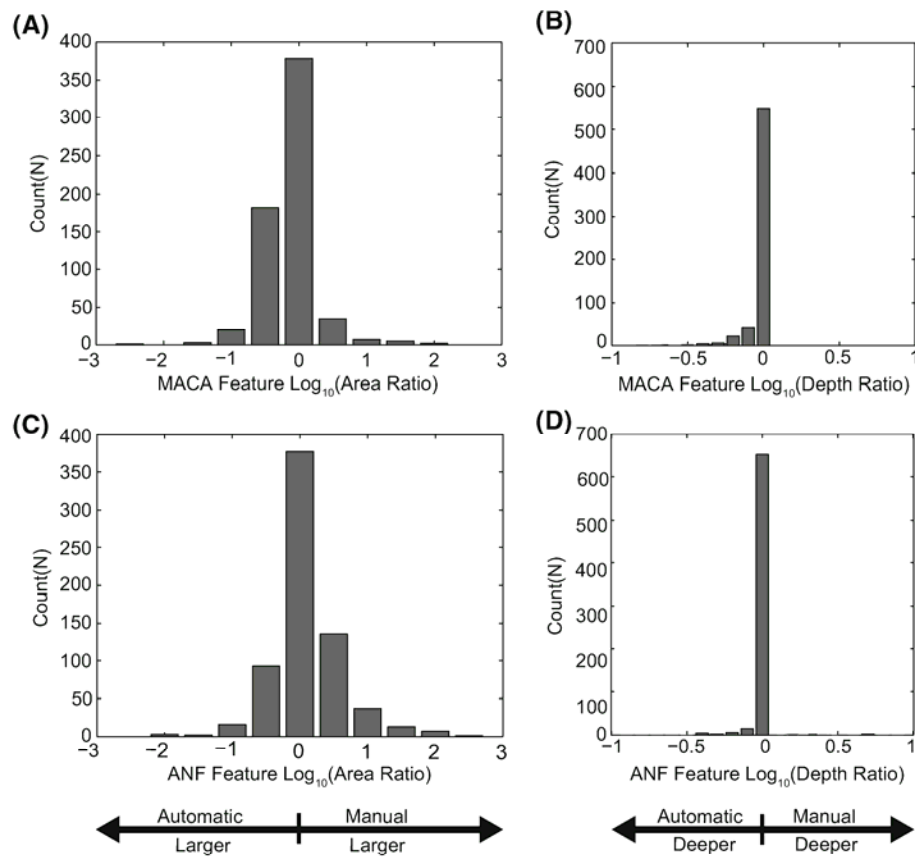


Fig. 9 Application of the Logarithmic Size Ratio to aid in identifying biases in recording metrics by the manual and automated karst depression cataloging methods for area and maximum depth at Mammoth Cave National Park (**a, b**) and Apalachicola National Forest (**c, d**)

Table 2 Success rates from re-gridding the MACA lidar-derived DEM and creating depression catalogs

Pixel dimension (m)	Resolution (m ²)	Success rate (%)	Catalog size (<i>n</i>)
1	1	93.2 % (<i>n</i> = 764)	1504
1.414	2	92.3 % (<i>n</i> = 757)	1472
3	9	92.2 % (<i>n</i> = 756)	1444
5	10	92 % (<i>n</i> = 754)	1410
10	100	90.7 % (<i>n</i> = 744)	1516
20	400	87.8 % (<i>n</i> = 720)	2296

higher (1 vs. 2 m²) pixel resolution of the MACA dataset. This being said, as pixel dimension increases the likelihood for errors of commission increases. Evidence of this can be seen with a pixel dimension of 20 m. The success rate for a catalog generated from a raster with this resolution is 87.8 %, but the catalog size is nearly 800 features larger than the original catalog. These newly created features are located primarily within the riparian zones and are the result of topographic aliasing.

6.4 Newly identified depressions

At MACA and ANF, 797 and 3377 new karst depressions were identified using the automated method. Laboratory classification of new karst depressions included three categories: ‘likely,’ ‘possible,’ and ‘unlikely.’ At MACA, 62 % ($n = 496$) were categorized as ‘likely,’ 20 % ($n = 153$) as ‘possible’ and 18 % ($n = 145$) as ‘unlikely.’ At ANF, 38 % ($n = 1283$) were categorized as likely, 45 % ($n = 1497$) as ‘possible’ and 17 % ($n = 580$) as ‘unlikely.’ The higher percentage of ‘likely’ features at MACA, relative to ANF, may reflect the relative quality of the lidar-derived DEMs, whereby an anthropogenic origin could be more confidently excluded in the MACA data. Of the 19 and 37 ‘likely’ depressions visited in the field at MACA and ANF, respectively, all were confirmed as true topographic depressions (e.g., Fig. 10).

While the lithology at ANF is nearly homogenous, the geologic formations observed at MACA can be classified as carbonate-dominated units, consisting mostly of limestone, with a lesser amount of shale, siltstone and sandstone (covering $\sim 143 \text{ km}^2$), and non-carbonate-dominated units consisting of sandstones and shales, with lesser amounts of limestone (covering $\sim 153 \text{ km}^2$). For depressions mapped within the state catalog, 84 % are found within carbonate units where they occupy $\sim 11 \%$ of the land area. Non-carbonate units contain only 16 % of the depressions and cover $\sim 0.45 \%$ of the land area. In contrast, when considering only the smaller-scale features added by the automated fill

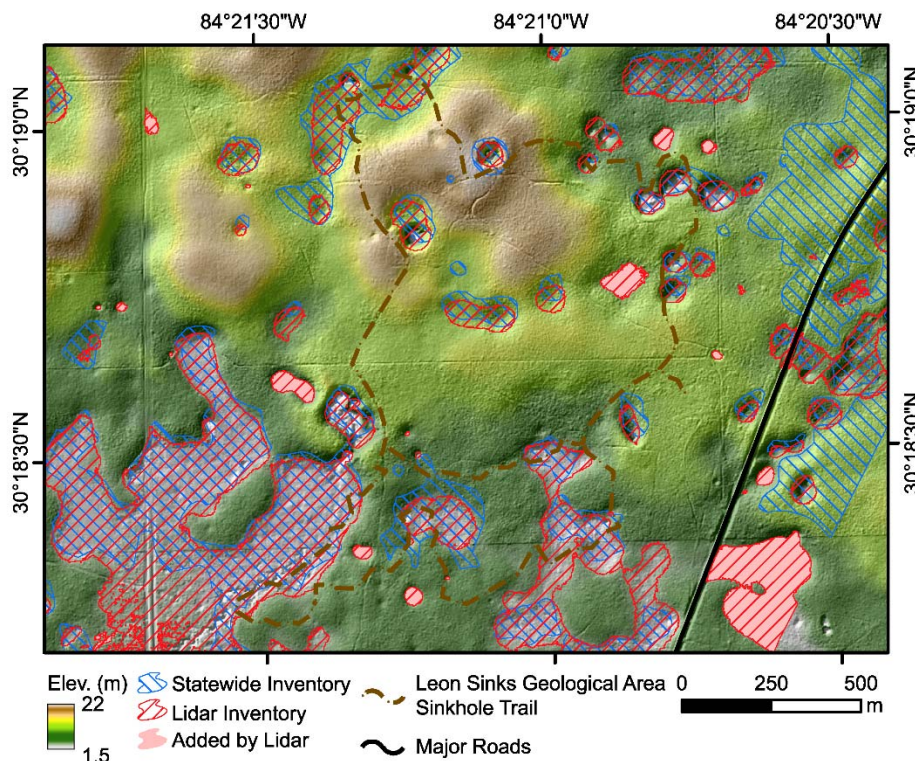


Fig. 10 Digital elevation model with a hillshade showing newly identified karst depressions at the Leon Sinks Geological Area within Apalachicola National Forest

technique, 47 and 53 % of the added depressions are observed in carbonate- and non-carbonate-dominated units, respectively, with both covering ~ 0.3 % of the land area. The recovery of a higher proportion of additional depressions in the non-carbonate-dominated areas, relative to the state catalog, may reflect the fact that the formation of smaller depressions (which would otherwise be missed by manual analysis using coarse resolution maps) is favored in areas where karst-prone lithologies are distributed more heterogeneously.

7 Conclusions

The automated fill-difference method is an effective tool for karst inventorying when compared to pre-existing manually generated inventories; the automated method is able to identify 95 and 87 % of manually identified karst depressions at MACA and ANF, respectively. The automated method additionally increases catalog size by 183 % ($n = 797$) at MACA and 505 % ($n = 3377$) at ANF, providing a more complete representation of these karst-dominated landscapes. The resulting distribution of depression sizes is statistically similar for features larger than $\sim 10^3$ m² in area and 3–5 m in depth. Depressions identified by the automated fill-difference method at MACA tended to be larger in area and depth, and more aggregated, than those identified by the manual method. However, at ANF, where the local relief and density of lidar returns used to construct the DEM are both lower, the automated method tends to disaggregate features.

The automated fill-difference method delineates the boundary of the depression based on the inability of water to be routed across the surface (resulting instead in the ponding of ‘virtual’ water in the GIS environment), eliminating subjective decision making and ensuring that the results are repeatable. The objective nature of the fill-difference method is ideal for characterizing the statistics of topographic depressions in any area for which lidar data exist, and could potentially be applied in the study of other geomorphic features (e.g., bays, sag ponds, kettles, and craters). With the expanding availability of lidar-derived topographic data that are being acquired in karst-susceptible portions regions of the world, the need to compare sinkhole susceptibility within these heterogeneous landscapes is important. The techniques developed herein are easily implemented within a GIS and can be used by planners and emergency managers to develop more accurate karst hazard maps.

Acknowledgments The authors would like to thank the National Speleological Society, the Cave Research Foundation, Environmental and Engineering Geology Division of the Geological Society of America, and the Southeastern Section of the Geological Society of America for funding this research. The authors would also like to thank the Hamilton Valley research station and Mammoth Cave National Park staff along with the Joint Fire Science Program and Northwestern Florida Water Management District for making their lidar data publicly available.

References

- Arthur JD, Baker AE, Cichon JR, Wood AR, Rudin A (2005) Florida aquifer vulnerability assessment (FAVA): contamination potential of Florida’s principal aquifer systems. Florida Geological Survey. http://waterinstitute.ufl.edu/suwannee-hydroobserv/pdf/FAVA_REPORT_MASTER_DOC_3-21-05.pdf
- Bauer C (2015) Analysis of dolines using multiple methods applied to airborne laser scanning data. *Geomorphology* 250:78–88. doi:10.1016/j.geomorph.2015.08.015
- Bement LC (2010) Hunter-gatherer mortuary practices during the Central Texas Archaic. University of Texas Press, Austin

- Bohnenstiehl DR, Howell JK, White SM, Hey RN (2012) A modified basal outlining algorithm for identifying topographic highs in gridded elevation data, part 2: application to Springerville Volcanic Field. *Comput Geosci* 49:308–314. doi:[10.1016/j.cageo.2012.04.023](https://doi.org/10.1016/j.cageo.2012.04.023)
- Bolstad PV, Stowe T (1994) An evaluation of DEM accuracy: elevation, slope, and aspect. *Photogramm Eng Remote Sens* 60:1327–1332
- Carter J, Schmid K, Waters K, Betzhold L, Hadley B, Mataosky R, Halleran J (2012) Lidar 101: An introduction to lidar technology, data, and applications. National Oceanic and Atmospheric Administration (NOAA) Coastal Services Center, Charleston
- Chen Q (2007) Airborne lidar data processing and information extraction. *Photogramm Eng Remote Sens* 73:109
- Crutchley S, Crow P (2010) The Light Fantastic: using airborne lidar in archaeological survey. *English Heritage, Swindon*
- Day M (1976) The morphology and hydrology of some Jamacian karst depressions. *Earth Surface Process* 1:111–129
- Dinger JS, Zourarakis DP, Currens JC (2007) Spectral enhancement and automated extraction of potential sinkhole features from NAIP imagery—initial investigations. *J Environ Inf* 10:22–29
- Doctor DH, Young JA (2013) An evaluation of automated GIS tools for delineating karst sinkholes and closed depressions from 1-meter LiDAR-derived digital elevation data. In: Land L, Doctor DH, Stephenson JB (eds) Sinkholes and the engineering and environmental impacts of Karst: proceedings of the thirteenth multidisciplinary conference, May 6–10, Carlsbad, New Mexico. NCKRI symposium 2. National Cave and Karst Research Institute, Carlsbad, NM, pp 449–458
- Doneus M, Briese C, Fera Janner M (2008) Archaeological prospection of forest areas using full-waveform airborne laser scanning. *J Archaeol Sci* 35:882–893. doi:[10.1016/j.jas.2007.06.013](https://doi.org/10.1016/j.jas.2007.06.013)
- Engel AS, Stern LA, Bennett PC (2004) Microbial contributions to cave formation: new insights into sulfuric acid speleogenesis. *Geology* 32:369–372. doi:[10.1130/G20288.1](https://doi.org/10.1130/G20288.1)
- Etienne D, Ruffaldi P, Dupouey JL, Georges-Leroy M, Ritz F, Dambrine E (2013) Searching for ancient forests: a 2000 year history of land use in northeastern French forests deduced from the pollen compositions of closed depressions. *Holocene* 23:678–691. doi:[10.1177/0959683612470173](https://doi.org/10.1177/0959683612470173)
- Florea LJ, Paylor RL, Simpson L, Gulley J (2002) Karst GIS advances in Kentucky. *J Cave Karst Stud* 64:58–62
- Florida State Senate (2011) Issues relating to sinkhole insurance. Interim Report 2011-104
- Ford D, Williams PD (2013) Karst hydrogeology and geomorphology. Wiley, Chichester
- Galve JP, Gutiérrez F, Remondo J, Lucha P, Cendrero A (2009) Evaluating and comparing methods of sinkhole susceptibility mapping in the Ebro Valley evaporate karst (NE Spain). *Geomorphology* 111:160–172. doi:[10.1016/j.geomorph.2009.04.017](https://doi.org/10.1016/j.geomorph.2009.04.017)
- Galve JP, Remondo J, Gutiérrez F (2011) Improving sinkhole hazard models incorporating magnitude–frequency relationships and nearest neighbor analysis. *Geomorphology* 134:157–170. doi:[10.1016/j.geomorph.2011.05.020](https://doi.org/10.1016/j.geomorph.2011.05.020)
- Gao J (1995) Comparison of sampling schemes in constructing DTMs from topographic maps. *ITC J* 1:18–22
- Garbrecht J, Starks P (1995) Note on the use of USGS level 1 7.5-minute DEM coverages for landscape drainage analyses. *Photogramm Eng Remote Sens* 61:519–522
- Gong J, Li Z, Zhu Q, Sui H, Zhou Y (2000) Effects of various factors on the accuracy of DEMs: an intensive experimental investigation. *Photogramm Eng Remote Sens* 66:1113–1117
- Granger DE, Fabel D, Palmer AN (2001) Pliocene-Pleistocene incision of the Green River, Kentucky, determined from radioactive decay of cosmogenic ^{26}Al and ^{10}Be in Mammoth Cave sediments. *Geol Soc Am Bull* 113:825–836
- Green RT, Painter SL, Sun A, Worthington SR (2006) Groundwater contamination in karst terranes. *Water Air Soil Pollut Focus* 6:157–170. doi:[10.1007/s11267-005-9004-3](https://doi.org/10.1007/s11267-005-9004-3)
- Gupta A (2011) Tropical geomorphology. Cambridge University Press, Cambridge
- Gutiérrez F, Guerrero J, Lucha P (2008) A genetic classification of sinkholes illustrated from evaporate paleokarst exposures in Spain. *Environ Geol* 53:993–1006. doi:[10.1007/s00254-007-0727-5](https://doi.org/10.1007/s00254-007-0727-5)
- Han G, Liu CQ (2004) Water geochemistry controlled by carbonate dissolution: a study of the river waters draining karst-dominated terrain, Guizhou Province, China. *Chem Geol* 204:1–21. doi:[10.1016/j.chemgeo.2003.09.009](https://doi.org/10.1016/j.chemgeo.2003.09.009)
- Hérault B, Thoen D (2008) Diversity of plant assemblages in isolated depressional wetlands from Central-Western Europe. *Biodivers Conservat* 17:2169–2183. doi:[10.1007/s10531-007-9227-x](https://doi.org/10.1007/s10531-007-9227-x)
- Hodgson ME, Jensen JR, Schmidt L, Schill S, Davis B (2003) An evaluation of LIDAR-and IFSAR-derived digital elevation models in leaf-on conditions with USGS Level 1 and Level 2 DEMs. *Remote Sens Environ* 84:295–308. doi:[10.1016/S0034-4257\(02\)00114-1](https://doi.org/10.1016/S0034-4257(02)00114-1)

- Homer CG, Dewitz JA, Yang L, Jin S, Danielson P, Xian G, Coulson J, Herold ND, Wickham JD, Megown K (2015) Completion of the 2011 national land cover database for the conterminous united states—representing a decade of land cover change information. *Photogramm Eng Remote Sens* 81:345–354
- Jenson SK, Domingue JO (1988) Extracting topographic structure from digital elevation data for geographic information system analysis. *Photogramm Eng Remote Sens* 54:1593–1600
- Kerr-Upal M, Stone M, Seters TV, Whitehead G, Price J (1999) Assessing the risk of groundwater nitrate contamination in the Region of Waterloo, Ontario, Canadian. *Water Resour J* 24:225–233. doi:10.4296/cwrj2403225
- Kobal M, Bertoneclj I, Pirotti F, Dakskobler I, Kutnar L (2015) Using lidar data to analyse sinkhole characteristics relevant for understory vegetation under forest cover—case study of a high karst area in the Dinaric Mountains. *PLoS ONE*. doi:10.1371/journal.pone.1022070
- Lindsay JB, Creed IF (2006) Distinguishing actual and artefact depression in digital elevation data. *Comput Geosci* 32:1192–1204. doi:10.1016/j.cageo.2005.11.002
- Mayer JH (2002) Evaluating natural site formation processes in eolian dune sands: a case study from the Krmopotich Folsom site, Killpecker Dunes, Wyoming. *J Archaeol Sci* 29:1199–1211. doi:10.1006/jasc.2001.0803
- NWFWMD (2015) NWFWMD public LiDAR data server. <http://www.nwfwmdlidar.com/>. Accessed 1 Aug 2013
- Olsen SJ (1958) Wakulla cave. *Natural History* 67:386–404
- Palmer AN (1981) A geological guide to mammoth cave national park. Zephyrus Press, Teaneck
- Paylor RL, Florea LJ, Caudill MJ, Currens JC (2003) A GIS coverage of Sinkholes in the Karst Areas of Kentucky: Kentucky Geological Survey, metadata file and shapefiles of highest elevation closed contours, 1 CDROM. A single CDROM. Kentucky Geological Survey
- Puri HS, Vernon RO (1964) Summary of the geology of Florida and a guidebook to the classic exposures. Special publication no. 5. Florida Geological Survey, Tallahassee
- Rahimi M, Alexander EC Jr (2013) Locating sinkholes in LiDAR coverage of a glacio-fluvial karst, Winona County, MN. In: Land L, Doctor DH, Stephenson JB (eds) Sinkholes and the engineering and environmental impacts of karst: proceedings of the thirteenth multidisciplinary conference, May 6–10, Carlsbad, New Mexico. NCKRI symposium 2. National Cave and Karst Research Institute, Carlsbad, pp 469–480
- Sanderson M, Karrow PF, Greenhouse JP, Paloschi GVR, Schneider G, Mulamoottil G, Mason C, McBean EA, Fitzpatrick PN, Mitchell B, Shrubsole D (1995) Groundwater contamination in the Kitchener–Waterloo area, Ontario. *Can Water Resour J* 20:145–160. doi:10.4296/cwrj2003145
- Scott TM (2001) Text to accompany the geological map of Florida. Florida Geological Survey, Tallahassee, Florida
- Seale LD, Florea LJ, Vacher HL, Brinkmann R (2008) Using ALSM to map sinkholes in the urbanized covered karst of Pinellas County, Florida—1, methodological considerations. *Environ Geol* 54:995–1005. doi:10.1007/s00254-007-0890-8
- Shunk AJ, Driese SG, Clarke GM (2006) Latest Miocene to earliest Pliocene sedimentation and climate record derived from paleosinkhole fill deposits, Gray Fossil Site, northerneastern Tennessee, USA. *Paleogeogr Palaeoclimatol Palaeoecol* 231:265–278. doi:10.1016/j.palaeo.2005.08.001
- Slatton KC, Carter WE, Shrestha RL, Dietrich W (2007) Airborne laser swath mapping: achieving the resolution and accuracy required for geosurficial research. *Geophys Res Lett*. doi:10.1029/2007GL031939
- Stotler RL, Frapce SK, El Mugammar HT, Johnston C, Judd-Henrey I, Harvey FE, Drimmie R, Jones JP (2011) Geochemical heterogeneity in a small, stratigraphically complex moraine aquifer system (Ontario, Canada): interpretation of flow and recharge using multiple geochemical parameters. *Hydrogeol J* 19:101–115. doi:10.1007/s10040-010-0628-7
- Tharp TM (1999) Mechanics of upward propagation of cover-collapse sinkholes. *Eng Geol* 52:23–33. doi:10.1016/S0013-7952(98)00051-9
- Thornberry-Ehrlich T (2011) Mammoth Cave National Park: geologic resources inventory report. Natural Resource Report NPS/NRSS/GRD/NRR–2011/448. National Park Service, Fort Collins, Colorado
- Upchurch SB (2007) An introduction to the Cody Escarpment, North-Central Florida. Prepared for the Suwannee River Water Management District by Sam B. Upchurch, SDII Global Corporation
- Veni G, DuChene HR, Crawford NC, Groves CG, Huppert GN, Kastning EH, Olson R, Wheeler BJ (2001) Living with Karst: a fragile foundation. AGI environmental awareness series, no. 4. American Geological Institute, Alexandria, Virginia
- Wall J, Doctor DH, Terziotti S (2015) A semi-automated tool for reducing the creation of false closed depression from a filled lidar-derived digital elevation model. In: Doctor DH, Land L, Stephenson JB (eds) Sinkholes and the engineering and environmental impacts of karst: proceedings of the fourteenth

- multidisciplinary conference, October 5–9, Rochester, Minnesota. NCKRI symposium 5. National Cave and Karst Research Institute, Carlsbad, NM, pp 255–262
- Weary DJ, Doctor DH (2014) Karst in the United State: a digital map compilation and database. US Department of the Interior. US Geological Survey Open-File Report 2014-1156. <http://dx.doi.org/10.3133/ofr20141156>
- White WB, Watson RA, Pohl ER, Brucker R (1970) The central Kentucky karst. *Geogr Rev* 60:88–115
- Zandbergen PA (2010) Accuracy considerations in the analysis of depressions in medium-resolution LiDAR DEMs. *GISci Remote Sens* 47:187–207
- Zhu J, Taylor TP, Currens JC, Crawford MM (2014) Improved karst sinkhole mapping in Kentucky using LIDAR techniques: a pilot study in Floyds Fork Watershed. *J Cave Karst Stud* 76:207–216

CHAPTER 3

A novel workflow for identifying sunken graves utilizing ultra-high-resolution topographic data and machine learning

The contents of Chapter 3 have been prepared for submission to the *Journal of Archaeological Science* with the following co-authors:

Bohnenstiehl, D. R.¹; Levine, N. S.²; Wegmann, K.W.¹

¹ Department of Marine, Earth, and Atmospheric Sciences, NC State University, Raleigh, North Carolina, USA

² Department of Geology and Environmental Geosciences, College of Charleston, Charleston, South Carolina, USA

Abstract

In times of peace and war, individuals may be buried in graves that have no identifying marker, or their marker may be lost through time. The absence of grave markers hinders the identification of buried people in both cemeteries and unofficially recognized interment sites. Oberlin Cemetery, located in Raleigh, North Carolina, U.S.A., is a 3.20-acre ($\sim 13,000 \text{ m}^2$) parcel of land that has served the people of Oberlin Village, the largest historic Freedmen's community in Wake County, from 1873 to present-day. Utilizing Oberlin Cemetery as a field site, a method to automatically detect small, closed depressions (i.e. sunken graves) via terrain analysis and machine learning is developed. This method is evaluated against 318 sunken graves identified both by field observation and within a digital elevation model (DEM) derived from terrestrial laser scanning data. A roving window filter was passed over a 0.10 m cell size DEM to locally detrend the data. The detrended raster was then used as input into a fill-difference routine resulting in a depth raster that was then contoured at 0.01 m intervals. Thirteen morphometrics were calculated for each contour to use as predictor variables. Roughly half of the contours ($n = 979$) were manually classified as 'likely' or 'unlikely' to represent sunken graves which were then used to train, validate, and test a binary classification tree. Using interaction-curvature to determine predictor importance, orientation, contour perimeter, elongation shape factor, and difference shape factor were identified as the most important morphometrics in determining the likelihood of a contour representing a sunken grave. The resulting tree had an estimated accuracy of 82.45%. The entire contour data set was then classified with the resulting 'likely' contours dissolved into one another. This resulted in a catalog of 448 confirmed or probable sunken graves at Oberlin Cemetery. The automated detection method presented in this study utilizes the

topographic signal of sunken graves to increase the accounting accuracy of individuals buried within a site and is expandable to other cemeteries and burial sites.

Introduction

Methodological background and motivation

When individuals are interred within the shallow subsurface, areas of local subsidence can develop in response to the compaction of backfilled sediments, the decomposition of remains, or the collapse of a casket within the subsurface. If burial sites are not maintained over time, these processes may lead to the development of closed topographic depressions, more commonly known sunken graves. For graves that are not identified by headstones, or other markers, these depressions may provide the only evidence for the interment of individuals. Despite the ubiquity of closed topographic depressions in many older cemeteries and potential utility as a grave identifier, few studies have attempted to describe (Amari and Alsulaimani, 2016) or inventory (Bon-Harper et al., 2003; Wall et al., submitted) these features.

Sunken graves are geomorphically analogous to sinkholes. Recent efforts to automate the process of cataloging sinkholes have utilized high-resolution elevation data (~1 m gridding) derived from airborne light detection and ranging (lidar) systems. The most successful approach, when judged against field- and aerial-based inventories, have applied a hydrological routine to fill closed depressions within a digital elevation model (DEM) (Zhu et al., 2014; Doctor and Young, 2013; Kobal et al. 2015; Bauer, 2015; Wall et al, 2017). The original DEM is then subtracted from the filled surface model, creating a depth raster from which sinks are defined.

Airborne lidar data has also been widely used for archaeological prospection, particularly in areas where forest canopy limits the effectiveness of aerial photography and other passive remote sensing techniques. Much of the focus has been on manually identifying sites, using hill shades and contrast image filtering visualization techniques (Bewley et al., 2005; Doneus and Briese, 2006; Hesse, 2010; Chase et al., 2011). More recently, template-matching methods have

been used to detect individual archaeological features (e.g., pits, and mounds) within lidar-derived DEMs (Trier et al., 2015; Schnider et al., 2015). This approach, however, can require a large suite of pre-defined templates to represent variability in the shapes of these features, and in practice, this leads to high error of commission rates that limit the utility of the technique (e.g., Sevara et al., 2016).

Archaeological features at the scale of an individual burial are not likely to be detectable in airborne lidar datasets. Sunken graves, however, can be resolved using terrestrial laser scanning (TLS) equipment that is capable of generating centimeter-to-decimeter scale DEMs (e.g., Weitman, 2012; Aziz et al., 2016; Wall et al., submitted). This paper develops a workflow that applies a modified fill-difference method, developed for karst sinkhole identification, to an ultra-high-resolution DEM for the purpose of automating the detection of sunken graves.

In 2016, a TLS survey and location-enabled pedestrian inventory were conducted at Oberlin Cemetery located near downtown Raleigh, North Carolina, U.S.A. (**Fig. 1**). The cemetery was formally founded in 1873 during the Reconstruction Era (1865-1877) and records the vernacular cultural traditions of death in a Freedmen's community, Oberlin Village, through the Jim Crow Era (1870's to 1950's) to the modern day. Wall et al. (submitted) reports the results of a pedestrian survey of Oberlin Cemetery, which includes a visual cataloging of more than three hundred sunken graves—most of which are not associated with grave markers. The undulating topography created by these sunken graves, along with vegetation within the site, were found to limit the utility of ground penetrating radar surveys at Oberlin Cemetery. This led Wall et al. (submitted) to consider the presence of a closed depression (sunken grave) as the primary line of evidence for a burial and for the motivation behind the development of a new technique to systematically identify sunken graves based on their topographic signature. The

detection approach uses a binary classification tree, trained using field observations, to classify closed-contours from a fill-difference derived depth raster based on their morphometric properties. The final catalog of sunken graves is created by dissolving nested closed-contours classified as ‘likely’ associated with a sunken grave.

Geomorphology, geology, and pedology

Oberlin Cemetery is comprised entirely of Cecil series soils, which are derived from quartzofeldspathic gneisses and mica schists (Soil Survey Staff, 2017; Stoddard et al., 1991). Cecil soils are gently sloping, well-drained, and deep with moderate permeability, water capacity, and shrink-swell potential (Cawthorn, 1970). The soil A-Horizon ($\leq 0.15\text{-}0.20$ m) consists of a sandy loam while the remaining horizons are generally comprised of clay that reverts to loam between 0.86 and 1.05 m (Soil Survey Staff, 2017). The depth to water table in this area is estimated to be more than 2.00 m (Soil Survey Staff, 2017) while the depth to bedrock is between 1.83 and 3.05 m (Soil Survey Staff, 2006). Raleigh has an mean annual temperature of 16° C that ranges from 5° C in January to 26° C in July and enjoys an average of 1.10 m of annual precipitation (NOAA Online Weather Data, 2006). The combination of temperature and abundant moisture causes the rapid decomposition of organic matter and hastens chemical reactions in the soils and near-surface bedrock.

Data and methods

Topography survey

A TLS survey was carried out within Oberlin Cemetery during the winter of 2016. A total of 26 scan positions, at ~ 25 m spacing, were occupied using a Leica HDS3000 laser scanner (**Fig. 2A**). The instrument was configured for a minimum acquisition point spacing of 0.02 m and a maximum scan range of 30 m. Scans were tied together in Leica Cyclone 9.1.4 to create a

single, unified point cloud. Tie points for georeferencing the cloud were established in the field using the corners of ten monuments and their positions were surveyed using a Trimble R10 GNSS-VRS (Global Navigation Satellite System using a Virtual Reference Station) receiver. The TLS onboard camera was not functioning during the survey resulting in only three tie points being able to be identified and used. The georeferenced RMSE of the survey was 0.80 m. Points within the cloud were classified using LASTools (Isenburg, 2014) with ‘wilderness’ and ‘hyper-fine’ flags enabled. Ground-classified points were then thinned and gridded at a spatial resolution of 0.10 m. This resolution is an order of magnitude finer than commonly available datasets recorded from airborne platforms (e.g. Doctor and Young, 2013; Zhu et al., 2014; Wu et al., 2016). Using this grid size, 13.38% of cells have ≤ 1 point per cell. The remaining 86.62% have two or more points per cell, with the average standard deviation of elevation points within a cell being 0.01 m (**Fig. 2B**) The spatial distribution of optimally versus sub-optimally constrained points are shown in **Figure 2C** where most of the sub-optimally constrained pixels are where dense vegetation was present. For grid cell locations without sufficient lidar points, but within two meters of cells with sufficient points, the elevation value was interpolated to create a DEM (**Fig. 2D**).

Field Observations

Pedestrian survey data were recorded during summer 2016 using a GNSS-VRS receiver paired with a cellphone running Trimble’s TerraFlex application (Wall et al., submitted). The horizontal uncertainty of the positions ranged between 0.01-1.58 m, with an average of 0.17 m. In addition to inventorying headstones and other monuments within the cemetery, the survey initially cataloged 357 topographic depressions, which were interpreted in the field as sunken graves based on their shape, size, and orientation. The southwest corner position of each

depression was recorded, along with its length, width, and depth as measured using a tape. To facilitate later comparisons with the TLS data, no attempt was made to remove leaf litter and vegetation prior to making these measurements.

To accommodate uncertainty in the positioning data, sunken graves identified during the pedestrian survey were manually matched with the centroids of their corresponding local depressions observed in the DEM. A total of 39 sunken graves identified in the field could not be uniquely correlated with TLS recorded topography, resulting in a catalog of 318 sunken graves (**Fig. 3**). Of these 265 were unmarked, with only 53 graves associated with headstones, footstones, or other markers. The field-recorded metrics for these 318 features are described in **Table 1**.

Grave Detection from Ultra-High-Resolution Topographic Data

The cataloging of sunken graves is a novel process outlined by **Figure 4**. It was implemented here within ArcGIS 10.5.1, but could be applied within most geographic information systems. A Topographic Position Index (TPI) was calculated on the DEM. The TPI employs a roving window filter to locally detrend the elevation data thereby elucidating geomorphic features at the scale of the window (Jenness, 2013). While various window shapes can be used for a TPI, an annulus, defined by inner and outer radii, was used here. The resulting TPI raster was then hydrologically conditioned using the *Fill* tool within the ArcGIS *Hydrology Toolbox*. This tool is usually employed to ensure stream delineation is not impacted by small errors in elevation data; however, in some geomorphic settings, such as karst terrain, these depressions are likely to be real features (cf. Lindsay and Creed, 2006; Zandbergen, 2010). The initial TPI raster was then subtracted from the filled TPI raster resulting in a depth raster. This hydrologic conditioning and differencing method is similar to the fill-difference method outlined

by Doctor and Young (2013) with the exception of a TPI raster being used. The resulting depth raster was then contoured at the vertical accuracy of the elevation data (0.01 m). Closed-contours were then saved for further analysis if their area were within the 95% quantile range (1.0-2.7 m²) of sunken graves recorded during the pedestrian survey (Wall et al., submitted).

A variety of inner and outer radii pairs were tested for the TPI (**Table 2**). The optimal combination was determined by converting derived contours to polygons and then spatially intersecting them with field identified graves to determine a collocation or capture ratio. An inner radius of 0.70 m and outer radius of 0.90 m was found to capture the greatest percentage (90%) of field observed sunken graves and was adopted for this study.

Maximum, mean, and standard deviation of depths within each closed-contour (n = 1,763) were calculated using the *Zonal Statistics as Table* tool within the *Spatial Analyst Toolbox*. Major (i_{major}) and minor (i_{min}) axes length as well as major axis orientation were calculated using the *Minimum Bounding Geometry* (MBG) tool, which fits each contour-polygon obtained from the depth raster with a rectangle of the smallest enclosing area. Contour and MGB perimeter (P_C , P_{MBG}) and area (A_C , A_{MBG}) were automatically calculated and stored within a File Geodatabase. Elongation (F_{elong}), circularity (F_{circ}), and compactness (F_{comp}), shape factors (**Table 3**) were calculated in Microsoft Excel.

Classifying detections with machine learning

At least one closed-contour associated with each field identified sunken grave was classified as ‘likely’, as were additional closed-contours displaying a highly idealized ellipse shape (**Fig. 5A, B**) (n = 511). For depressions bound by concentric-contours, two contours were classified to minimize cartographic area bias. Closed-contours not associated with field observed sunken graves and interpreted as delineating depressions within the natural landscape were

classified as ‘unlikely’ (**Fig. 5C**) ($n = 468$), with an additional 784 closed-contours left unclassified. Classified contours were randomly split into training and validation ($n = 734$) and testing ($n = 245$) sets. Using the contour metrics describe above, a binary classification tree (‘likely’ or ‘unlikely’) was grown within MATLAB 2017a. Predictor selection was determined using interaction-curvature, which minimizes the p-value of a chi-square test of independence between each predictor and the response as well as each pair of predictors and the response (Loh, 2002). This selection method is ideally suited to constraining the importance of each predictor especially in the presence of irrelevant variables. Predictor importance was estimated by summing changes in risk due to splits on every predictor and dividing by the sum of branch nodes (Mathworks, 2018).

An initial tree was grown using Gini’s diversity index for determining splits. This tree was pruned using the $1 - SE$ rule where the best pruning level is the one that has an estimated error rate within one standard error of the minimum (**Fig. 6**) (Breiman et al., 1984). Using a ten-fold cross-validation model, the pruned tree had a loss rate of 18.05% (Mathworks, 2018). Predictor importance for the pruned tree indicated that out of the initial 13 metrics, only orientation, contour perimeter, elongation shape factor, and compactness shape factor were important (**Fig. 7**). The withheld test data was then used to determine the predictive tendencies of the model. The estimated accuracy was 82.45%. The confusion matrix (**Fig. 8**) indicates 15.4% of contours classified as ‘unlikely’ to be associated with sunken graves are errors of omission, while 20.2% of the contours classified as ‘likely’ are errors of commission.

Results

Utilizing a binary classification tree on the entire contour catalog, 1,039 (58.93%) contours were identified as ‘likely’ associated with sunken graves (**Fig. 9**), while 724 (41.07%)

were identified as ‘unlikely.’ Of the ‘likely’ contours, 734 collocated with 238 (74.84%) sunken graves observed in the field. The remaining 305 ‘likely’ contours describe 210 additional sunken graves for a total of 448 confirmed or probable sunken graves at Oberlin Cemetery. While there is some level of ambiguity in the total catalog size due to errors of omission and commission, this same issue would be encountered with more traditional, manual classification methods.

Of the field identified sunken graves at Oberlin Cemetery that could also be visually identified in the TLS derived DEM, 80 (26.41%) were not identified by the method outlined here (**Fig. 10**). The automatically created contours associated with 32 field observations had areas that were outside the 95% quantile range (1.0-2.7 m²) recorded during the pedestrian survey (**Fig. 11A**). The remaining 48 field observations excluded by the binary classifier were associated with depressions having morphologies that deviated significantly from those in the training dataset (**Fig. 11B**). Of these 48, seven correlated with contours in two-to-one relationship due to the sunken graves coalescing into one another. The remaining 34 field observed sunken graves collocate with 48 closed-contours, all of which were classified as ‘unlikely’ based on their perimeter (28), elongation (10), orientation (7), or difference (3).

Discussion

Lidar recorded from airborne platforms, that was of sufficient resolution for site identification, has been used to identify barrow mounds, pits, and other cemetery features with dimensions on the order of a few meters (e.g., Crutchley, 2006; Cerillo-Cuenca, 2016). Automated identification of these archaeological features has relied primarily on template-matching routines. Trier and Pilø (2012), for example, used 12 circular templates, with radii 1.2-3.4 m, passed over a 1-meter resolution DEM, to identify smelting pits within two forests of Oppland County, Norway. While the capture rate for these pits, when judged against field

surveys, was 83.2%, nearly 80% of all detections were errors of commission. Schneider et al. (2015) mapped charcoal kiln sites using template-matching operating on a 1-meter scale DEM from an area near Jänschwalde, Germany. They report a similarly high capture rate (73.9%), with 44.6% of all detections representing errors of commission.

While individual sunken graves occur at scales too small to be detected in airborne lidar datasets, they can be imaged using terrestrial scanning systems (Weitman, 2012 and Aziz et al., 2016), which yield much higher point densities and support the gridding of DEMs with ~0.10 m resolution. TLS data, as with lidar systems on other platforms, can record topographic data below vegetation (Crutchley and Crow, 2009). At Oberlin Cemetery, this was useful when imaging areas with grass and sparse ivy (*Hedera helix*) cover, but somewhat less effective in the most densely covered areas. In areas with little-to-no vegetative cover, topographic data obtained by high-resolution photogrammetric methods (i.e. Structure from Motion) can also utilize the cataloging method presented in this paper. Such an approach to topographic data acquisition may have a lower operational cost and can be less time intensive if conducted using a small unmanned aerial vehicle (drone).

In this study, we have used a machine learning approach to classify contours, as opposed to a template matching approach, which has been used in most previous archaeological studies aimed at terrain feature identification. This choice reflects the amount of variability observed in the depth, size, and shape of the sunken graves, which would require an exceedingly large set of templates. While the results of this study cannot be directly compared to previous efforts to identify archaeological features in coarser-resolution DEMs (e.g., Trier and Pilø, 2012; Schneider et al., 2015), they demonstrate the potential for machine learning based approaches to provide similar capture rates (74.84%) and lower errors of commission rates (20.2%). In many

DEM-based template-matching studies, high error of commission rates (40-70%) have necessitated catalog cleaning methods, commonly using manual review. Machine learning approaches, which might use detection scores and other predictors derived from a DEM, could be used to create archaeological feature classifiers that are more fully automated.

In our investigation of sunken graves at Oberlin Cemetery, 13 morphometric descriptors were originally calculated for each closed-contour; however, only orientation, contour perimeter, elongation shape factor, and difference factor were found to be useful in determining if a contour was 'likely' or 'unlikely' to be associated with a sunken grave. The binary classification tree trained, tested, and validated here can be further refined and/or applied at other sites.

Wall et al. (submitted) estimated that 517 to 660 individuals are buried at Oberlin Cemetery based on field observations. Burials of 357 individuals were determined from their topographic expression alone, or in association with grave markers (e.g. headstones, fieldstones, flower holders). Of the 357 sunken graves observed in the field, 318 could additionally be observed in the TLS derived 0.1-meter resolution DEM. The automated method identified 238 of these graves, as well as an additional 210 not identified by field observations, resulting in a total count of 448 sunken graves. The 91 sunken graves observed in the field and TLS data that were not automatically cataloged were missed due to being outside the area threshold ($n = 32$) or having deviant morphologies ($n = 48$).

Conclusions

The workflow outlined here, a modification of the fill-difference method, is an effective tool for cataloging sunken graves when compared to field observations. Of the 13 morphometrics calculated for each contour, orientation, contour perimeter, elongation shape factor, and compaction shape factor were determined to be the most important predictors in determining if a

contour was associated with a sunken grave or not. The likelihood of a contour being associated with sunken graves was determined using a binary classification tree which had a test accuracy of 82.45%. The method was able to identify 74.84% (n = 238) of the field observed sunken graves. A further 210 sunken graves were identified by this method that were not identified in the field for a total of 448 confirmed or probable sunken graves. Sunken topography therefore identifies 46.03 to 67.88% of burials at Oberlin Cemetery.

The approach outlined here uses morphometrics and machine learning to determine if a detected topographic feature is associated with a sunken grave, thereby removing subjective decision making; furthermore, this approach can be fully automated and other studies can utilize the classification tree developed herein. While TLS data was used here due to vegetation cover, the method can operate on any ultra-high-resolution (≤ 0.10 m) topographic dataset. Given the high proportion of sunken graves identified at Oberlin Cemetery, this method can be used at other sites to identify burial places of people that were not only marginalized in life (e.g. African American slaves, freedmen, and victims of war atrocities as well as genocides), but, due to the scarcity of research on unmarked sunken graves, in death as well.

Acknowledgements

We would like to thank the Friends of Oberlin Village and InterAct for facilitating access to the Cemetery. The Santee Cooper Geographic Information Systems Laboratory for providing the Leica HDS3000. Justin Barton for his help while carrying out the lidar scanning and referencing the data as well as providing Cyclone licenses. Dan Doctor for his review of the manuscript.

References

1. Amari IEA, Alsulaimani GS. Detecting and Imaging Historical Graves by Using Visual Inspection and Ground Penetrating Radar Investigation Detecting and Imaging Historical Graves by Using Visual Inspection and Ground Penetrating Radar Investigation. *Int J Res Eng Sci.* 2016;4(10):1-9.
2. Aziz AS, Stewart RR, Green SL, Flores JB. Locating and characterizing burials using 3D ground-penetrating radar (GPR) and terrestrial laser scanning (TLS) at the historic Mueschke Cemetery, Houston, Texas. *J Archaeol Sci Reports.* 2016;8:392-405. doi:10.1016/j.jasrep.2016.06.035.
3. Bauer C. Analysis of dolines using multiple methods applied to airborne laser scanning data. *Geomorphology.* 2015;250:78-88. doi:10.1016/j.geomorph.2015.08.015.
4. Bewley RH, Crutchley SP, Shell CA. New light on an ancient landscape : lidar survey in the Stonehenge World Heritage Site. 2005;79(August 2004):636-647.
5. Bon-Harper S, Neiman F, Wheeler D. *Monticello's Park Cemetery, Monticello Department of Archaeology Technical Report Series Number 5.*; 2003. <https://www.monticello.org/archaeology/publications/parkcemetery.pdf>.
6. Breiman L, Friedman JH, Olshen RA, Stone CJ. *Classification and Regression Trees.* Boca Raton, Florida: Chapman & Hall; 1984.
7. Cawthorn JW. *Soil Survey: Wake County North Carolina.*; 1970. https://www.nrcs.usda.gov/Internet/FSE_MANUSCRIPTS/north_carolina/wakeNC1970/text.pdf.
8. Cerrillo-Cuenca E. An approach to the automatic surveying of prehistoric barrows through LiDAR. *Quat Int.* 2017;435(May):135-145. doi:10.1016/j.quaint.2015.12.099.
9. Chase AF, Chase DZ, Weishampel JF, et al. Airborne LiDAR, archaeology, and the ancient Maya landscape at Caracol, Belize. *J Archaeol Sci.* 2011;38(2):387-398. doi:10.1016/j.jas.2010.09.018.
10. Crutchley S. Light detection and ranging (lidar) in the Witham Valley, Lincolnshire: an assessment of new remote sensing techniques. *Archaeol Prospect.* 2006;13(4):251-257. doi:10.1002/arp.294.
11. Doctor DH, Young JA. An Evaluation of Automated Gis Tools for Delineating Karst Sinkholes and Closed Depressions From 1-Meter Lidar-Derived Digital Elevation Data. *Thirteen Multidiscip Conf Sink Eng Environ Impacts Karst.* 2013:449-458.
12. Doneus M, Briese C. Full-waveform airborne laser scanning as a tool for archaeological reconnaissance. In: Campana S, Forte M, eds. *From Space to Place: 2nd International Conference on Remote Sensing in Archaeology. Proceedings of the 2nd International*

- Workshop, CNR, Rome, Italy, December 4-7, 2006, BAR International Series 1568.*
Oxford: Archaeopress; 2006:99-106.
13. Exner HE, Hougardy HP. Quantitative Image Analysis of Microstructures. 1988. *DGM Informationsgesellschaft mbH*. Stuttgart and Düsseldorf.
 14. Hesse R. LiDAR-derived Local Relief Models - a new tool for archaeological prospection. *Archaeol Prospect*. 2010;72(December 2009):67-72. doi:10.1002/arp.374.
 15. Isenburg M. LAStools - efficient LiDAR processing software. 2014. <http://rapidlasso.com/LAStools>.
 16. Jenness J, Brost B, Beier P. Land Facet Corridor Designer: Extension for ArcGIS. *Jenness Enterp*. 2013;(January):110. http://www.jennessent.com/arcgis/land_facets.htm.
 17. Kobal M, Bertonecelj I, Pirotti F, Dakskobler I, Kutnar L. Using Lidar Data to Analyse Sinkhole Characteristics Relevant for Understory Vegetation under Forest Cover — Case Study of a High Karst Area in the Dinaric Mountains. *PLOSE One*. 2015:1-19. doi:10.1371/journal.pone.0122070.
 18. Lindsay JB, Creed IF. Distinguishing actual and artefact depressions in digital elevation data. *Comput Geosci*. 2006;32(8):1192-1204. doi:10.1016/j.cageo.2005.11.002.
 19. Loh W. Regression Trees With Unbiased Variable Selection and Interaction Detection. *Stat Sin*. 2002;12:361-386. doi:10.5351/KJAS.2004.17.3.459.
 20. Mathworks. Statistics and Machine Learning Toolbox (r2018a). <https://www.mathworks.com/help/stats/>. Published 2018. Accessed April 12, 2018.
 21. NOAA. NOAA online weather data (NOWData): Interactive data query system. <http://w2.weather.gov/climate/xmacis.php?wfo=rah>. Published 2006. Accessed May 15, 2018.
 22. Schneider A, Takla M, Nicolay A, Raab A, Raab T. A Template-matching Approach Combining Morphometric Variables for Automated Mapping of Charcoal Kiln Sites. *Archaeol Prospect*. 2015;22(1):45-62. doi:10.1002/arp.1497.
 23. Sevara C, Pregesbauer M, Doneus M, Verhoeven G, Trinks I. Pixel versus object - A comparison of strategies for the semi-automated mapping of archaeological features using airborne laser scanning data. *J Archaeol Sci Reports*. 2016;5:485-498. doi:10.1016/j.jasrep.2015.12.023.
 24. Soil Survey Staff, Natural Resources Conservation Service USD of A. Cecil Series. National Cooperative Soil Survey. https://soilseries.sc.egov.usda.gov/OSD_Docs/C/CECIL.html. Published 2006. Accessed February 28, 2018.

25. Soil Survey Staff, Natural Resources Conservation Service USD of A. Web Soil Survey. <https://websoilsurvey.sc.egov.usda.gov/>. Published 2017. Accessed January 1, 2018.
26. Stoddard EF, Farrar SS, Horton JW, Butler JR, Druhan RM. The Eastern Piedmont in North Carolina. In: Horton JW, Zullo V, eds. *The Geology of the Carolinas: Carolina Geological Society Fiftieth Anniversary Volume*. 1st ed. Knoxville: The University of Tennessee Press; 1991:79-92.
27. Trier ØD, Pilø LH. Automatic Detection of Pit Structures in Airborne Laser Scanning Data. *Archaeol Prospect*. 2012;19(2):103-121. doi:10.1002/arp.1421.
28. Trier ØD, Zortea M, Tønning C. Automatic detection of mound structures in airborne laser scanning data. *J Archaeol Sci Reports*. 2015;2:69-79. doi:10.1016/j.jasrep.2015.01.005.
29. Wall J, Bohnenstiehl DWR, Wegmann KW, Levine NS. Morphometric comparisons between automated and manual karst depression inventories in Apalachicola National Forest, Florida, and Mammoth Cave National Park, Kentucky, USA. *Nat Hazards*. 2017;85(2):729-749. doi:10.1007/s11069-016-2600-x.
30. Wall J, Bohnenstiehl DWR, Levine NS, Millhauser JK, McGill DE, Wegmann KW, Melomo. A geospatial and geoarchaeological investigation of an African-American cemetery in Raleigh, North Carolina, USA. *Archaeological and Anthropological Sciences*. (Submitted)
31. Weitman SL. Using Archaeological Methods in Cemetery Surveys with Emphasis on the Application of Lidar. *Electron Theses Diss*. 2012. <http://digitalcommons.georgiasouthern.edu/cgi/viewcontent.cgi?article=1627&context=etd>.
32. Wu Q, Deng C, Chen Z. Automated delineation of karst sinkholes from LiDAR-derived digital elevation models. *Geomorphology*. 2016;266(August):1-10. doi:10.1016/j.geomorph.2016.05.006.
33. Zandbergen P a. Accuracy Considerations in the Analysis of Depressions in Medium-Resolution Lidar DEMs. *GIScience Remote Sens*. 2010;47(2):187-207. doi:10.2747/1548-1603.47.2.187.
34. Zhu J, Taylor TP, Currens JC, Studies K. IMPROVED KARST SINKHOLE MAPPING IN KENTUCKY USING LIDAR TECHNIQUES : A PILOT STUDY IN FLOYDS FORK WATERSHED. *J Cave Karst S*. 2014;76(3):207-216. doi:10.4311/2013ES0135.

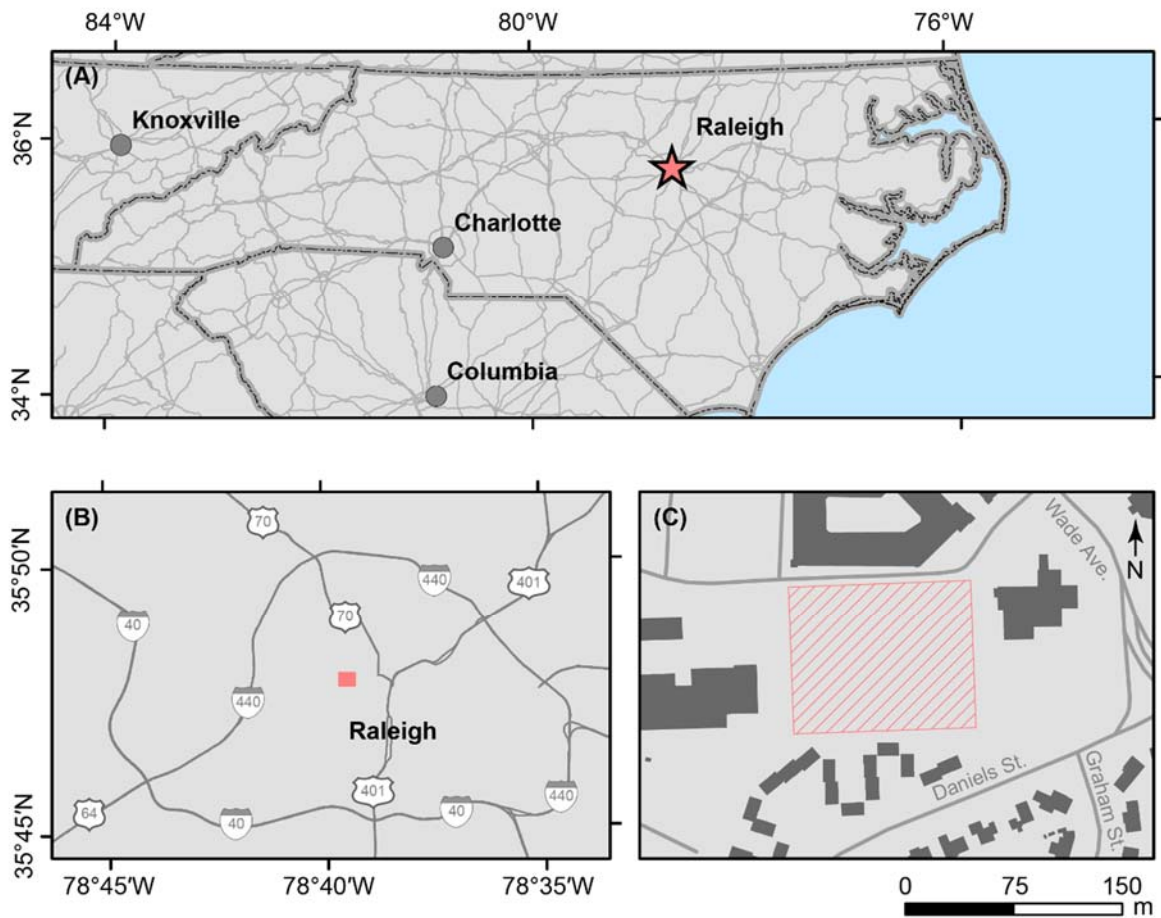
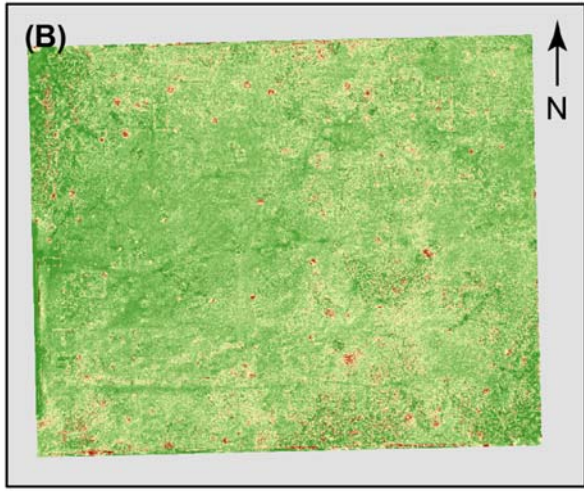
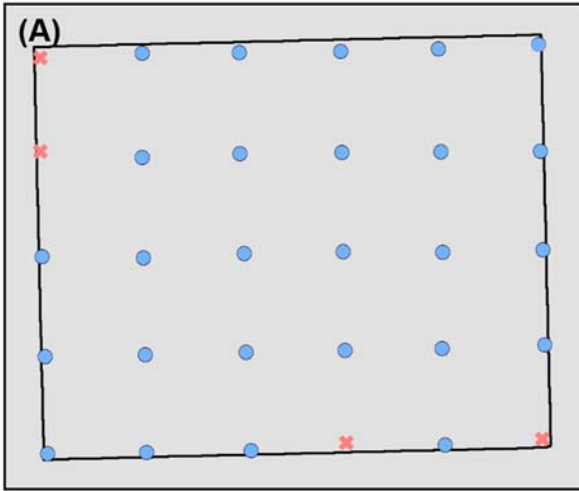
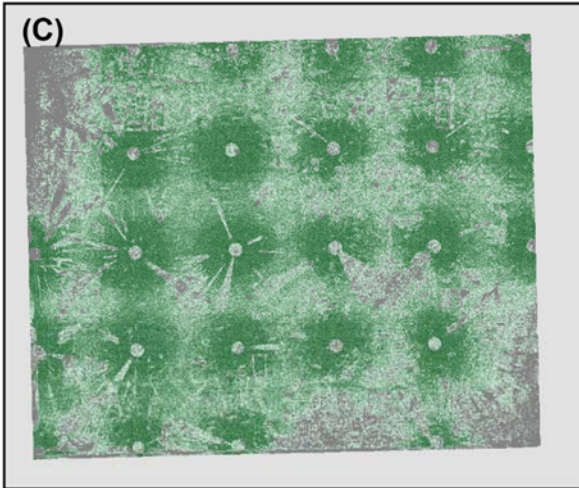
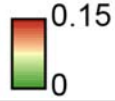


Figure 1. (A) Raleigh is located in central North Carolina. (B) Just north-west of downtown Raleigh, Oberlin Cemetery (pink square) occupies a 3.2-acre (1.3-hectare) plot of land. (C) To the north of the cemetery (pink hachured square) are the Oberlin Court Apartments while to the south are the Cameron Village Condominiums. Flanking the cemetery to the east and west are the Occidental Life Insurance and InterAct office buildings, respectively.

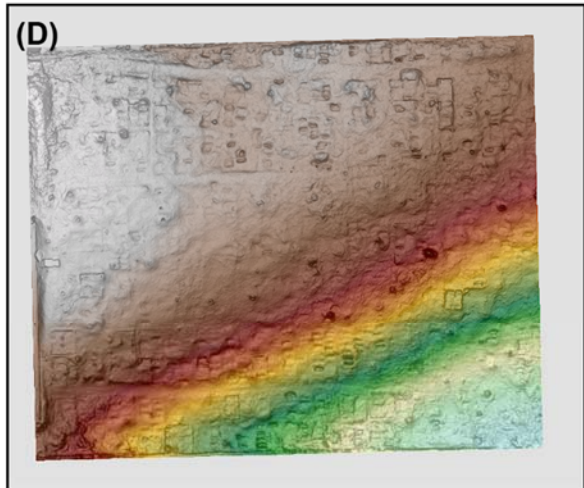
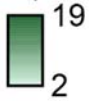
Figure 2. (A) Locations for 26 scans (blue dots) that were carried out with a Leica HDS3000 Terrestrial Laser Scanner (TLS) within Oberlin Cemetery. Planned scans at four locations (pink crosses) could not be conducted due to dense vegetation. These scans were combined into a unified point cloud within Leica Cyclone. Ground returns were identified and classified with LAStools. (B) Vertical accuracy of elevation values within a 0.10 m grid was assessed using the standard deviation of elevation values within each cell ($\mu = 0.01$ m). (C) Using this grid resolution of 0.10 m, 13.38% of cells had ≤ 1 point per cell (dark grey) while 86.62% have two or more points per cell. Optimally constrained cells had 2 to 19 points per cell. Most of the sub-optimally constrained cells were in areas of dense vegetation. (D) A digital elevation model (DEM) was gridded from ground classified points where cells with ≤ 1 point per cell were interpolated from TLS points located within two meters. Color-shading shows the derived DEM with a draped slope-shade.



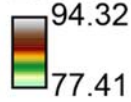
Std. of Elevations (m/0.01 m²)

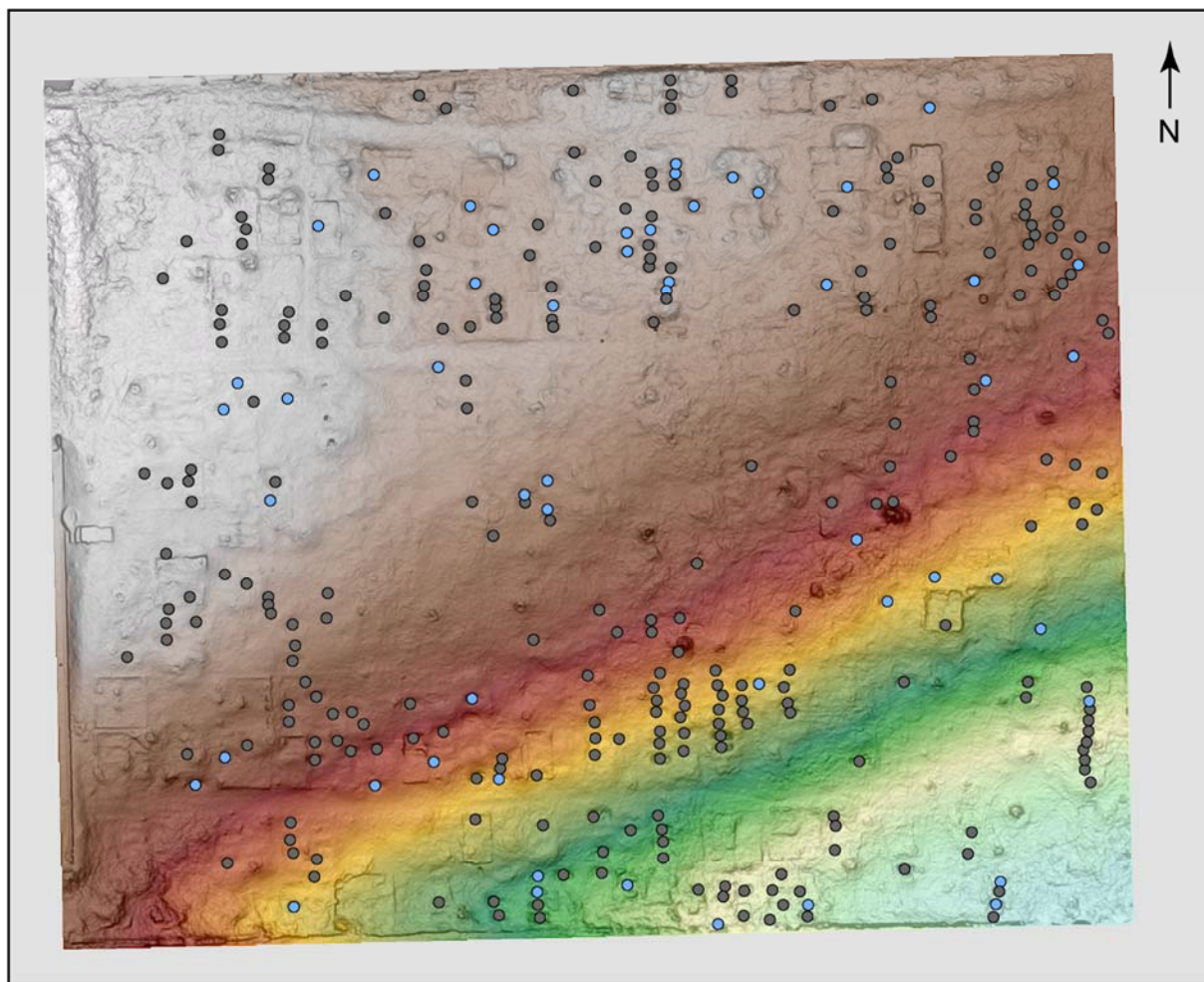


Optimal Point Density (points/0.01 m²)



Elevation (m)





Elevation (m)
 94.32
 77.41

0 50 m

Figure 3. Distribution of field observed sunken graves which could also be identified in the terrestrial laser scanning derived digital elevation model (n = 318). The majority (n = 265) of these sunken graves were identified without associated material culture (grey dots) while 53 were associated with headstones, fieldstones, flower holders and other material culture (blue dots).

Table 1. Field recorded metrics for sunken graves at Oberlin Cemetery.

	Minimum	Maximum	Mean	Standard Deviation
<i>Length (m)</i>	1.10	2.88	2.19	0.28
<i>Width (m)</i>	0.44	2.12	0.92	0.22
<i>Depth (m)</i>	0.01	1.18	0.14	0.11

Figure 4. A schematic for automatically identifying sunken graves within an ultra-high-resolution digital elevation model (DEM). An initial DEM is locally detrended using a Topographic Position Index (TPI) with an annulus window. The TPI is then hydrologically conditioned using the *Fill* tool within the ArcGIS *Hydrology Toolbox*. This fills depressions within the TPI such that synthetic streamflow would be routed over depressions and to the edge of the raster. The initial TPI is then subtracted from the filled TPI to create a depth raster which is contoured with an interval equal to the vertical accuracy of the DEM (0.01 m). These contours are then converted to polygons and thresholded during processing to two standard deviations from the observed mean grave area ($1.00 \text{ m}^2 < A_{field} < 2.72 \text{ m}^2$). Conversion must happen in a for-loop within Python, ArcGIS Model Builder, or equivalent. A simple conversion to polygons (i.e. *Feature to Polygon* in ArcGIS) results in the intra-contour spacing being converted to polygons opposed to the entire area that the contour covers.

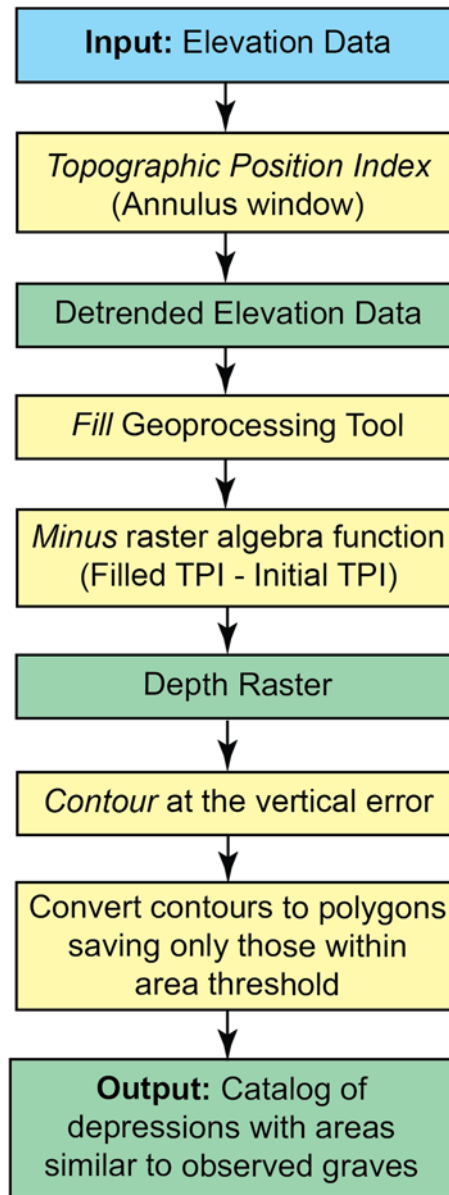


Table 2. Tested annulus inner and outer radii to determine optimal values. Capture ratio is calculated by: 1) converting contours to polygons; 2) thresholding polygons to two standard deviations of the observed area ($1.00 \text{ m}^2 < A_{field} < 2.72 \text{ m}^2$); and 3) and using a Select by Location on field observations ($n = 318$). This identified 0.70 m inner and 0.90 m outer radii (italicized) as optimal with a capture ratio of 90%.

Inner Radius (m)	Outer Radius (m)	Capture Ratio (%)
0.10	0.30	3
0.10	0.50	41
0.10	0.70	47
0.10	0.90	85
0.30	0.50	56
0.30	0.70	77
0.30	0.90	85
0.50	0.70	85
0.50	0.90	89
0.50	1.00	89
0.50	1.50	87
0.50	2.00	83
0.50	2.50	77
0.50	3.00	74
<i>0.70</i>	<i>0.90</i>	90
1.00	1.50	88
1.00	2.00	81
1.00	2.50	77
1.00	3.00	72
1.50	2.00	79
1.50	2.50	74
1.50	3.00	69
2.00	2.50	71
2.00	3.00	65
2.50	3.00	61

Table 3. Calculated shape factors from derived contour-polygon metrics.

Metric	Equation	Description	Source
<i>Elongation Factor</i>	$f_{elong} = \sqrt{\frac{i_{minor}}{i_{major}}}$	Square-root of the ratio of minor axis (i_{minor}) length to major axis (i_{major}) length. Major and minor axes are the width and length, respectively, from fitting a rectangle with the smallest area (i.e. minimum bounding geometry [MBG]).	Exner and Hougardy (1988)
<i>Circularity Factor</i>	$f_{circ} = \frac{4\pi A_C}{P_C^2}$	Ratio between the observed, contour-polygon area (A_C) and its perimeter (P_C). A feature with a circularity of one perfect whereas a highly tortured shape is less than one.	Exner and Hougardy (1988)
<i>Difference Factor</i>	$f_{diff} = \frac{(A_{MBG} - A_C)}{A_{MBG}}$	Difference ratio between the MBG area (A_{MBG}) and the contour area (A_C). As a feature fills the MBG, the value approaches unity.	N/A

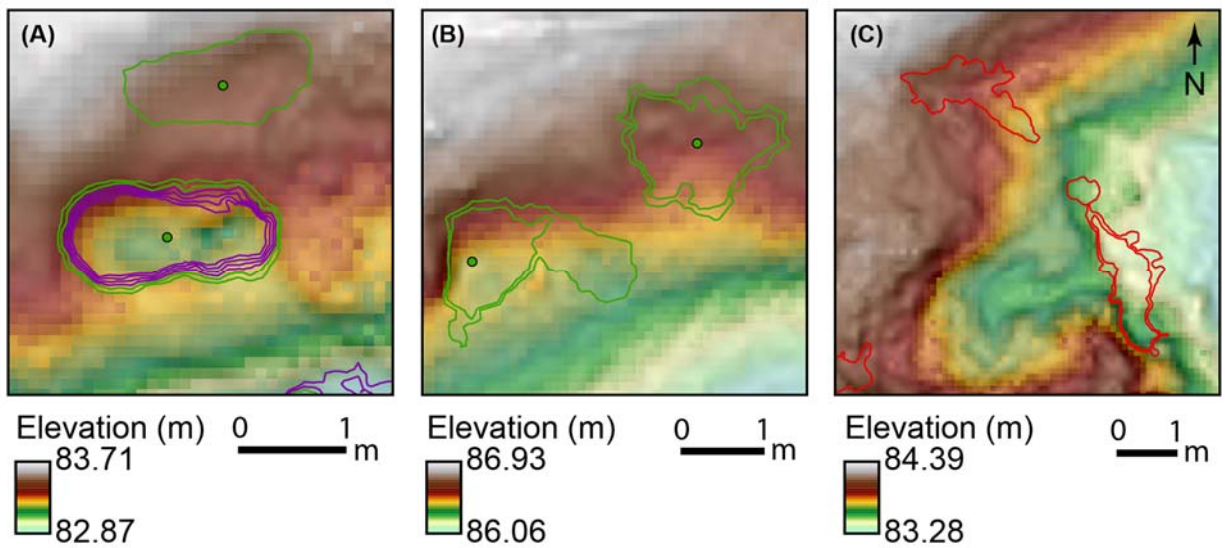


Figure 5. Examples of closed-contours, with a 0.01 m interval, manually classified as ‘likely’ sunken graves (green lines) for training a binary classification tree. A slope-shaded digital elevation model is shown in the background. (A) When concentric closed-contours were associated with field identified sunken graves (green dots), only the two outer-most contours were classified. Remaining contours were left ‘unclassified’ (purple lines) and were not used for training and validation. (B) Closed-contours associated with field observation and classified as ‘likely’ despite having less idealized shapes. (C) Closed-contours not associated with field identified sunken graves and classified as ‘unlikely’ (red lines).

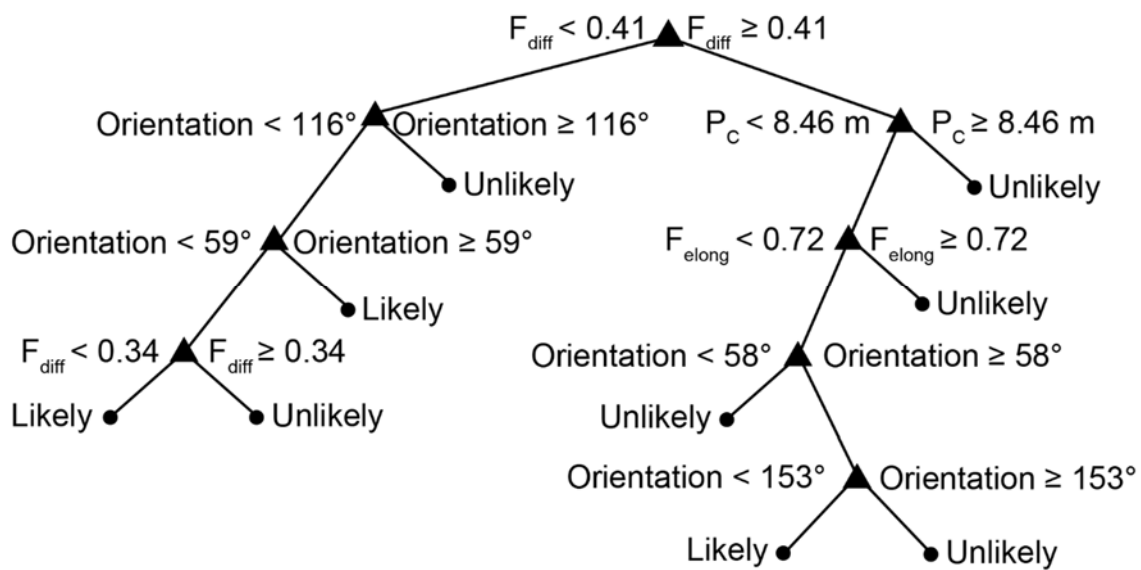


Figure 6. Pruned binary classification tree created from 734 training contours. Predictor selection was determined using the interaction-curvature method. Splitting was determined using Gini's diversity index while pruning used the $1 - SE$ rule. Using a ten-fold cross-validation method, the classification error is 18.05%. Note that not all metrics from *Table 3* are used in this classification tree.

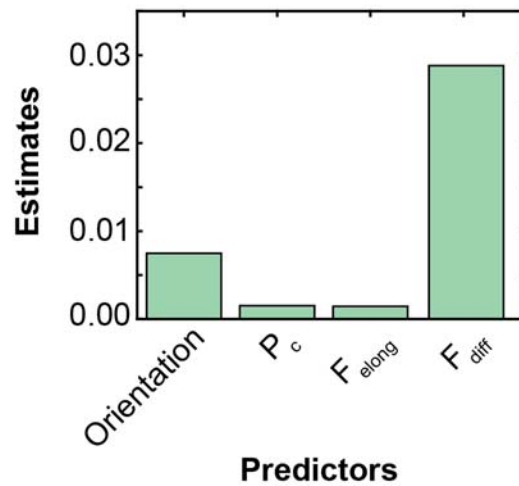


Figure 7. Predictor importance for the pruned classification tree. Of the 13 predictors, only orientation, contour perimeter (P_c), elongation factor (F_{elong}), and difference factor (F_{diff}) were identified as meaningful. The estimated value is calculated by summing the changes in risk due to splits on every predictor and dividing the sum by the number of branch nodes.

Predicted Classification	Likely Sunken Grave	115 (84.6%)	22 (20.2%)
	Unlikely Sunken Grave	21 (15.4%)	87 (79.8%)
		Likely Sunken Grave	Unlikely Sunken Grave
		Manual Classification	

Figure 8. Confusion matrix created from test contours.

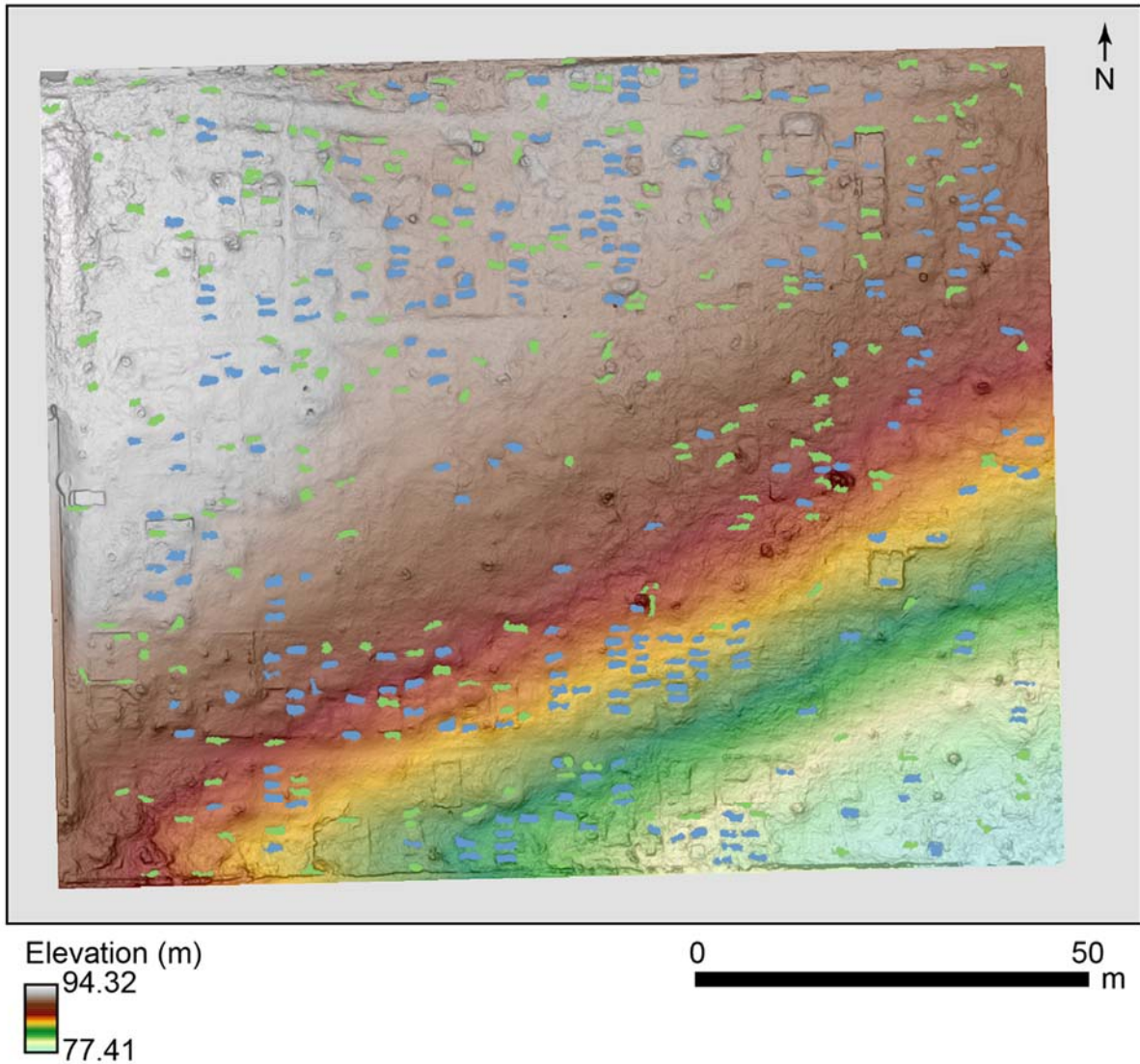


Figure 9. A total of 1,039 contours were classified as ‘likely’ to be associated with sunken graves. Of these, 844 contours spatially collocated with 238 of the graves identified during the pedestrian survey (blue polygons). An additional 305 contours (green polygons), describing 210 features, were identify as ‘likely’ associated with sunken graves based on their morphometric properties. For visualization, overlapping polygons were dissolved into one another.

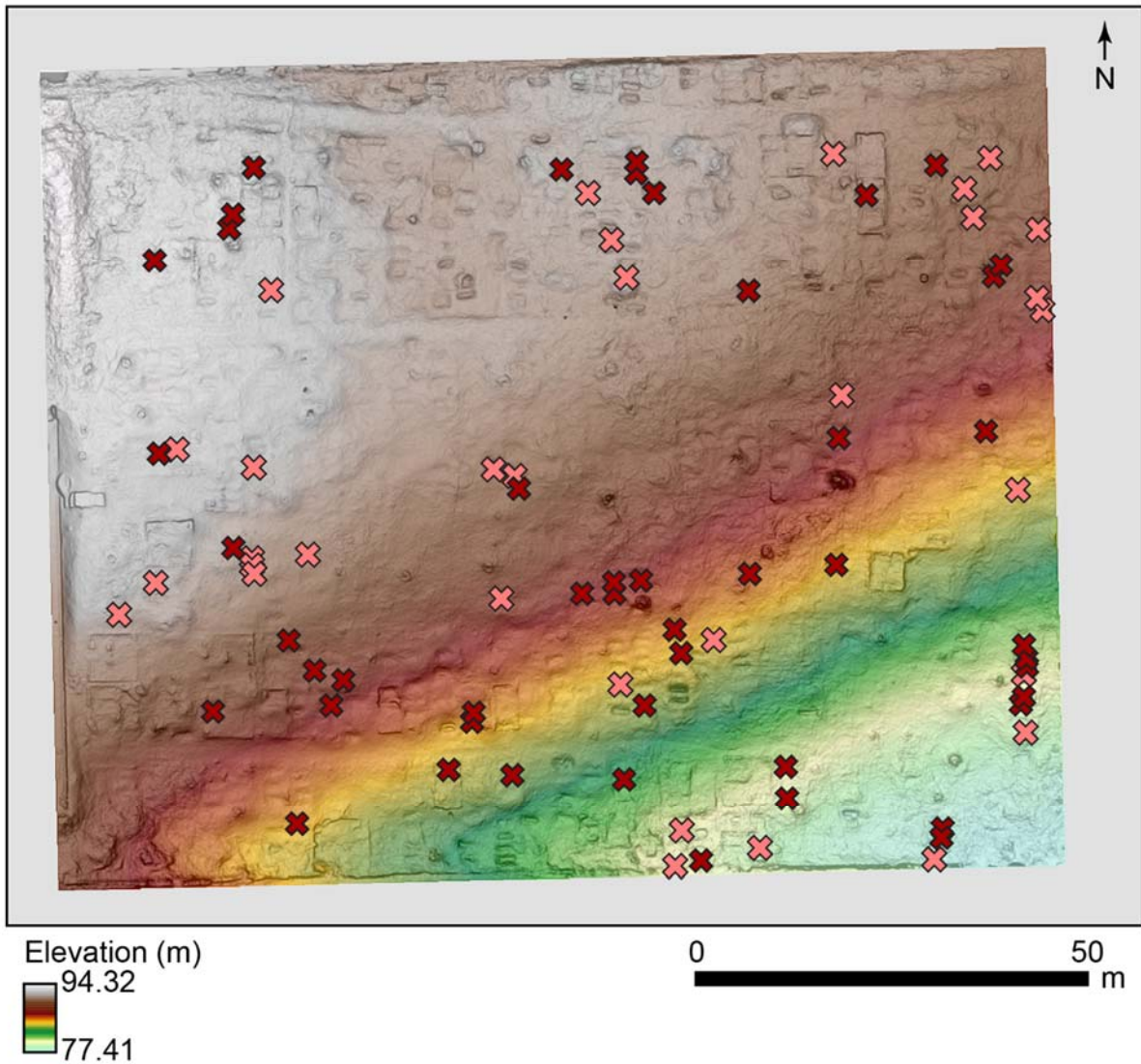


Figure 10. Pink crosses denote the locations of 32 sunken graves whose defining contours had areas outside two standard deviations of field observed sunken graves ($A_{field} < 1.00 \text{ m}^2$; $A_{field} > 2.72 \text{ m}^2$). Red crosses denote the location of 48 field-identified sunken graves with contours that were misclassified by the decision tree.

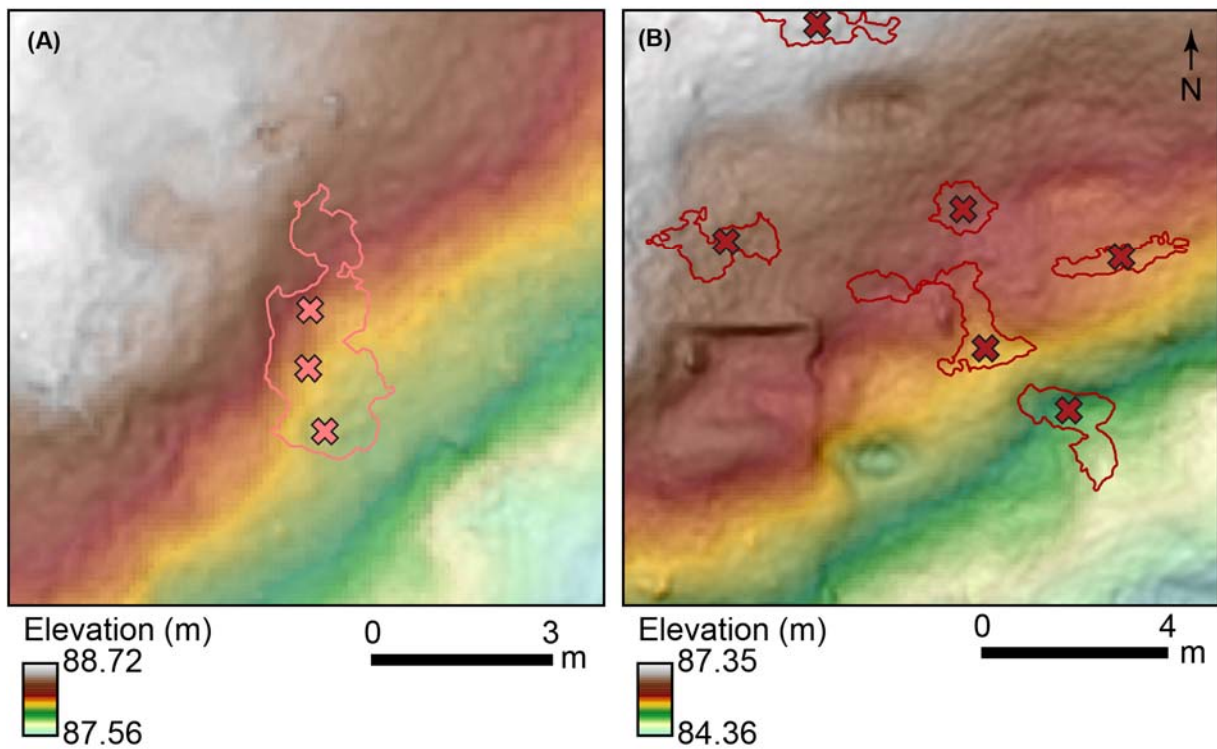


Figure 11. (A) Example of a closed-contour (pink lines, $A_c = 5.42 \text{ m}^2$) that exceeded the area threshold due to graves (pink crosses) coalescing into one another. (B) Examples of graves not identified as ‘likely’ sunken graves (red) by the binary classification tree due to having morphologies that differ substantially from those used as training polygons.

APPENDIX

APPENDIX A

A geospatial and geoarchaeological investigation of an African-American cemetery in

Raleigh, North Carolina, U.S.A.

The contents of Appendix A have been prepared for submission to *Archaeological and Anthropological Sciences* with the following co-authors:

Bohnenstiehl, D. R.¹; Levine, N. S.²; Millhauser, J. K.³; McGill, D. E.³; Wegmann, K.W.¹;
Melomo, V.⁴

¹ Department of Marine, Earth, and Atmospheric Sciences, NC State University, Raleigh, North Carolina, USA

² Department of Geology and Environmental Geosciences, College of Charleston, Charleston, South Carolina, USA

³ Department of Sociology and Anthropology, NC State University, Raleigh, North Carolina, USA

⁴ Department of Anthropology, William Peace University, Raleigh, North Carolina, USA

Abstract

Cemeteries often serve as focal points of identity for a community and can provide insight into its history. Inventorying graves and other cultural features within a historic cemetery can assist with the preservation and management of these sites. Oberlin Cemetery, near downtown Raleigh, North Carolina, U.S.A., was founded in 1873. This 3.2-ac (~13,000 m²) parcel of land served as the main cemetery for the people of Oberlin Village—the largest freedmen’s community in Wake County. Today, decedents of the village founders and other neighborhood residents are working to preserve this community landmark and have its historical significance recognized. In support of these efforts, terrestrial laser scanning and global positioning system enabled pedestrian surveys were conducted during the winter and summer of 2016. This work documented 276 grave makers constructed from carved stone, cement, wood and metal. Of these, 221 are interpreted to be the sole or primary identifier for the burial of one or more individuals. The topography of the cemetery is marked by 357 elongate depressions visible both in the field and contained in the results of laser-scanning data. These are interpreted as sunken graves and occur at 296 sites not associated with burial markers. The ground is also covered with hundreds of fieldstones, some fraction of which may identify additional burials. A ground penetrating radar survey was conducted over ~12% of the cemetery. These observations support the interpretation of the topographic depressions as graves; however, the undulating topography, as well as the density of trees and shrubs, limits the utility of ground-penetrating radar at this site. Based on the inventory of formal grave markers, sunken graves, and fieldstones, the number of individuals interred within the cemetery is estimated to be between 517 and 660. Based on the birth dates listed on monuments, ~23% of these persons were born before the end of the U.S. Civil War (1861-1865). Death dates show steady use of the cemetery

by the community throughout the early 1970's, and less frequent use thereafter, with the most recent burials in 2009. A comparison with a 2012 inventory of monuments within Oberlin Cemetery suggests that ~3% of the markers were lost or displaced in a four-year period. This highlights the importance of preservation efforts and the ongoing need to document cultural materials within historic cemeteries.

Introduction

Historic cemeteries are valuable resources offering insight into the development of neighborhoods over time (Vlach, 1978; Parker Pearson, 1982; McGuire, 1988; Canon, 1989; Little, 1992; Tarlow 1999; Jamieson, 1995). Their preservation typically requires community engagement, and the task of maintaining these sites is often left to local governments and civic groups. In support of landmark applications, as well as educational and outreach initiatives, communities often have worked with academic researchers and contractors to collect base-level information on burial records and catalog the distribution of cultural materials and graves within historic cemeteries (Leibens, 2003; Rainville, 2008; 2009; Gonzales-Tennant, 2016).

Following the American Civil War (1861-1865), African-American cemeteries created during the Reconstruction Era (1865-1877) document the history of an emancipated people as they struggled to build a sense of community. Jim Crow Era (1870's to 1950's) laws further institutionalized racial divisions within the United States and perpetuated the existence of segregated neighborhoods and cemeteries. Over time, despite re-development and shifting demographics within many areas, these cemeteries have remained, and today, they may provide the only visible link to the historic identity of a neighborhood—revealing the civic history, kinship structure, religious practices, and cultural beliefs of its founding residents (Vlach, 1991, Rainville, 2009; Sattenspiel & Stoops, 2010).

This study investigates Oberlin Cemetery (Figure 1), one of four known African-American cemeteries within Raleigh, North Carolina, U.S.A. (Little, 2012). This cemetery, founded in 1873, served the community of Oberlin Village—the largest freedmen's village in Wake County. Although the cemetery fell into disrepair during the late 1900's, a non-profit group, the Friends of Oberlin Village (FOV), is actively working to maintain the grounds, which

serve as a focal point for their efforts to highlight the neighborhood's history. In support of this initiative, pedestrian, terrestrial laser scanning (TLS), and ground penetrating radar (GPR) surveys were conducted to document cultural materials within the cemetery and constrain the number of persons that may be interred there.

Pedestrian, or field-walking surveys catalog and describe cultural materials within a site. The spatial location of these features may be recorded using grids, traditional surveying techniques, or global-positioning system technology (Gaffney, 2008; Newhard et al., 2013). For cemetery investigations, pedestrian surveys have traditionally focused on identification and transcription of headstones in order to ascertain the names, ages, and death dates of those interred, and less commonly on the documentation of fieldstones and other historical artifacts (Rainville, 2009; Amari and Alsulaimani, 2016). The use of digital technology at the field site promotes dynamic, menu-driven data entry that assists in minimizing transcription errors and facilitating rapid archiving (Opitz et al., 2015; Vega and Agulla, 2008).

Terrestrial laser scanners generate a three-dimensional model of the physical environment. These systems use time-of-flight or continuous frequency modulated lasers to measure the distance to surfaces from multiple scan points. In cemetery investigations, TLS has been used principally to record the shape and locations of monuments (Weitman, 2012). Point cloud data can also be gridded to produce high-resolution digital elevation models (DEMs) with sub-decimeter vertical accuracy. Such data are capable of illuminating subtle landscape features that may include sunken graves, walkways, or other markers used to sub-divide a cemetery (Aziz et al., 2016; Majewska, 2017). As the technique typically cannot resolve monument inscriptions, it is most often deployed alongside pedestrian survey efforts.

Ground penetrating radar is a geophysical remote-sensing technique that provides information on the stratigraphy of the shallow (typically < 2-3 m depth) subsurface. A GPR system transmits a pulse of electromagnetic energy that propagates downward into the subsurface and is reflected upward as the wave encounters geologic layers or buried materials with different electrical properties (Conyers, 2004). While the effectiveness of this approach in grave identification depends on local soil conditions and mortuary practices (Gaffney, 2008), this non-invasive technique has become a standard tool in many cemetery investigations and can be critical in delineating burials not accounted for by archival records or formal grave markers (Doolittle and Bellantoni, 2010; Damiata et al., 2013; Kadioglu et al., 2013; Aziz et al., 2016).

In our work at Oberlin Cemetery, data from field investigations and geophysical surveys were spatially enabled within a geographic information system (GIS) to create the first digital maps of the site. These observations were further integrated with georectified historical maps and land records. This archival information tracks the historical change of Oberlin Cemetery and the more modern re-development of properties within the historic Oberlin Village area.

Historical and cartographic analysis

In 1858, Jesse Pettiford, a freed African-American, purchased 16-ac (6.47 ha) of land, which encompassed portions of the future Village of Oberlin, from George W. Moredecai (Wake County, North Carolina, Deed Book 22: 187). Land belonging to Pettiford was identified on an 1865 map of the Confederate lines in Raleigh (War Department, 1865; Figure 2A). It also is depicted, with a reference to the aforementioned deed, on a map of historical properties lines from the mid-1800's that was produced in 1920 by C.L. Mann, a surveyor and Professor of Civil Engineering at North Carolina State University (Mann, 1920; Wake County, 2018; Figure 2B).

Oberlin Cemetery was formally established in July of 1873. Wake County Deeds (40: 445) indicate that Nicholas Pettiford, the son of Jesse Pettiford, sold one-acre (0.4 ha) of land to the trustees of Oberlin Cemetery for forty-five dollars. Although no plat survey of Oberlin Cemetery has been identified from this period, the land was described as located in the Village of Oberlin and bordered by property owned by the late George W. Mordecai on the east, by Albert Pettiford on the south, and by Luvinia Pettiford on the west.

Professor Harry Tucker, a colleague of C.L. Mann's, surveyed the land immediately to the south of Oberlin Cemetery in 1924 (Wake County, North Carolina, Map Book 1924: 81; Figure 3). His map identifies land purchased by John T. Turner from Albert Pettiford in 1920 as the Pine View Cemetery (Wake County, North Carolina, Deed Book 368: 440). Although there is no record of these lands later being formerly recombined by deed, Pine View represents an annex to the main Oberlin Cemetery. Tucker's map shows plans for a total of 136 family plots in four east-west trending rows covering an area of one-acre (0.4 ha).

U.S. Geological Survey (USGS) 15'-topographic quadrangle from 1943 does not show Oberlin Cemetery (Reeves et al., 1943). It also fails to identify the Oberlin Graded School, which at that time was located on the parcel of land to the west of the cemetery. The quadrangle does, however, denote St. Mary's School a short distance away (Figure 4A).

In 1954, J.W. York and R. A. Bryan, local developers, commission a survey of their land between Daniels Street and Wade Avenue. Resulting maps show Oberlin Cemetery as well as identify an access road between the Cemetery and Oberlin Road to the west (Wake County, North Carolina, Map Book 1954: 48). Just two years later, in 1956, The Occidental Insurance Company Building was constructed immediately to the east of the Cemetery, ushering in a new era of development within Oberlin Village (Wake County GIS, 2016).

The 1968 USGS 7.5'-topographic quadrangle (1972 ed.) denotes the presence of the Cemetery and Oberlin Graded School (U.S. Geological Survey, 1968). Aerial photography from the same year (U.S. Geological Survey, 1970; Figure 4B) shows a contiguous wooded area (0.4 ha or 1 ac) encompassing the cemetery and land to north of the Oberlin Graded School. By 1975, however, the Oberlin Graded School was demolished and replaced by a Young Woman's Christian Association (YWCA) facility next to the Cemetery (Wake County GIS, 2016).

In 2003 and 2005, lands immediately to the north of the Oberlin Cemetery were recombined for the construction of the Oberlin Court apartment complex (Wake County, North Carolina, Map Book 2003: 855). Plat maps indicate that only the northern and eastern boundaries of the Cemetery, which abut the Oberlin Court and Occidental properties, were surveyed at this time (Wake County, North Carolina, Map Book 2006: 1744). During construction of the Oberlin Court Apartment complex, parking lot and driveway surfaces were excavated and stone retaining walls up to two-meters in height and fencing were installed along these property lines. Because of commercial development within the formerly wooded area to the northwest, today the 1.31 ha (3.24 ac) Cemetery property can only be accessed from the west through the parking area of the former YWCA building (now owned by InterAct of Wake County).

Previous surveys of Oberlin Cemetery

The first survey of the cemetery was conducted in the 1930's by the Works Progress Administration (WPA), which reported death dates ranging from 1876 to 1913 (Little, 2012). Jennifer Hallman (unpublished) conducted an archival survey in the 1990's, which made use of the WPA survey results and the Wake County Death Registry. Hallman's study also involved interviews with community elders and some field observations; however, no attempt was made

to fully inventory monuments within the cemetery. Her study provided evidence for the burial of 332 individuals between 1876 and 1992 at Oberlin Cemetery.

M. Ruth Little, a local historian, conducted a pedestrian survey of the Cemetery in 2012. Her work was motivated by the formation of the FOV community group the previous year and supported their efforts to have Oberlin Cemetery placed on the City of Raleigh's historic registry. Little's survey established a 10 x 10 ft (3 x 3 m) grid system that was used to reference the position of cultural material within the Cemetery. She produced a tabular database of 147 monuments (primarily burial and family markers) and transcribed the names, dates, and dedications recorded on them.

Field Methods

Terrestrial laser scanning survey

Oberlin Cemetery was surveyed in the winter of 2016 using a Leica HDS3000 terrestrial laser scanner (TLS) deployed at 26 locations throughout the cemetery (Figure 5). A minimum acquisition point spacing of 0.02 m was used. The scan data were tied together into a single, unified point cloud using the Leica Cyclone 9.1.4 software. Tie points were established using the corners of ten monuments, which were surveyed with a Trimble R10 global navigation satellite system (GNSS) receiver with real-time kinematic corrections supplied using a virtual reference station (VRS). As the onboard TLS camera was not functioning during the survey, only three of these tie points could be identified and used for geo-referencing. The resulting RMSE of the survey was 0.80 m. Lidar ground points were classified using LAStools (Isenburg, 2014), with 'wilderness' and 'hyper-fine' flags enabled. Ground-classified points were then thinned and gridded at a spatial resolution of 0.10 m. This grid size resulted in only 14% of cells having ≤ 1 point per cell, while 86% have two or more points per cell. Most of the sub-optimally

constrained pixels were at the edges and within densely vegetated areas. Topographic expressions of family plots were digitized at a 1:250 scale.

Pedestrian survey

Pedestrian survey data were recorded in the field during summer 2016 using a Trimble R10 GNSS-VRS receiver. Data collection utilized a custom-build digital form that provided adaptive menu choices and data entry fields. The form was developed using the Trimble TerraFlex application programming interface (Figure 6), which was communicated with the R10 receiver using a Bluetooth connection. Positional information was recorded at the southwestern corner of each feature. Horizontal accuracy ranged between 0.01 to 2.93 m, with a mean of 0.15 m and standard deviation of 0.24 m.

Items of material culture were organized by categories: (1) *Carved Stones* (Figure 7A), including worked and engraved headstones, footstones, and obelisks; (2) *Cement Markers* (Figure 7B) that were cast or poured stone conglomerates used as headstones and footstones; (3) *Fieldstones* (Figure 7C), consisting of local schist and large quartz crystals which were predominate markers from the Colonial period through the 1870's (Alexia, 1997; Rainville, 2008; Stone, 2009); (4) *Metal Plaques* (Figure 7D) made by casting or pressing metal as well as pressed metal frames all generally associated with a unique metal steak form; (5) *Wooden headboards* (Figure 7E); and (6) *Other* (Figure 7F) which included items such as conch shells, drain pipes and metal scrap. A photograph was captured for each feature and its dimensions recorded. The names, dates, and dedications were transcribed for carved stones, cement markers, and metal plaques.

The Cemetery landscape is marked by numerous elongate topographic depressions, with morphologies that are consistent with subsidence associated with graves (Aziz et al., 2016). The

dimensions of each depression, as visible within the field, were recorded using a tape measure. To facilitate later comparisons with the TLS data, no attempt was made to remove leaf litter and vegetation prior to making these measurements.

Tables were generated containing attributes that could be queried to summarize the data by record class (monument, monument & sunken grave, and sunken grave), material, inscriptions, and state of disrepair. Field notes, transcribed names, photographs, topographic data, and geospatial relationships were used to associate primary (e.g., headstone) and secondary (e.g., footstone) monuments with unique burials. Metal plaques without names, wooden headboards, and heavily weathered carved stone were associated with burials based on their continuity of form with other monuments within the Cemetery.

Ground penetrating radar survey

A GPR survey was carried out over ~12% of the cemetery (Figure 8) with the objectives of validating our interpretation of closed topographic depressions as sunken graves and potentially locating unmarked graves. A more extensive GPR survey was judged to be impractical due to the undulating terrain and prevalence of trees and shrubs across large portions of the site. Both 250 and 500 MHz Sensors and Software Pulse EKKO Pro radar antennae were deployed using a cart system. Survey lines were collected in a roughly north-south (grave-normal) direction with 0.5 m spacing between lines. Trace data were stacked 16 times and triggered at 0.05 (250 MHz) and 0.02 m (500 MHz) intervals along each line. An average radar velocity of 0.1 m ns^{-1} was estimated by fitting hyperbola throughout the survey area. The maximum depth of penetration for the radar was ~2.5-3.0 m.

Results

Cultural materials and burials

The pedestrian survey generated 1087 records (Table 1) within the cemetery. This includes 276 grave markers (headstones and footstones) constructed from carved stone (n = 160), poured cement (n = 67), metal plaques (n = 47), and wooden headboards (n = 2). Nearly half (n = 126) of these markers were in some form of disrepair (i.e., broken, fallen, sunken, rusted). A further 234 records list other objects of material culture (e.g. flower holders, terra cotta pots, cinderblocks). Of the 276 markers and 234 other items, 221 were interpreted as the sole or primary marker for the burial of one or more persons (Table 2). Classification as a primary burial marker was determined by the inscription of names (n = 132) or other identifiers (n = 4), the association of an uninscribed monument with sunken grave (n = 29) or based on the continuity of a monument's form (e.g., a metal plaque, wooden headboard, heavily weathered carved stone with no discernable markings) (n = 56). Other items of material culture identifying unique burials are itemized in Appendix A.1. A total of 158 individuals (Appendix A.2) are identified from 137 records. Mattie E. Williams was identified by two monuments with different birth dates. Some monuments identify more than one person.

Prior research has indicated that fieldstones—unworked or minimally worked rocks lacking inscriptions—were used as burial markers throughout the southeastern United States during the 17th to 19th centuries (Alexia et al., 1997; Brandon and Hillard, 1998; Rainville, 2008; Stone, 2009). A total of 272 fieldstones were surveyed at Oberlin Cemetery. Of these, 13 were spatially associated with sunken depressions, consistent with their being interpreted as burial markers, and an additional 130 might be considered unique grave markers based on their location within rows and upright positioning (143 total). Some remaining fieldstones appear to delineate

family plots, while others are arranged more haphazardly, making their function within the cemetery less clear.

Based on their size and morphology, 357 topographic depressions were identified in the field as possible sunken graves. The length, depth, and widths of each sunken depression are summarized in Table 3. Of these records, 61 were associated with monuments including carved stones (n = 16), cement markers (n = 8), metal plaques (n = 15), fieldstones (n = 13), and other items of material culture (n = 9). The remaining 296 depressions were not associated with grave markers. Comparison of these field observations with TLS data showed that ~89% (n = 318) could be identified visually in the hill-shaded elevation dataset.

The formation of sunken graves is driven primarily by sediment compaction, with much of the settling occurring in initial month-to-years after a burial (Scott, 1980), and the later collapse of caskets within the subsurface. The occurrence of a sunken grave therefore depends on the leveling and maintenance of the site over time, as well as the construction materials of the casket and vault (if present). The infrequent occurrence (~10%) of sunken graves in association with burials having carved headstones is consistent with the upkeep of these gravesites over time and perhaps the use of casket materials with greater longevity. The Oberlin Cemetery site is comprised of clay rich (*Cecil series*) soils developed over the igneous and metamorphic rock of the Appalachian Piedmont. Local soil hydrologic conditions may also influence the rate and amount of settling, and the prevalence of casket collapse. After heavy rain events, water commonly pools along the southern (lowest elevation) margin of the Cemetery, where many of the deepest depressions were found (Figure 9). We cannot, however, account for spatial variations in the age of these burials or differences in mortuary practices.

Based on the pedestrian survey results, Oberlin Cemetery contains 221 primary burial markers, which list the names or initials of 158 individuals (Appendix A.2). There are also 296 sunken gravesites that cannot be associated with a formal grave marking monument or fieldstone. This conservatively constrains the total number of interred individuals to be 517. We identify a total of 143 fieldstones positioned in a manner consistent with use as a burial marker. We therefore estimate a maximum of 660 individuals buried within Oberlin Cemetery.

Enclosures and family plots

Twenty-seven enclosures were identified both from the pedestrian survey and analysis of hill-shaded elevation data (Figure 10) with 0 to 21 records within each (Appendix A.3). The Dunston family plot, located just inside the cemetery entrance, is outlined by worked stone pillars connected with linked chain and contains a tall (~ 2.5 m) obelisk monument. Similarly, the Turner family plot, located at the entrance of Pineview Annex, is surrounded by a short iron fence with stone corners, contains a marble bench, and large graded monuments. The ornamental characteristics of these two enclosures may denote the socio-economic standing of the families within the community. Not all family enclosures, however, are as ornate. Some additional family plots (n = 6) are marked by a family monument and lack a walled or fenced enclosure.

Enclosures do not always contain a single-family name. In three cases, more than one family name is listed on grave markers within an enclosure that contain a family monument. A further five enclosures have multiple family names listed on grave markers, but do not contain clear family monuments. Within these enclosures with multiple family names, the Peebles family is identified in two enclosures and Curtis/Curties in three. The presence of conch shells in the Webb family plot hint at a sense of cultural ties with west African culture (Jamieson, 1995); however, these are only present within this family plot.

Demography

There were 158 individuals identified by monument inscriptions, including five persons identify only by their family name and three persons identified only by their initials (Appendix A.3). A total of 128 birth dates and 142 death dates were transcribed. In a handful of cases, the inscriptions on monuments could not be read with confidence due to weathering, or it could not be determined if a date referenced the birth or death of an individual. One individual, Mattie E. Williams, appears to be identified on two monuments, with slightly different (January 22 vs. February 22) death dates in 1894.

The distribution of birthdates within Oberlin Cemetery is left-skewed (Figure 11A) and shows that ~23% of those individuals having inscribed monuments were born before the end of the American Civil War (ca. 1865). The oldest birthdate inscribed on a monument was for Zylphia Thompson, born in 1804. The most recent birthdate recorded was for Henry Jose C. Peebles, born December 6, 1962.

The oldest burial with a legible inscription on a monument dates to 1876, consistent with the WPA and Hallman survey results. The median year of burial was 1937, and the cemetery was used regularly through the early 1970's (Figure 11B). The rate of burials decreased during the 1980's and 1990's, as the site Cemetery grounds fell into a state of disrepair. Eight individuals, however, have been buried in Oberlin Cemetery since the year 2000, with Grace H. Williams (2009) being the individual interred most recently.

Based on monument inscriptions, the average age of individuals at the time of death was 57 years, with a median age of 62 years. The youngest individuals identified were John Scarver (1 day) and Ophelia Sheppard (11 months). Charles H. Hunter (102 years) and Carrie W. Hunter

(107) were the oldest individuals. Figure 12 shows a box-and-whisker plot for the age at death within the Cemetery binned by birth year.

Local historians have contended that the oldest part of the cemetery is along the central western edge, noting a clustering of fieldstone markers in this area. Our pedestrian survey, however, shows that these markers are ubiquitously distributed throughout the cemetery. Death dates on inscribed monuments similarly show no spatial patterning, beyond the more recent (after 2000) burials, which are clearly concentrated in the southwestern corner of the cemetery (Figure 13). This lack of patterning by date is consistent with burials being organized primarily around familial organization. Graves for Oliffe Poole and Lula Turner, located along the northern edge of Pineview Annex, have death dates prior to its 1920 creation.

Religious symbols are exclusively Christian and include engraved crosses. Lamb of God sculptures top two tombstones associated with children. Carvings of ivy leaves and anchors are also common throughout the cemetery. Five military veterans are buried within the cemetery—one Spanish-American War and four World War I. Notation of occupation includes a caduceus for William B. Pettiford and John V. Turner’s monument noting him as an educator. There are six monuments displaying the Masonic Square and Compass of the Freemasons (Figure 14A); five monuments with three interlocking chains denoting membership in the Ancient Order of Oddfellows (Figure 14B), as well as one inscription referencing the Eastern Star Lodge (Figure 14C).

Discussion

Database comparison

Prior work carried out in 2012 for the City of Raleigh Landmark (CRL) survey generated a total of 147 records (Little, 2012). Approximately 86% (n = 127) of these records could be

positively identified within the database generated by the 2016 pedestrian survey, including grave markers with (n = 114) and without (n = 2) names, as well as family monuments (n = 11). During the pedestrian survey, location information was recorded utilizing a high-resolution GNSS-VRS receiver; however, the CRL survey recorded only the grid (10 x 10 ft) in which each record existed. Given the written descriptions and ambiguity in location provided by the CRL survey, 15 records could not be positively correlated with the pedestrian survey database. An additional five CRL survey records (headstones), however, are clearly absent within the pedestrian survey database. Subsequent efforts, which enlisted local community members, have failed to locate these headstones, suggesting that they have been damaged or displaced during the interval between the two surveys. This represents a ~3% loss over a four-year period.

The CRL survey created a registry of 138 people buried in Oberlin Cemetery; whereas, this pedestrian survey identified 158 individuals—representing a 15% registry increase. Both surveys record the earliest burial being that of Julia Andrews in 1876. Although the CRL survey reports use of the cemetery through only 1971, our pedestrian survey identifies 19 later burials, with the most recent being those of Grace H. and Alexander Williams, in 2009. In total, the pedestrian survey identified 25 individuals and three family monuments not present within the CRL survey database.

Unmarked grave identification

Where burials are suspected to be present, but no grave markers exist, GPR has been used by other studies to confirm their presence (Johnson, 2010; Doolittle and Bellantoni, 2010; Damiata et al., 2013; Kadioglu et al., 2013; Aziz et al., 2016). Despite clay-rich (conductive) soils within Oberlin Cemetery, the 2.5-3.0 m depth-of-penetration for the radar was sufficient for imaging the burials at this site (Figure 15A). The vegetation cover on site, however, made a

detailed scan (≤ 0.5 m line spacing) of the entire area impractical. Moreover, our partial (~12%) survey of the cemetery with GPR revealed a tendency for the radar system to decouple while crossing many of the sunken graves. This situation results from a change in the height of the antennas above the ground surface, as well as the thick accumulation of leaf-litter present within some topographic depressions. While indications of a burial can often be gleaned from these radargram images, this change in radar coupling make interpretation more difficult and generally renders depth slicing ineffective (e.g., Conyers et al., 2014).

As an alternative approach, this study has relied on the prevalence of sunken graves to constrain the minimum number of unmarked burials within Oberlin Cemetery. The topographic expression of these sunken graves was identified in the field during the pedestrian survey and are visualized using the lidar-derived elevation model (Figure 15B, C). The identification of these features within topographic data is consistent with observations by Weitman (2012) and Aziz et al. (2012). Given the consistency of these observations and the impracticality for cemetery-wide GPR survey, unmarked burials within similar conditions would be best inventoried using their topographic signal.

Summary and conclusions

Pedestrian survey and terrestrial laser scanning datasets collected in 2016 provide baseline information for the preservation and management of Oberlin Cemetery, in Raleigh, North Carolina, U.S.A. This cemetery, which was founded in 1873, served the historic African-American community of Oberlin Village—the largest Freedman’s community in Wake County (Little, 2012). Today, with continued land-development and shifting demographics within the neighborhood, the cemetery serves as a focal point for community efforts to preserve the area’s history.

The pedestrian survey documented 276 burial markers constructed from carved stone, cement, wood, and metal; of these, 221 are interpreted to be the sole or primary identifier for the burial of one or more individuals. Burial markers record the names or initials of 158 individuals, with ~23% of these persons being born before the end of the U.S. Civil War in 1865. The cemetery remained in steady use by the community throughout the early 1970's, with less frequent use thereafter, and the most recent burials were in 2009.

In addition to these formal grave markers, the survey recorded 272 unworked or minimally worked fieldstones, which were common grave markers in use throughout the southeastern US through the 19th century (Alexia, 1997; Rainville, 2008; Stone, 2009). Based on their alignment, positioning, or association with a sunken grave, as many as 143 of these fieldstones could represent grave markers. The pedestrian survey also cataloged 357 elongate topographic depressions that are interpreted to have formed in response to the subsidence of a gravesite or following the collapse of a casket in the subsurface. Of these small depressions, 296 occur at sites not otherwise marked by formal burial markers. Summing unique observations, the number of persons interred within the cemetery is estimated to be between 517 (formal burial markers and sunken graves) and 660 (formal burial markers, sunken graves, and fieldstones).

Many burials are organized within family plots. There is a total of 27 walled or fenced enclosures within the cemetery, of which seven contain family markers. In addition, there are six unenclosed family plots identified based on the presence of a family marker and corroboration with the CRL. Freemason and Ancient Order of Oddfellows iconography are found on a handful of headstones. Religious symbols that adorn monuments within the Cemetery are exclusively of Christian origin.

Comparing the results of a 2012 grid-based inventory (cf. Little, 2012), the 2016 pedestrian survey identified 25 individuals not listed as part of the City of Raleigh Landmark application—expanding the cemetery registry by 15%. The survey, however, failed to identify five headstones (~3%) located in 2012. This suggests that these monuments have been displaced or severely damaged over the intervening four-year period and highlights the need to actively document cultural materials within historic cemeteries and the importance of sustained preservation efforts.

Acknowledgements

We would like to thank the Friends of Oberlin Village and InterAct for facilitating access to the Cemetery. Wake Technical Community College students Natalia Womack, Lisa Picariello, and Morgan Whited without whom the field survey likely never would have happen. The Santee Cooper Geographic Information Systems Laboratory for providing the Leica HDS 3000. Justin Barton for his help while carrying out the lidar scanning and referencing the data as well as providing Cyclone licenses. Kevin Walker, Heather Paxson, Andy Jordan, and Jeff Weis for assisting in the field. Meg Watters for discussions regarding GPR survey. Jim Newhard for information regarding landscape archaeology theory and methods. Student participation in this project was support by the National Science Foundation as part of a partnership between the Department of Marine, Earth, and Atmospheric Sciences at N.C. State University and Wake Technical Community College.

References

1. Amari IEA, Alsulaimani GS. Detecting and Imaging Historical Graves by Using Visual Inspection and Ground Penetrating Radar Investigation Detecting and Imaging Historical Graves by Using Visual Inspection and Ground Penetrating Radar Investigation. *Int J Res Eng Sci.* 2016;4(10):1-9.

2. Aziz AS, Stewart RR, Green SL, Flores JB. Locating and characterizing burials using 3D ground-penetrating radar (GPR) and terrestrial laser scanning (TLS) at the historic Mueschke Cemetery, Houston, Texas. *J Archaeol Sci Reports*. 2016;8:392-405. doi:10.1016/j.jasrep.2016.06.035.
3. Brandon JC, Hilliard JE. The Van Winkle Mill and the Anderson Slave Cemetery : African-American Related Sites in Northwest Arkansas. *African Diaspora Archaeol Newsl*. 1998;5(3):3-6. <http://scholarworks.umass.edu/adan/vol5/iss3/1>.
4. Cannon A. The Historical Dimension in Mortuary Expressions of Status and Sentiment. *Curr Anthropol*. 1989;30(4):437-458. <http://www.jstor.org/stable/2743373>.
5. Conyers LB. *Interpreting Ground-Penetrating Radar for Archaeology*. New York, NY: Routledge; 2014.
6. Damiata BN, Steinberg JM, Bolender DJ, Zoëga G. Imaging skeletal remains with ground-penetrating radar: Comparative results over two graves from Viking Age and Medieval churchyards on the Stóra-Seyla farm, northern Iceland. *J Archaeol Sci*. 2013;40(1):268-278. doi:10.1016/j.jas.2012.06.031.
7. Doolittle JA, Bellantoni NF. The search for graves with ground-penetrating radar in Connecticut. *J Archaeol Sci*. 2010;37(5):941-949. doi:10.1016/j.jas.2009.11.027.
8. Gaffney C. Detecting trends in the prediction of the buried past: A review of geophysical techniques in archaeology. *Archaeometry*. 2008;50(2):313-336. doi:10.1111/j.1475-4754.2008.00388.x.
9. González-Tennant E. Recent Directions and Future Developments in Geographic Information Systems for Historical Archaeology. *Hist Archaeol*. 2016;50(3):24-49. doi:10.1007/BF03377332.
10. Helsley AJ. *Silent Cities: Cemeteries and Classrooms*. South Carolina Department of Archives and History; 1997.
11. Jamieson RW. Material Culture and Social Death : African-American Burial Practices. *Hist Archaeol*. 1995;29(4):39-58. <http://www.jstor.org/stable/25616423>.
12. Kadioglu S, Kadioglu M, Kadioglu YK. Identifying of buried archaeological remains with ground penetrating radar, polarized microscope and confocal Raman spectroscopy methods in ancient city of Nysa, Aydin - Turkey. *J Archaeol Sci*. 2013;40(10):3569-3583. doi:10.1016/j.jas.2013.04.001.
13. Liebens J. Map and Database Construction for an Historic Cemetery: Methods and Applications. *Hist Archaeol*. 2003;37(4):56-68. <http://www.jstor.org/stable/25617095>.
14. Little MR. *Oberlin Cemetery Landmark Designation Application*. Raleigh, N.C.; 2012.

15. Majewska A. Surface prospection of burial grounds and new research tools (on the example of the study of changes in cemetery boundaries). *J Geogr Polit Soc.* 2017;1/2017(1):60-69. doi:10.4467/24512249JG.17.008.6207.
16. Mann CL. Part of Mordecai-Cameron Lands: as compiled from recent surveys, deed survey notes and original survey notes. [http://www.wakegov.com/rod/help/land/Pages/Historical Maps/CLmaps.aspx](http://www.wakegov.com/rod/help/land/Pages/Historical%20Maps/CLmaps.aspx). Published 1920. Accessed January 10, 2018.
17. McGuire R. Dialogues with the dead: Ideology and the Cemetery. In: *The Recovery of Meaning: Historical Archaeology in the Eastern United States.* ; 1988:435-480.
18. Newhard JML, Levine NS, Phebus AD, Craft S, John D. A geoinformatic approach to the collection of archaeological survey data. *Cartogr Geogr Inf Sci.* 2013;40(1):3-17. doi:10.1080/15230406.2013.762139.
19. Opitz R, Limp WF. Recent Developments in High-Density Survey and Measurement (HDSM) for Archaeology: Implications for Practice and Theory. *Annu Rev Anthropol.* 2015;44(1):347-364. doi:10.1146/annurev-anthro-102214-013845.
20. Rainville L. Social Memory and Plantation Burial Grounds, a Virginian Example. *Africa Diaspora Archaeol Newsl.* 2008;11(1). <http://scholarworks.umass.edu/adan/vol11/iss1/5>.
21. Rainville L. Protecting Our Shared Heritage in African-American Cemeteries. *J F Archaeol.* 2009;34(2):196-206. doi:10.1179/009346909791071005.
22. Reeves R, Drown CH, Hopkins BT, Pumpelly JW, Jones JM. *Topographic Map of Raleigh, N.C.: The Geological Survey, Map N3545--W7830/15, One GeoTIFF File, Scale 1:62,500.* 1943rd ed.; 1943. <https://ngmdb.usgs.gov/topoview/viewer/#15/35.7960/-78.6657>.
23. Sattenspiel L, Stoops M. Gleaning signals about the past from cemetery data. *Am J Phys Anthropol.* 2010;142(1):7-21. doi:10.1002/ajpa.21186.
24. Scott CR. *An Introduction to Soil Mechanics and Foundations.* Third. Barking, England: Applied Science Publishers Ltd.; 1980.
25. Stone G. Sacred Landscapes : Material Evidence of Ideological and Ethnic Choice in Long Island , New York , Gravestones , 1680-1800. *Hist Archaeol.* 2009;43(1):142-159. <http://www.jstor.org/stable/25617547>.
26. Tarlow SW. *Bereavement and Commemoration: An Archaeology of Mortality.* Oxford: Blackwell; 1999.

27. U.S. Geological Survey. *Aerial Single Frame Photo ID: 1VBWH00010033*. Sioux Falls, South Dakota: U.S. Geological Survey (USGS) Earth Resources Observation and Science (EROS) Center; 1970. https://lta.cr.usgs.gov/Single_Frame_Records.
28. Vega SG De, Agulla SO. Using mobile GIS for Field Digital Data Acquisition (FDA) in archaeological field survey. *Geoinf Technol Geo-cultural Landscapes Eur Perspect*. 2008;35:35-46.
29. Vlach JM. *The Afro-American Tradition in Decorative Arts*. University of Georgia Press; 1978.
30. Vlach JM. *By the Work of Their Hands: Studies in Afro-American Folklife*. University of Virginia Press; 1991.
31. Wake County NC. Map Book. <http://services.wakegov.com/booksweb/genextsearch.aspx>. Published 2016. Accessed December 18, 2017.
32. Wake County NC. Deed Book. <http://services.wakegov.com/booksweb/genextsearch.aspx>. Published 2016. Accessed December 17, 2017.
33. Wake County NC. C.L. Mann & Tax Maps. [http://www.wakegov.com/rod/help/land/Pages/Historical Maps/CLmaps.aspx](http://www.wakegov.com/rod/help/land/Pages/Historical%20Maps/CLmaps.aspx). Published 2018. Accessed January 10, 2018.
34. War Department. Office of the Chief of Engineers. 1818-9/18/1947. Map of the Rebel Lines at Raleigh, N.C., Evacuated April 13th, 1865, upon the approach of the Army commanded by Maj. Gen. W. T. Sherman, U.S.A. Reduced under the direction of Capt. O. M. Poe, Corps of Engineers, Bvt. Brig. Gen., U.S.A. & Chief Engineer, M. <https://catalog.archives.gov/id/305783>. Published 1865. Accessed January 10, 2018.
35. Weitman SL. Using Archaeological Methods in Cemetery Surveys with Emphasis on the Application of Lidar. *Electron Theses Diss*. 2012:627. <http://digitalcommons.georgiasouthern.edu/cgi/viewcontent.cgi?article=1627&context=etd>

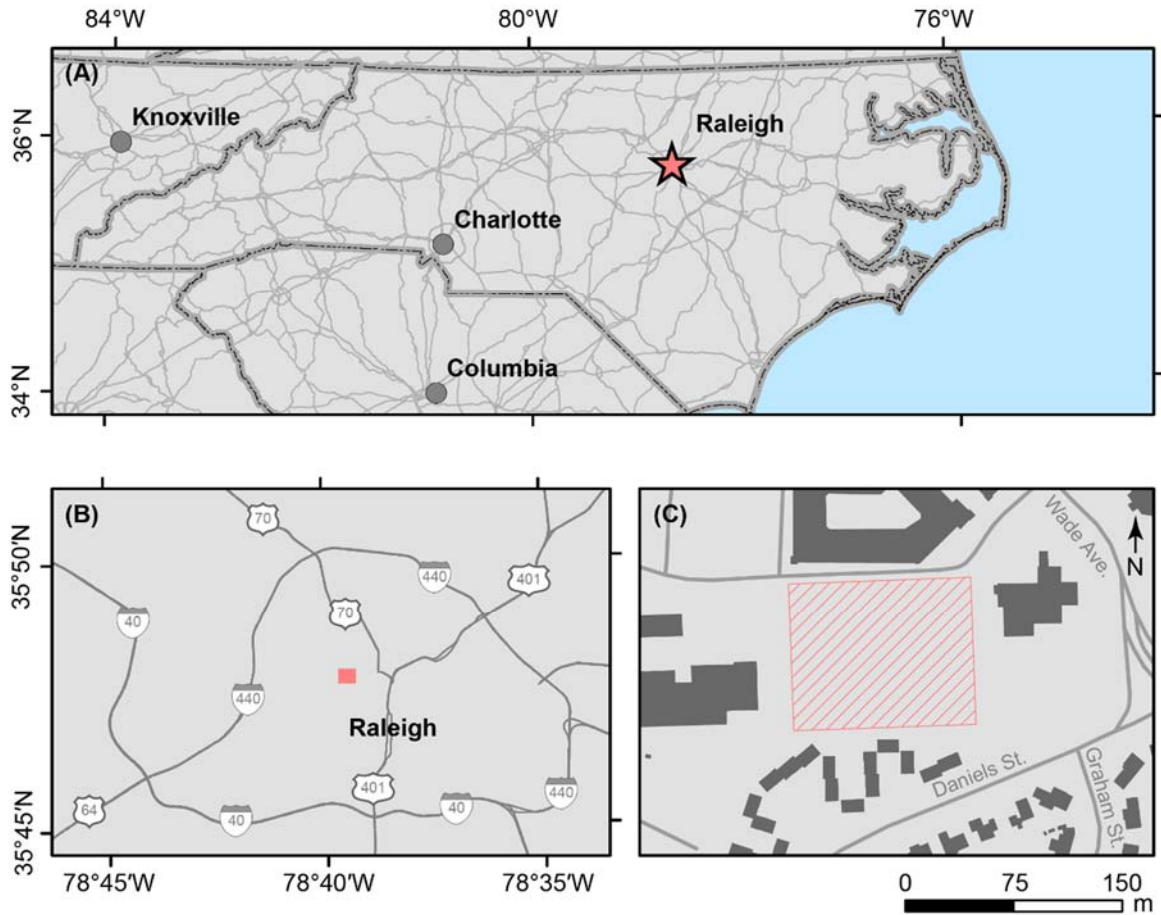


Figure 1. (A) Raleigh is located in central North Carolina. (B) Just north-west of downtown Raleigh, Oberlin Cemetery (pink square) occupies a 3.2-acre (1.3-hectare) plot of land. (C) To the north of the cemetery (pink hachured square) are the Oberlin Court Apartments while to the south are the Cameron Village Condominiums. Flanking the cemetery to the east and west are the Occidental Life Insurance and InterAct office buildings, respectively.

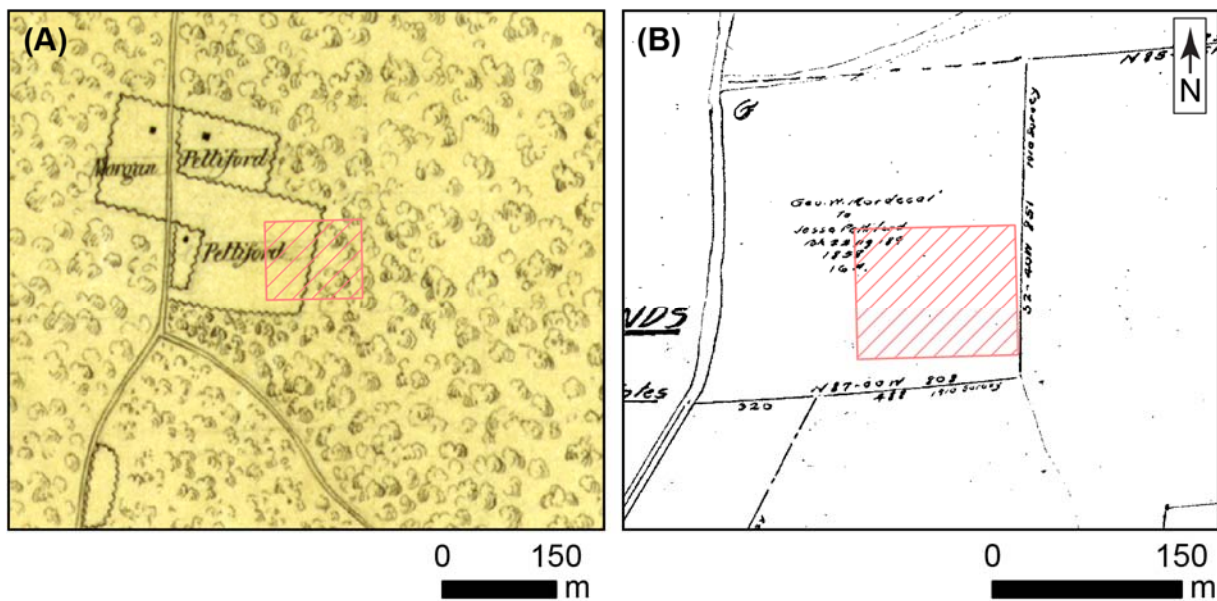
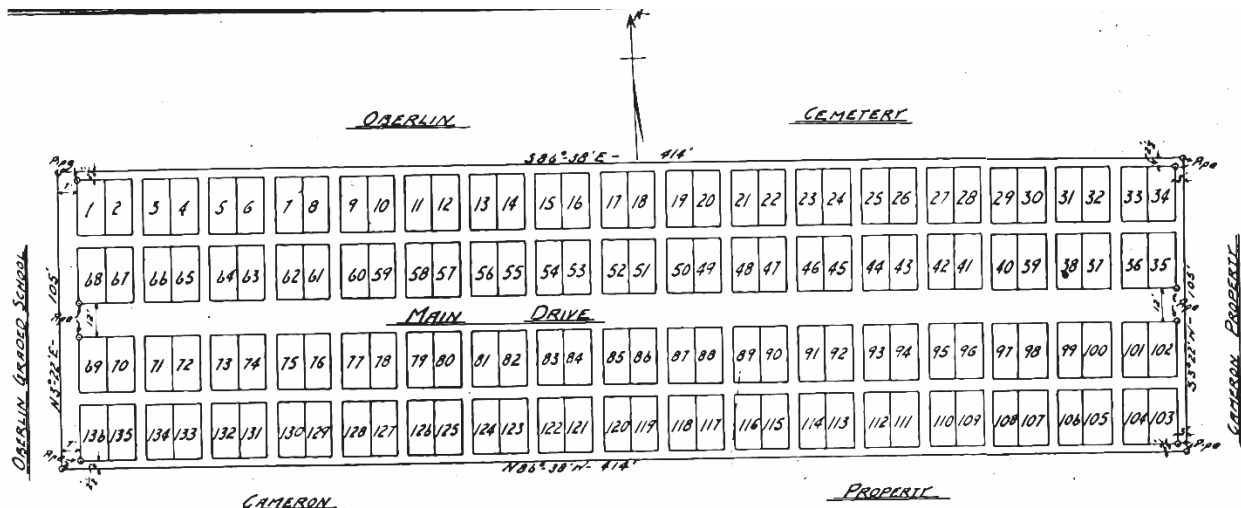


Figure 2. Modern extent of Oberlin Cemetery (pink hatched polygon) compared to two historic maps. (A) The modern extent occupies land identified as Pettiford's in an 1865 map of Confederate lines around Raleigh, North Carolina. (B) A map created in 1920 by C.L. Mann from compiled survey, deed survey notes, and historic surveys indicating that the land was sold by George W. Mordecai to Jesse Pettiford in 1858. The boundary for Pettiford's land is noted on Mann's map as being re-surveyed in 1910.



NOTE:-
 All Lots are 10' x 20'
 Walks are 4' wide except as noted

PINE VIEW CEMETERY
RALEIGH, N.C.
 Scaled 1:20 Surveyed & Plotted by
 June, 1922 Harry Tucker
 Civ. Eng.

Figure 3. A survey plat map created by Harry Tucker of Pine View Cemetery which was created by John Jerome Turner in 1922. Pine View abutted Oberlin Cemetery to the south and is now collectively identified as part of Oberlin Cemetery, although sometimes identified as an annex. The plat indicates the annex contains 136 lots, or family plots, measuring 18.58 m² (200 ft²), each.

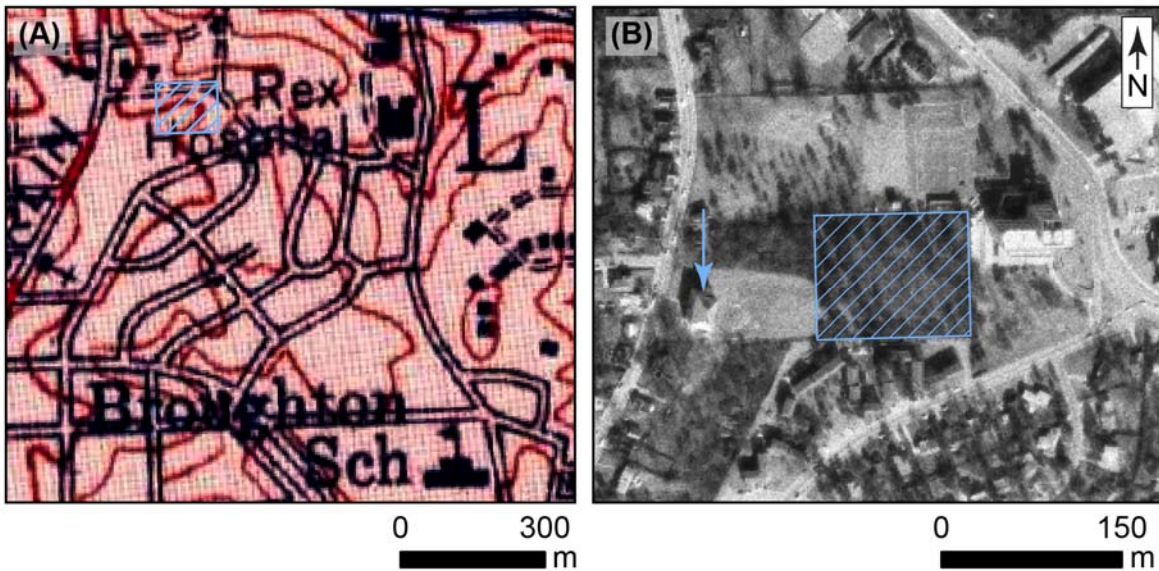


Figure 4. Modern extent of Oberlin Cemetery (light blue hatched polygon) compared to United States Geological Survey (USGS) (A) topographic data and (B) aerial photography. The 15'-topographic map from 1943 does not show Oberlin Cemetery nor Oberlin Graded School but does show the historically white Broughton High School a short distance away. Aerial photography from 1968 shows Oberlin Graded School (below blue arrow) immediately to the west of the Cemetery. The Cemetery is wooded with a contiguous wooded appendage extending west from the northwestern corner. Although the land-cover between the appendage and cemetery are the same, the land-use is indeterminate.

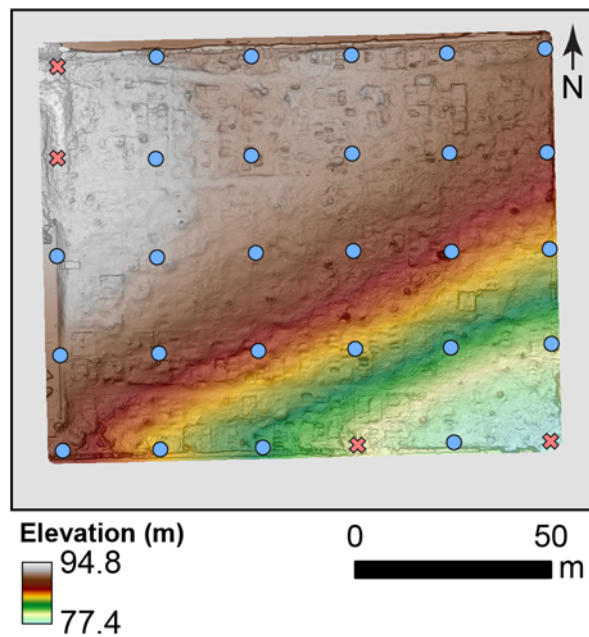


Figure 5. Locations for 26 scans (blue dots) carried out with a Leica HDS3000 Terrestrial Laser Scanner within Oberlin Cemetery. These scans were combined into a unified point cloud within Leica Cyclone. Color-shading shows the derived digital elevation model created from these data. Planned scans at four locations (pink crosses) could not be conducted due to dense vegetation.

Trimble TerraFlex™

2 Projects
1 Tasks
990 Forms
Collect

Oberlin Cemetery

FieldValidation
0 / 990 forms updated

Forms | Map

Cemetery Boundary | Geodetic Posts
GPR Point | More

POINT
21 m ORIGINAL

Marker ID *
OC1088

Date Recorded
06 June 2016

Photos

What are you recording? *
Monument (only)

MONUMENT DESCRIPTION

Is the monument a grave marker? *
 Yes No

...what is the monument?

Monument material
Carved headstone

Monument Shape Description
Rectangular

What kind of marker is it?
Footstone

Monument Height (cm)
9 cm

Monument Width (cm)
10 cm

Monument Depth (cm)
5.5 cm

Monument Damage (description)
None

Transcribe writing on monument
T. B.

Dates on monument
None

Names on monument
T. B.

Symbols on monument
None

GRAVE DESCRIPTION

Not Applicable

Why are you documenting this feature?

ENCLOSURE DESCRIPTION

Is the grave part of an enclosed area?
 Yes No

What is the enclosure made out of?
Stone

List the ID's of graves within the same enclosure
OC1083, OC1084, OC1085, OC1086, OC1087, OC1088

Further comments

Initials
JW

AUTO COLLECTED COMPONENTS

Figure 6. A customized data entry form was created for the work at Oberlin Cemetery using Trimble’s TerraFlex application. Point and polygon data could be recorded with each point having an associated estimated accuracy with it. A unique identification number was given to each marker along with date and time stamp and field photos. Subsequent fields were dynamically exposed depending on prior values entered by the user. Shown here are fields exposed based on answering “Monument (only)” for the question “What are you recording?” Beyond recording metrics and inscriptions, if present, spatial relationships were also recorded, such as existing in an enclosure or other associated markers. Finally, the person recording the marker had to sign their initials to close the form.



Figure 7. Items of material culture identified within the cemetery were grouped into (A) Carved Stones, (B) Cement Markers, (C) Fieldstones, (D) Metal Plaques, (E) Wooden headboards, and (F) Other. Other was a catch-all term for any material culture that did not fit neatly into the other five categories. Features shown with a graduated scale in 1, 2, 5, and 10-centimeter intervals.

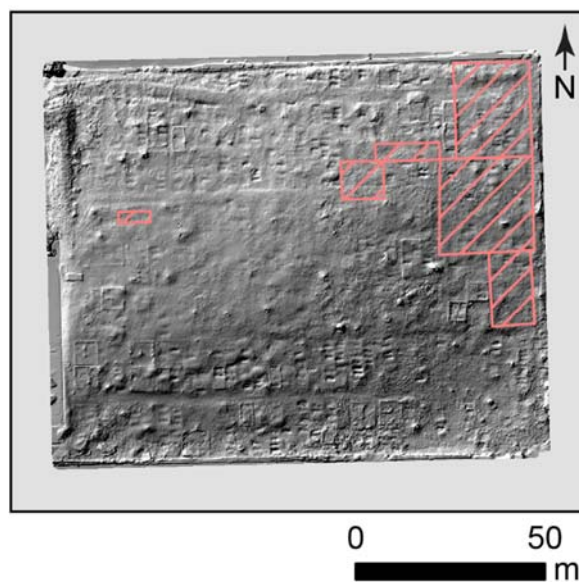


Figure 8. Geophysical survey using Ground Penetrating Radar was carried out on 12% of the Cemetery in six grids (pink hatched polygons). Both 250 and 500 MHz antennae were used at each grid with a line spacing of 0.5 m in a north-south (grave-normal) orientation.

Table 1. Counts of records identified as monuments, monuments & sunken graves, and graves with material culture in disrepair identified as well.

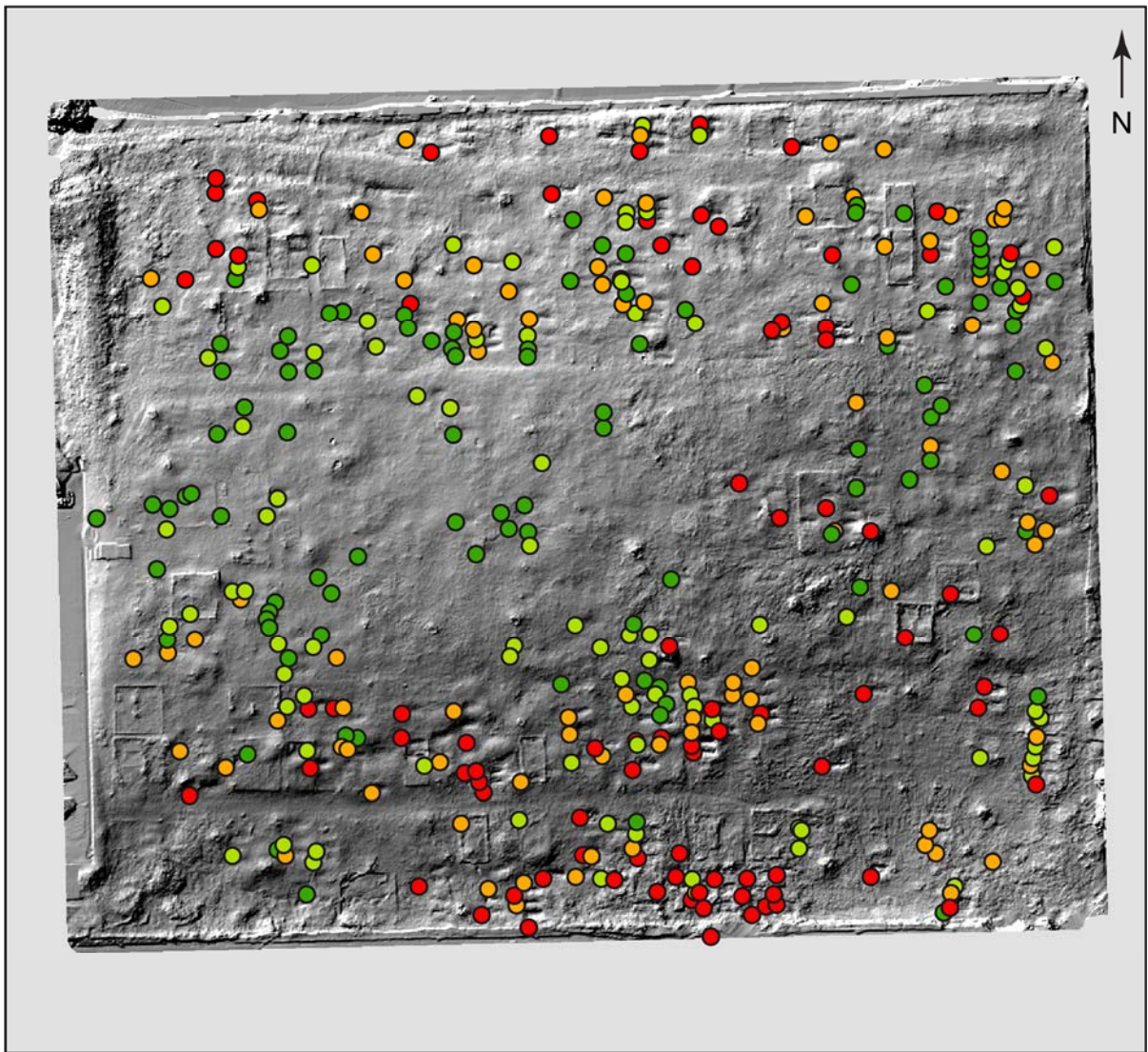
<u>Material</u>	<u>Monument (Disrepair)</u>	<u>Monument & Grave (Disrepair)</u>	<u>Sunken Grave</u>	<u>Total (Disrepair)</u>
<i>Carved Stone</i>	144 (58)	16 (7)	-	160 (65)
<i>Cement Marker</i>	59 (23)	8 (7)	-	67 (30)
<i>Metal Plaque</i>	32 (21)	15 (8)	-	47 (29)
<i>Wooden Headboard</i>	2 (2)	0	-	2 (2)
<i>Fieldstone</i>	259	13	-	272
<i>Other</i>	234 (4)	9	-	243 (4)
<i>Nothing</i>	-	-	296	296
<i>Sum</i>	730 (108)	61 (22)	296	1087 (130)

Table 2. Records identifying unique burials.

<u>Material</u>	<u>Monument</u>			<u>Monument & Sunken Grave</u>			<u>Sunken</u>	<u>Total</u>
	<i>Inscribed with Name</i>	<i>Inscribed without Name</i>	<i>Un-inscribed</i>	<i>Inscribed with Name</i>	<i>Inscribed without Name</i>	<i>Un-inscribed</i>	<u>Grave</u>	
<i>Carved Stone</i>	75	1	20	14	-	2	-	112
<i>Cement Marker</i>	23	3	9	3	-	5	-	43
<i>Metal Plaque</i>	13	-	16	2	-	13	-	44
<i>Wooden Headboard</i>	-	-	2	-	-	-	-	2
<i>Fieldstone</i>	-	-	130	-	-	13	-	143
<i>Other</i>	2	-	9	-	-	9	-	20
-	-	-	-	-	-	-	296	296
<i>Sum</i>	113	4	186	19	0	42	296	660

Table 3. Field recorded metrics of sunken graves at Oberlin Cemetery described by inclusive percentile measurements. Depth and width measurements were not always determinable in the field. Depth was indeterminate for two records, OC0192 and OC0760, due to dense vegetation and subtle topographic expression. Width was also indeterminate for OC0192 because of this vegetation.

Metric	Sample Size (n)	Minimum (cm)	25th Percentile (cm)	50th Percentile (cm)	75th Percentile (cm)	Maximum (cm)
<i>Depth</i>	355	1	7	10.5	17	118
<i>Width</i>	356	44	78	88	103	212
<i>Length</i>	357	110	204	222	236	288



Depth of Sunken Graves (cm)

- 1.0 - 7.0
- 7.0 - 10.5
- 10.5 - 17.0
- 17.0 - 118.0

0 50 m

Figure 9. Locations of sunken graves with point color indicating which quartile the grave's depth fit into from Table 3. Sunken graves within the fourth quartile appear to cluster along the middle portion of the southern edge; however, similarly deep values are found dispersed throughout the cemetery.

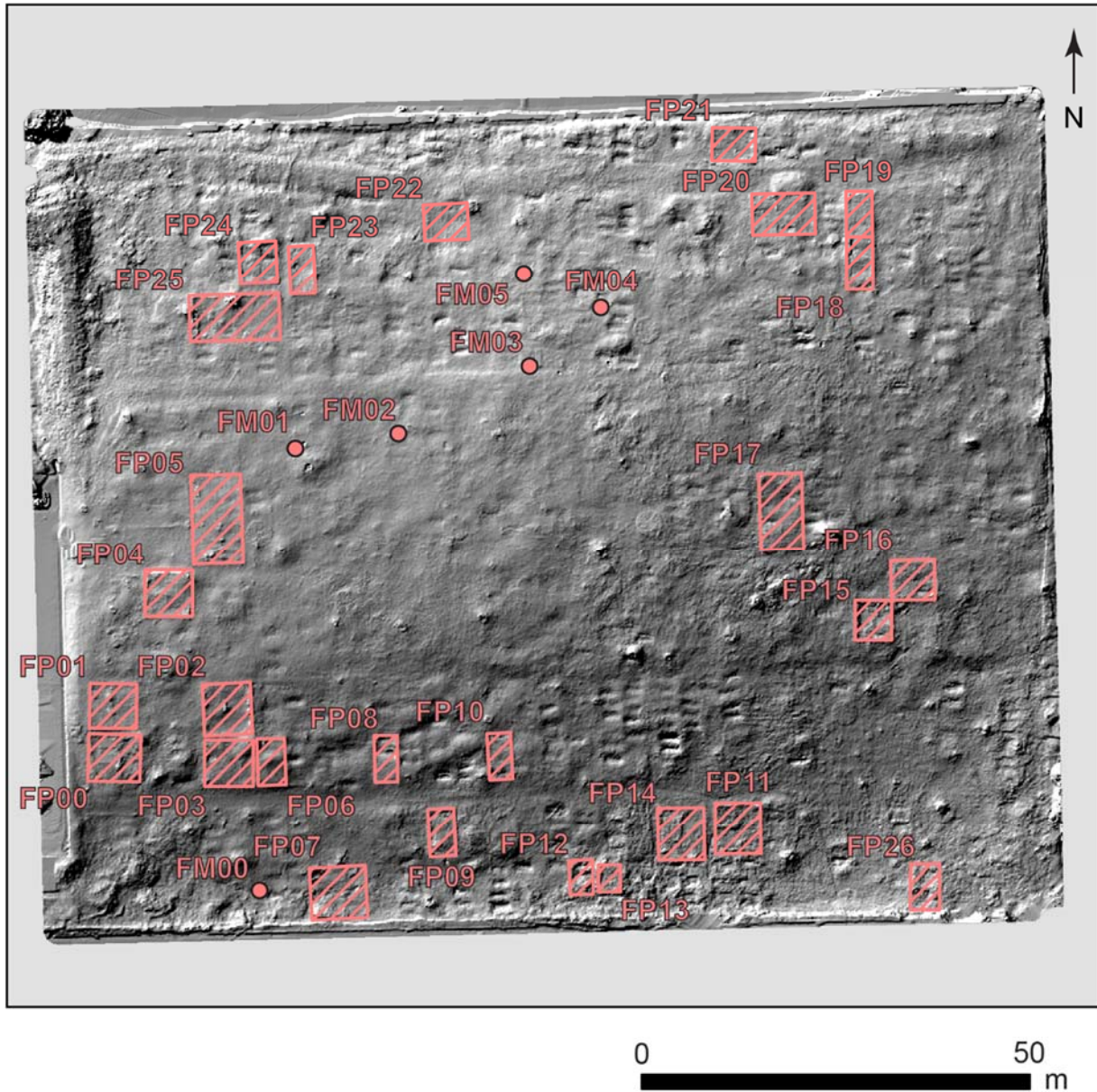


Figure 10. Family plots (pink hatched polygons) and family plot markers without enclosures (pink dots). Last names on markers and counts of records within enclosure are described in text as well as Appendix A.3.

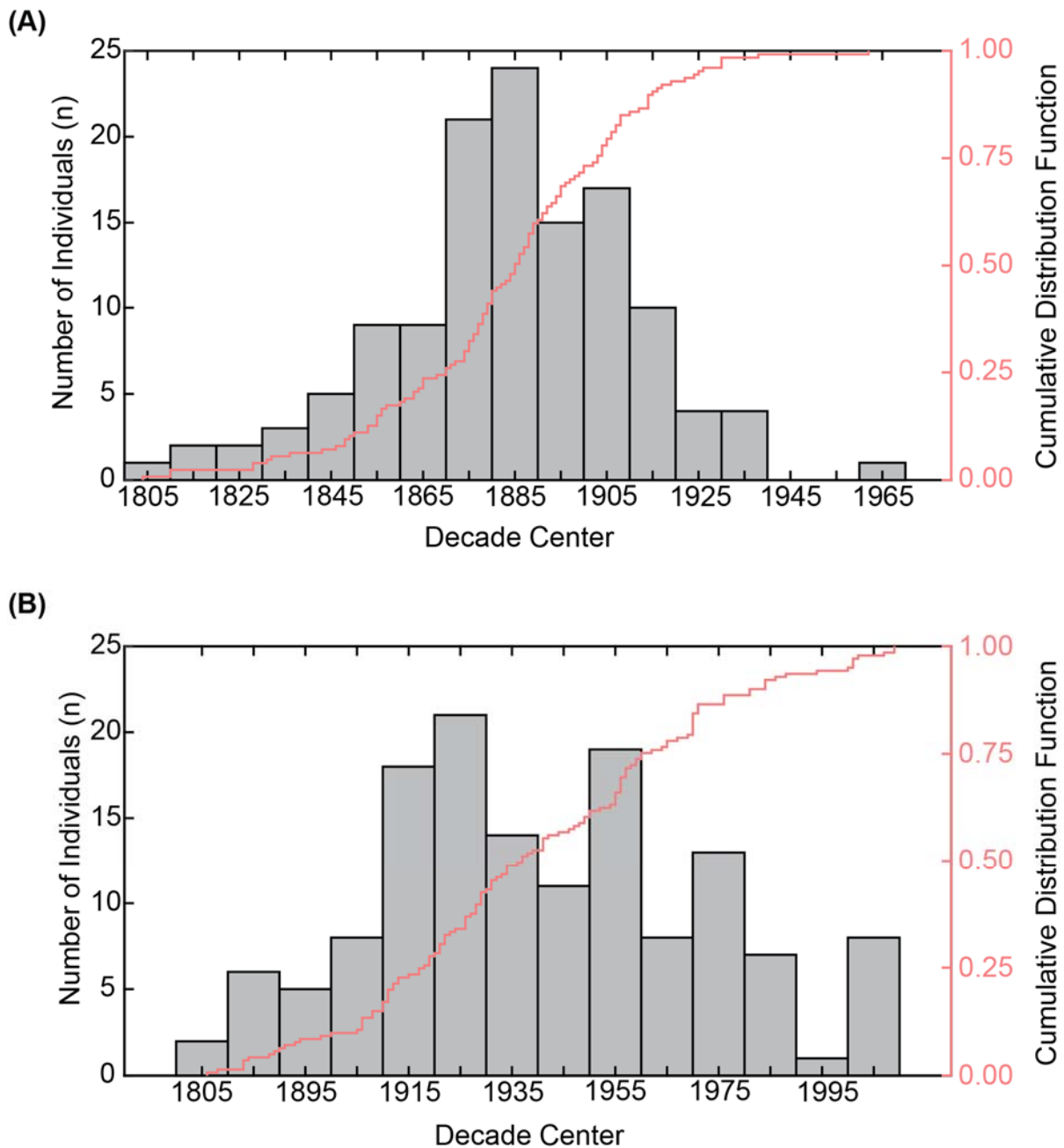


Figure 11. Distribution of (A) birth (n = 128) and (B) death (n = 142) dates found within Oberlin Cemetery. Count of individuals by decade are shown in comparison to the cumulative distribution of records for each graph. Thus, from grave markers with inscribed birth and/or death dates, 50% of individuals buried at Oberlin were born before 1885 while 50% died by 1935.

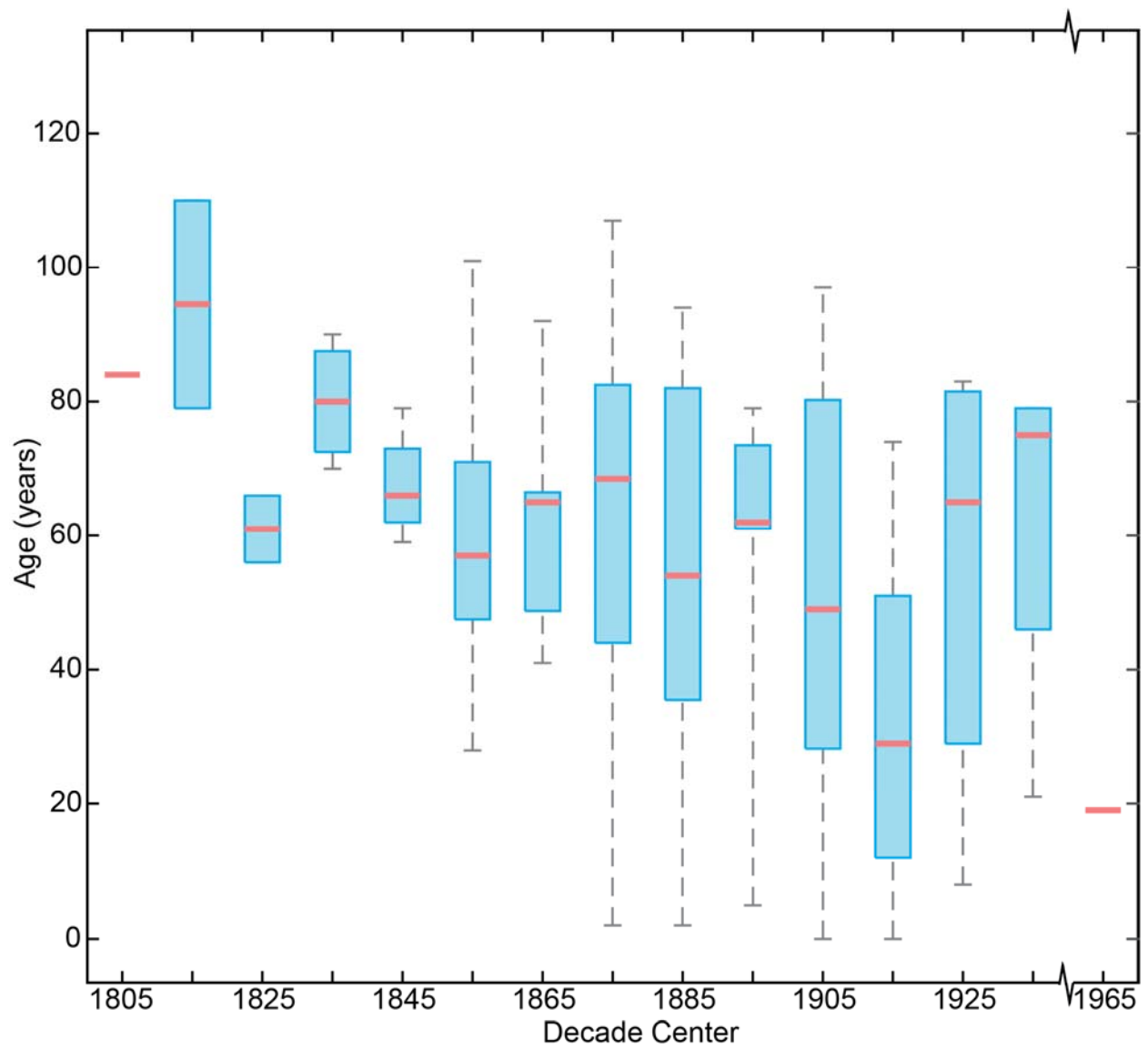
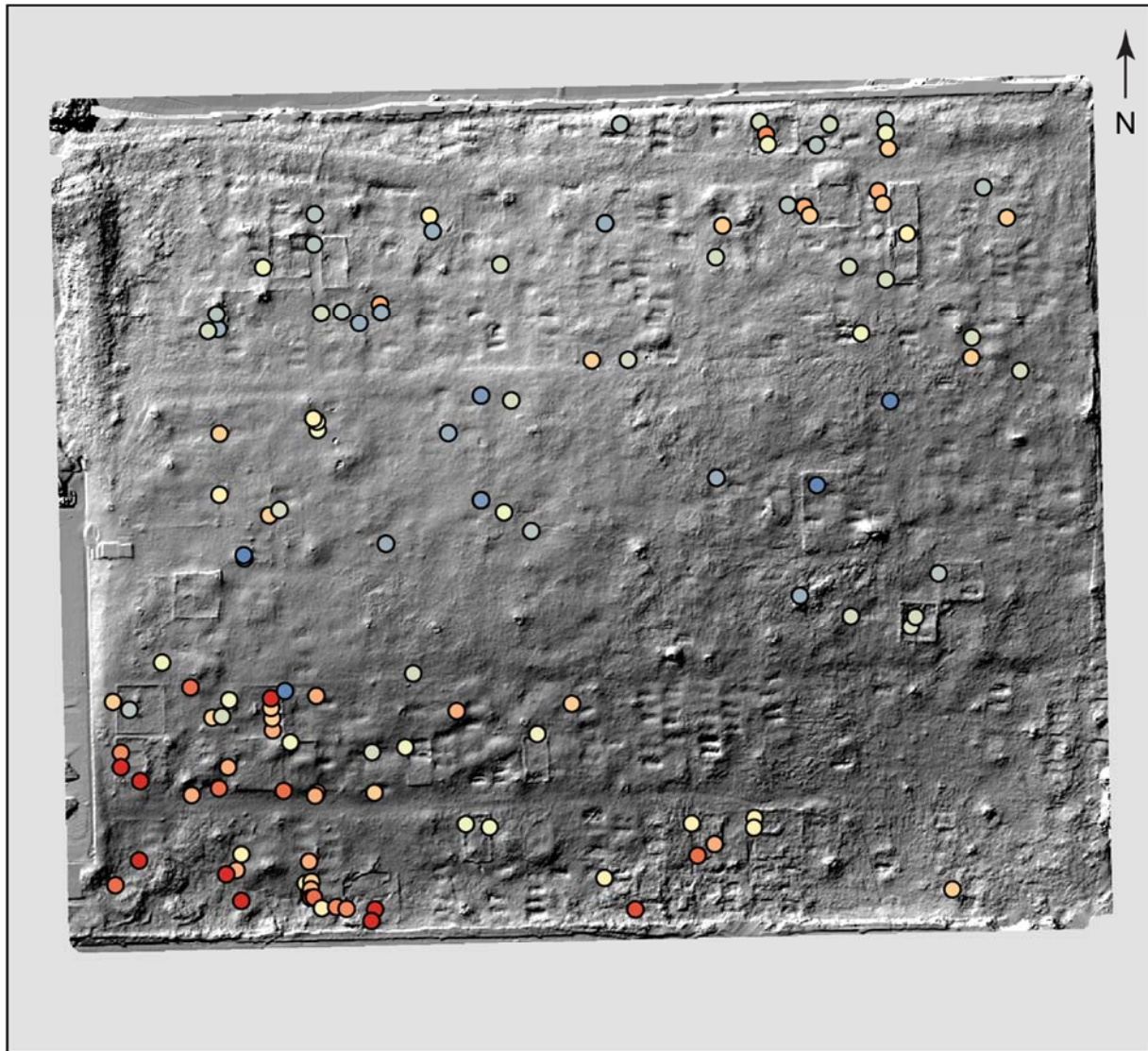


Figure 12. Age at death by decade of birth for individuals found within Oberlin Cemetery. **N.B.** there is a graph break between 1939 and 1960.



Inscribed Burial Date

- 1876 - 1880 ● 1911 - 1920 ● 1951 - 1960 ● 1991 - 2000
- 1881 - 1890 ● 1921 - 1930 ● 1961 - 1970 ● 2001 - 2009
- 1891 - 1900 ● 1931 - 1940 ● 1971 - 1980
- 1901 - 1910 ● 1941 - 1950 ● 1981 - 1990

0 25
 ─────────────────── m

Figure 13. Spatial distribution of burials with inscribed death dates symbolized by decade. There is no clear indication of clustering prior to 2000. Following 2000, burials cluster in the southwestern corner of the Cemetery.



Figure 14. Examples of social organizations on grave markers at Oberlin Cemetery. (A) The Prince Hall branch of the Freemasons, (B) Ancient Order of Oddfellows, and (C) Eastern Star Lodge of the Freemasons. Iconography and inscriptions shown with a graduated scale in 1, 2, 5, and 10-centimeter intervals.

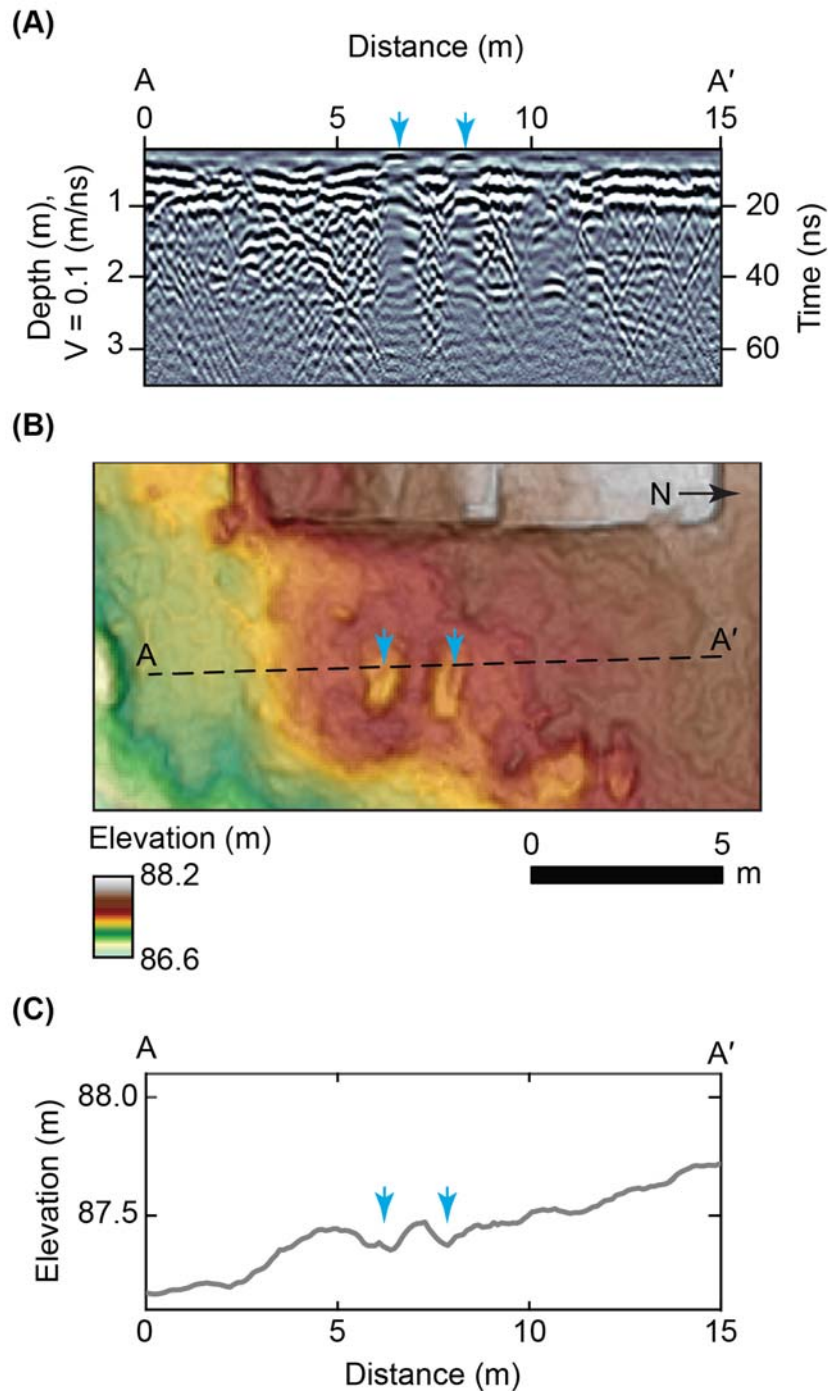


Figure 15. (A) Ground Penetrating Radar radargram created from 250 MHz antennae from A to A'. Data are visualized after applying a de-WOW filter, SEC2 gain, and background subtraction. Blue arrows indicate decoupling of the antennae due to depressions associated with sunken graves. These depressions are evident in (B) topographic data recorded with a terrestrial laser scanner and were inventoried during the pedestrian survey. (C) A topographic profile created from the digital elevation model additionally show the sunken graves.

Appendix A.1

Records identified in the field as “other” material culture.

<u>Record Identification</u>	<u>What is Recorded</u>	<u>Description</u>	<u>Notes</u>
OC0182	Monument & Grave	Metal scrap	Identified in the field as a monument and grave
OC0214	Monument & Grave	Metal scrap	Identified in the field as a monument and grave
OC0233	Monument	Zinc obelisk	Has a name on it
OC0278	Monument & Grave	Cemented gravel	Identified in the field as a monument and grave
OC0293	Monument	Metal pipe	Although it seems to be an edge marker, due to the small fieldstone just behind it, it could be a head marker
OC0429	Monument	Flower holder	Is a flower holder with a name on it
OC0631	Monument	Terracotta pot	From topographic data appears to represent a grave otherwise uncataloged
OC0647	Monument & Grave	Cinderblock	Identified in the field as a monument and grave
OC0659	Monument & Grave	Broken glass	Identified in the field as a monument and grave
OC0674	Monument	Flower holder	Spatially disassociated from other grave markers therefore might be likely to be a grave
OC0737	Monument	Flower holder	Spatially disassociated from other grave markers therefore might be likely to be a grave
OC0744	Monument	Flower holder	Spatially disassociated from other grave markers therefore might be likely to be a grave

Appendix A.1 (Continued)

<u>Record Identification</u>	<u>What is Recorded</u>	<u>Description</u>	<u>Notes</u>
OC0765	Monument	Flower holder	Spatially disassociated from other grave markers therefore might be likely to be a grave
OC0780	Monument & Grave	Brick and cement	Identified in the field as a monument and grave
OC0817	Monument	Cinderblock	Spatially disassociated from other grave markers therefore might be likely to be a grave
OC0923	Monument & Grave	Broken glass	Identified in the field as a monument and grave
OC0937	Monument & Grave	Flower holder	Identified in the field as a monument and grave
OC1016	Monument	Cemented gravel	Spatially disassociated from other grave markers therefore might be likely to be a grave
OC1033	Monument	Cinderblock	Spatially disassociated from other grave markers and follows a line of other markers therefore might be likely to be a grave
OC1097	Monument & Grave	Metal pipe	Identified in the field as a monument and grave

Appendix A.2

Registry of people identified in Oberlin Cemetery by field observation.

<u>Record Identification</u>	<u>First Name</u>	<u>Middle Name</u>	<u>Last Name</u>	<u>Birth Year</u>	<u>Death Year</u>	<u>Age</u>	<u>Previously Identified</u>	<u>Newly Identified</u>
OC0299	Julia		Andrews	1874	1876	2	x	
OC0299	Dynthia		Andrews	1875	1878	3	x	
OC0299	Margaret		Andrews	1855	June 1, 1883	28	x	
OC0299	Maggie		Andrews	1875	1883	8	x	
OC0299	Washington		Andrews	1878	1883	5	x	
OC1005	Maria		Dickerson	January 12, 1828	January 19, 1884	56		x
OC0810	Zylphia		Thompson	September 7, 1804	November 20, 1888	84	x	
OC0365	Oliffe		Poole	1810	February 17, 1889	79	x	
OC0095	Annie		Dunston	1850	July 19, 1890	40	x	
OC0299	Hattie		Andrews	1889	1891	2	x	
OC0557	Chapman		Alexander		August 4, 1893		x	
OC0093	John		Duston	1828	November 20, 1894	66	x	
OC0557	Sophia		Alexander		September 19, 1898		x	
OC0299	Mildred	W	Andrews	1895	1900	5	x	
OC0800	Alexander		Burton	1846	1905	59		x
OC0301	L	A	Busbee	1889	October 4, 1906	17	x	
OC0218	Ophelia		Sheppard	October 6, 1905	September 4, 1906	0	x	
OC0197	S	Patrick	McGuire	April 15, 1856	May 11, 1906	50	x	
OC0825	Emanuel		Bridgeford	March 4, 1836	March 28, 1906	70	x	
OC0216	Henrietta		Haywood	1863	November 7, 1908	45	x	
OC0668	Susie	S	Manly	September 6, 1888	June 15, 1908	19	x	
OC0312	Gladys		Williams	August 4, 1904	July 25, 1910	5	x	
OC0312	George	E	Williams	December 25, 1868	July 28, 1910	41	x	
OC0122	Jessie	Badie	Turner	May 29, 1860	August 18, 1910	50	x	
OC1069	Sara		Ivey	1848	1911	63	x	
OC0763	Annette	C	Andrews	January 15, 1885	July 6, 1911	26	x	
OC0124	Mary	Walker	Turner	September 4, 1886	February 5, 1911	24	x	
OC0044	Lula		Turner		1911		x	
OC0216	Edward		Haywood	1857	December 6, 1912	55	x	
OC0524	George	W	Williams	July 16, 1872	March 5, 1912	39	x	

Appendix A.2 (Continued)

<u>Record Identification</u>	<u>First Name</u>	<u>Middle Name</u>	<u>Last Name</u>	<u>Birth Year</u>	<u>Death Year</u>	<u>Age</u>	<u>Previously Identified</u>	<u>Newly Identified</u>
OC0668	Henry	C	Manly	June 27, 1856	July 13, 1913	57	x	
OC0222	Frank		Slade	October 24, 1832	October 23, 1913	80	x	
OC0965	P	T	Hall	1849	May 4, 1915	66	x	
OC0705	Sallie		Clarke	1887	1917	30	x	
OC0199	Pricilla	A	Hunter	September 1, 1855	October 16, 1917	62	x	
OC0741	Jesse		Scarver	1916	March 8, 1918	12	x	
OC0705	Haynes		Clarke	1848	1919	71	x	
OC0171	Robert		Williams	1870	May 5, 1919	49	x	
OC0741	John		Scarver	March 1, 1919	March 2, 1919	0	x	
OC1074	Jerry		Hinton	1810	May 30, 1920	110	x	
OC0639	Serena		McIlhenry	1831	July 1, 1921	90	x	
OC0571	Jesse	L	Pettiford	September 16, 1865	November 11, 1921	56	x	
OC0906	Edward		Cook		1921		x	
OC0909	Jimia		Barnweld	1843	December 30, 1922	79	x	
OC0044	John	T	Turner		1922		x	
OC0769	Sidney	G	Manly		March 5, 1922		x	
OC0800	Kate		Burton	1853	1923	70		x
OC1095	Fleming		Hinton	April 19, 1912	January 14, 1924	11	x	
OC0731	B	J	Curties	1861	June 2, 1926	65	x	
OC0362	J	D	Chavis	1871	March 17, 1926	55	x	
OC0224	Nora		Taylor	1900	August 15, 1926	26	x	
OC0745	Lucy	Wimbish	Montgomery	March 8, 1896	February 8, 1926	29	x	
OC0562	Elizabeth		Manly	1897	November 11, 1927	30	x	
OC0123	Grandison		Turner	August 10, 1853	February 4, 1928	74	x	
OC0827	Garland		Crosson	July 30, 1885	October 18, 1928	43	x	
OC1087	Thempie		Bobbitt		August 22, 1928	28	x	
OC1009	Susie		Parham	1888	January 4, 1929	41	x	
OC0041	Marshall	H	Smith	July 6, 1914	April 15, 1929	14	x	
OC0296	Lammentta	J	Hinton	October 5, 1864	December 3, 1929	65	x	
OC1017	Edward	T	Hester		February 26, 1929		x	
OC0387	Virginia		Hogan	1904	1930	26	x	

Appendix A.2 (Continued)

<u>Record Identification</u>	<u>First Name</u>	<u>Middle Name</u>	<u>Last Name</u>	<u>Birth Year</u>	<u>Death Year</u>	<u>Age</u>	<u>Previously Identified</u>	<u>Newly Identified</u>
OC0827	Garland		Crosson	July 30, 1885	October 18, 1928	43	x	
OC1087	Thempie		Bobbitt		August 22, 1928	28	x	
OC1009	Susie		Parham	1888	January 4, 1929	41	x	
OC0041	Marshall	H	Smith	July 6, 1914	April 15, 1929	14	x	
OC0296	Lammentta	J	Hinton	October 5, 1864	December 3, 1929	65	x	
OC1017	Edward	T	Hester		February 26, 1929		x	
OC0387	Virginia		Hogan	1904	1930	26	x	
OC0539	Theodore	F	Williams	April 11, 1875	September 13, 1931	56	x	
OC0157	Samuel	J	Webb	July 15, 1865	August 6, 1931	66	x	
OC0049			Dunston		1931		x	
OC0461	Joe		Copland	October 8, 1880	April 30, 1932	51	x	
OC0016	James		Ricks	February 9, 1865	October 3, 1933	68	x	
OC0789	Irving		Battle	March 1, 1900	March 27, 1934	34	x	
OC0042	Estelle		Smith	October 22, 1925	October 12, 1934	8	x	
OC0264	Hortense	S	Morgan	March 11, 1885	January 30, 1934	48	x	
OC1075	John		Wimbish		March 28, 1936	36	x	
OC0429	Martha		Hopkins	1910	May 9, 1937	32	x	
OC0734	Robert	H	Grant	April 27, 1908	December 3, 1937	29	x	
OC0431	Nellie		Bobbitt		March 15, 1938		x	
OC0384	James		Lipscomb	1874	1939	65	x	
OC0874	Adron		Curtis	1888	1941	53	x	
OC0104	Anna	B. Dunston	Starling	1903	1941	38	x	
OC0872	Mattie	L	Cruse	December 11, 1914	September 18, 1941	26	x	
OC0007	Plummer	T	Hall	March 12, 1886	December 15, 1941	55	x	
OC0859	Powell		Peebles	May 16, 1888	May 10, 1942	53	x	
OC0869	Alonzo		Jones	1877	1944	67	x	
OC1083	Thomas		Higgs	1884	1946	62	x	
OC0467	Curties		Snelling	October 10, 1884	November 24, 1947	63	x	
OC0195	Ella		McGuire		May 21, 1948		x	
OC0405	Lizzie		Alford	1877	1949	72	x	
OC0268	Mary	L	Morgan	August 27, 1908	April 2, 1949	40	x	

Appendix A.2 (Continued)

<u>Record Identification</u>	<u>First Name</u>	<u>Middle Name</u>	<u>Last Name</u>	<u>Birth Year</u>	<u>Death Year</u>	<u>Age</u>	<u>Previously Identified</u>	<u>Newly Identified</u>
OC0266	Wilson	W	Morgan	June 18, 1879	April 23, 1950	70	x	
OC0411	Frank		Howard		May 20, 1950	50	x	
OC1058	Frank		King	February 28, 1891	December 2, 1952	61	x	
OC1080	Charles	E	Flagg	1876	1954	78	x	
OC0046	Mary Jane	Dickerson	Turner	June 1863	March 26, 1955	92	x	
OC0944	Mary	H	Hinton	May 10, 1886	October 31, 1955	69	x	
OC1010	Walter	Allen	Dunston	May 12, 1892	January 16, 1955	62	x	
OC1077	Emma	H	Wimbish		March 7, 1955			x
OC0037	Amelia	T	Smith	August 13, 1906	January 22, 1956	49	x	
OC0589	William	B	Pettiford	August 4, 1893	January 26, 1956	62	x	
OC0389	Jessie		Dunston	February 11, 1892	November 23, 1956	64	x	
OC0767	Charles	H	Hunter	May 28, 1855	December 18, 1956	101	x	
OC1010	Virginia	Bryant	Dunston	September 23, 1894	September 4, 1956	61	x	
OC0036	Estelle	T	Smith	December 22, 1878	September 9, 1957	78	x	
OC0116	John		Anderson	December 25, 1895	May 25, 1957	61	x	
OC0755	William	E	Andrews	July 18, 1879	December 30, 1957	78	x	
OC0294	Alonza	M	Haywood	June 7, 1870	July 15, 1958	88	x	
OC0400	Alcoa	J	Allen	April 15, 1903	January 8, 1959	55	x	
OC0492	Jo	Ann	Turner	1938	1959	21		x
OC0406	Beachman		Alford	1915	1960	45		x
OC0040	James	L	Smith	February 29, 1905	October 14, 1960	55	x	
OC0372	Z	A	Poole	1880	1962	82		x
OC0215	Arthur	R	Shepard	August 14, 1881	April 25, 1964	82		x
OC1079	Sussie	T	Flagg	1878	1965	87	x	
OC0400	William		Floyd	March 5, 1891	June 22, 1965	74	x	
OC0404	Beechman		Alford	February 6, 1880	May 20, 1967	87	x	
OC0407	Essie	L	Smith	November 17, 1917	August 17, 1969	51	x	
OC0869	Mary	A	Jones	1877	1970	93	x	
OC0754	David	W	Andrews	1880	1970	90	x	
OC0356	George		Jeffries	1887	April 29, 1970	65		x
OC0391	Mattie	E	Williams	February 22, 1894	December 10, 1970	76	x	

Appendix A.2 (Continued)

<u>Record Identification</u>	<u>First Name</u>	<u>Middle Name</u>	<u>Last Name</u>	<u>Birth Year</u>	<u>Death Year</u>	<u>Age</u>	<u>Previously Identified</u>	<u>Newly Identified</u>
OC0392	Mattie	E	Williams	January 22, 1894	December 10, 1970	76	x	
OC0020	Eliza	Height	Parham	May 10, 1899	April 20, 1970	70	x	
OC0018	Claude		Snellings	October 15, 1890	August 12, 1970	79	x	
OC0008	Carl	A	Williams		November 16, 1970			x
OC0754	Georgia	H	Andrews	1895	1971	76	x	
OC0413	Ella		Howard	February 11, 1883	February 2, 1971	87	x	
OC0022	John	J	Turner	November 11, 1898	October 6, 1971	72	x	
OC0733	Eliza		Grant	1882	1976	94		x
OC0414	Leroy		Peebles	1926	1976	50		x
OC0035	James	S	Smith	January 16, 1874	January 27, 1976	102	x	
OC0043	Gertrude	B	Haywood	1889	1981	92	x	
OC0865	Henry Jose	C	Peebles	December 6, 1962	December 23, 1981	19	x	
OC0409	Lillie		Tillman	1907	1984	77		x
OC0408	Joesina	Alford	Tillman	November 21, 1907	April 23, 1984	76	x	
OC0013	Catherine		Trice	July 29, 1914	December 23, 1984	70	x	
OC0001	Carrie	W	Hunter	1879	1986	107		x
OC0052	James Patrick	Man	Haywood	1914	1988	74		x
OC0472	D	Supora	Taylor	1904	1994	90		x
OC0024	Ulia	Marie Hall	Turner	October 1, 1902	June 7, 2000	97	x	
OC0003	Rebecca	D	Whitter	1908	2001	93		x
OC0415	Robert		Peebles	1930	2001	71		x
OC0416	Dorothy	Peebles	Barker	November 11, 1906	February 2, 2001	94	x	
OC0038	William	T	Osbourne	January 27, 1922	October 5, 2002	80	x	
OC0029	John	V	Turner	January 22, 1924	November 25, 2007	83	x	
OC0009	Grace	H	Williams	1930	2009	79		x
OC0010	Alexander		Williams	1930	2009	79		x
OC1004	Lugenia		Durham		May 23, 195X			x
OC0944	Gideon		Hinton	October 19, 1876			x	
OC0090	Johnnie		Dunston				x	
OC0096	N	C	D				x	

Appendix A.2 (Continued)

<u>Record Identification</u>	<u>First Name</u>	<u>Middle Name</u>	<u>Last Name</u>	<u>Birth Year</u>	<u>Death Year</u>	<u>Age</u>	<u>Previously Identified</u>	<u>Newly Identified</u>
OC0098	E		D				x	
OC0099	B	H	Dunston				x	
OC0160			Webb					x
OC0164			Webb					x
OC0169	Ezekiel		Webb				x	
OC0216	Daniel		Williams				x	
OC0233			Anderson					
OC0355			Debnam					x
OC0732	Tempie		Curtis				x	
OC0786	Charles	W	Thorton				x	
OC0786	Emily		Thorton				x	
OC0920	B		B					x
OC1028	J	E	Jackson				x	

Appendix A.3

Family plot and markers identified at Oberlin Cemetery

<u>Record Identification</u>	<u>Enclosure Family Names</u>	<u>Has Family Monument</u>	<u>Features Inside (n)</u>	<u>Previously Identified</u>	<u>Newly Identified</u>
FP00	Turner	Yes	10		X
FP01	Turner	No	3		
FP02	Smith, Osbourne	Yes	8	X	
FP03	Snellings	No	3		
FP04	<i>Unknown</i>	No	2		
FP05	Dunston	No	21		
FP06	Pulley, Curtis, Trice	Yes	5	X	
FP07	Howard, Peebles	No	10		
FP08	Lipscomb	No	1		
FP09	Hopkins	No	6		
FP10	Copcland	No	3		
FP11	Cruse, Curtis	No	4		
FP12	Snelling	No	4		
FP13	<i>Unknown</i>	No	0		
FP14	Jones, Peebles	No	8		

Appendix A.3 (Continued)

<u>Record Identification</u>	<u>Enclosure Family Names</u>	<u>Has Family Monument</u>	<u>Features Inside (n)</u>	<u>Previously Identified</u>	<u>Newly Identified</u>
FP15	Cook, Barnweld	Yes	8		X
FP16	Hall	No	13		
FP17	Thompson	No	6		
FP18	Bobbitt, Higgs	Yes	6	X	
FP19	Flagg	No	4		
FP20	Andrews	No	12		
FP21	Grant, Curtis, Curties	No	10		
FP22	<i>Unknown</i>	No	2		
FP23	Hunter	No	5		
FP24	Webb	Yes	14	X	
FP25	Turner	No	7		
FP26	Hinton	Yes	5		X
FM00	Alford		N/A	X	
FM01	Morgan		N/A	X	
FM02	Williams		N/A	X	

Appendix A.3 (Continued)

<u>Record Identification</u>	<u>Enclosure Family Names</u>	<u>Has Family Monument</u>	<u>Features Inside (n)</u>	<u>Previously Identified</u>	<u>Newly Identified</u>
FM03	Pettiford, Hardy		N/A	X	
FM04	Trice		N/A	X	
FM05	Stanley		N/A	X	